DEVELOPMENT OF COST EFFECTIVE NANOSTRUCTURAL REINFORCEMENTS FOR ADVANCED COMPOSITES

A Thesis

Presented to

The Faculty of the Department of Engineering Technology

University of Houston

In Partial Fulfillment

Of the Requirements for the Degree of

Master of Science in

Engineering Technology

By

Anderson O. Okonkwo

August 2014

Acknowledgements

It is a wonderful moment when I reflect on the path I took towards achieving this work and those friends, relatives, colleagues and especially my family members who gave me their unequivocal support and guidance.

I wouldn't have achieved such a success without the candid advice of Dr. Francisco C. Robles Hernández, who guided me from the initiation through to the execution and close-out of this project. You made this project to be easy flowing and fun all along with your friendly conversations, responsive feedbacks and inspirations. You are my mentor.

I appreciate my wife, Schicasulyn, for all her prayers, good works and motivational words that kept me working harder; even when the going was very tough, she was my reliable support. I love you so much.

Many thanks go to my mom and my siblings for their prayers, advice and financial support towards my education. Though we are in different countries but I never felt alone and down cause I know that you are always praying for me and hearing your voices through phone conversations and Skype calls kept me going. Y'all are the best I ever had.

Finally, I want to appreciate my thesis committee members, Dr. El Nahas and Dr. Ignatiev for the time, support and efforts that they put in for the review of this work.

Abstract

The purpose of this work is to develop cost effective structural composites reinforced with complex carbon nanostructures for multiple applications. The main process in this study is mechanical milling which induce the *in-situ* transformation of carbon in the form of soot into complex nanostructures that behave as effective reinforcements. The soot mainly composed of amorphous particles with a high density of defects having a majority of sp2 bonding. During mechanical milling, this soot transforms *in-situ* into diamond, graphene and graphitic carbon. Milling media have two fundamental roles: welding and fracturing. A further contribution of milling in metal contamination is in some cases welcomed due to the presence of transition metals (e.g. Fe) with catalytic nature that sponsor further *in-situ* synthesis of carbon nanoreinforcements during sintering. The *in-situ* synthesized nanoreinforcements have demonstrated to be effective in improving mechanical properties in composites with various matrices including: ceramics, metallic and polymer (bio, organic and inorganic). Further, in this work is presented a novel sintering method involving induction heating at a high and low temperature. The induction sintering is pressure less. Novel processing technologies were demonstrated through the mechanical and characterization test results. In this study, we innovated a sintering process where induction heating is used and compared to Spark Plasma Sintering (SPS). The results will be supported by mechanical testing and characterization by means of x-ray diffraction, Raman spectroscopy, x-ray photoelectron spectroscopy, scanning and transmission electron microscopy.

Table of Contents

List of Figures

List of Tables

Chapter 1

1.1 Introduction

This work identifies the simple methodologies of developing cost effective complex carbon structures for nanostructural reinforcement of advanced composites. The raw material used is gotten from a byproduct of existing processes. It will also illustrate the characterization of the new product showing optimum properties and for a variety of applications. This work explores the tendencies of in-situ transformation of a commercially prepared sample of fullerene soot into a structural material that defeats the purposes of using similar materials in terms of their properties and applications. The fullerene soot is a by-product that results from the synthesis of fullerene by the Kratschmer method. This by-product is abundant and as of today no applications have emerged. This work demonstrates a wide variety of uses of this by-product. The fundamental processing methodology utilized is mechanical milling which is cost effective and can easily be gotten.

Carbon nanostructures are those allotropes of carbon that are in the nanoscale which includes carbon nanotubes, the fullerene family of buckyballs (i.e. C_{60}, C_{70}, C_{120} etc.) polyaromatic molecules, graphene among others as shown in Figure 1.1. The buckyballs are the most common allotropes of carbon with atomic orientation of carbon in pentagons, hexagons and heptagons (Kroto et al., 1985, Terrones and Terrones, 1997). There have been successful studies conducted towards the various synthesis of carbon nanostructures which results to the variety of structures available as allotropes of carbon (Harris, 1999, Kroto et al., 1985, Iijima, 1991, Ugarte, 1992). Figure 1.1 shows carbon nanostructures with their different orientation of the carbon atoms.

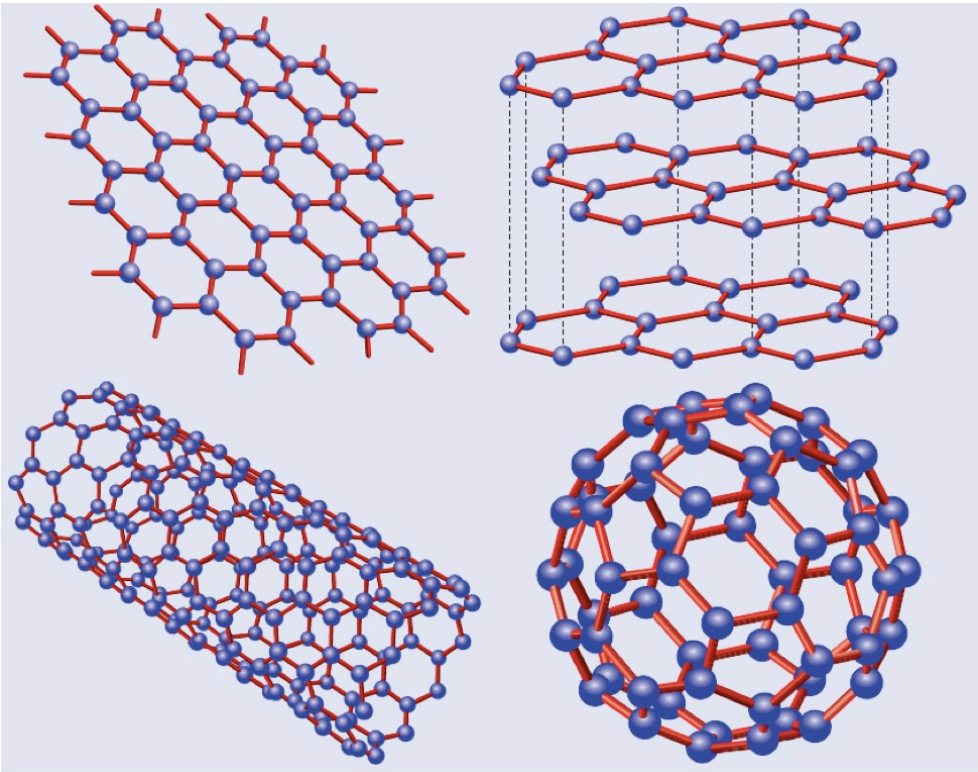

Figure 1. 1: Carbon nanostructures: top right: graphene; top left: graphite; bottom right: nanotube; bottom left: fullerene (as taken from [†])

Carbon nanostructures have made a big mark in many research projects as it is extensively researched in many applications. In search of solutions to energy problems and prevention of degradation of the planet, researches on carbon nanostructures were extended to its application in energy which led to the development of different carbon based nanostructures with different shapes and sizes which includes but not limited to carbon nano-onions, carbon nanohorns, carbon nanotorus, carbon nanobuds, carbon nanocups and carbon peapods which are mainly synthesized hybrid systems (Martin et al., 2011). These carbon nanostructures are shown in Figure 1.2.

[†] http://graphene.nus.edu.sg/content/graphene

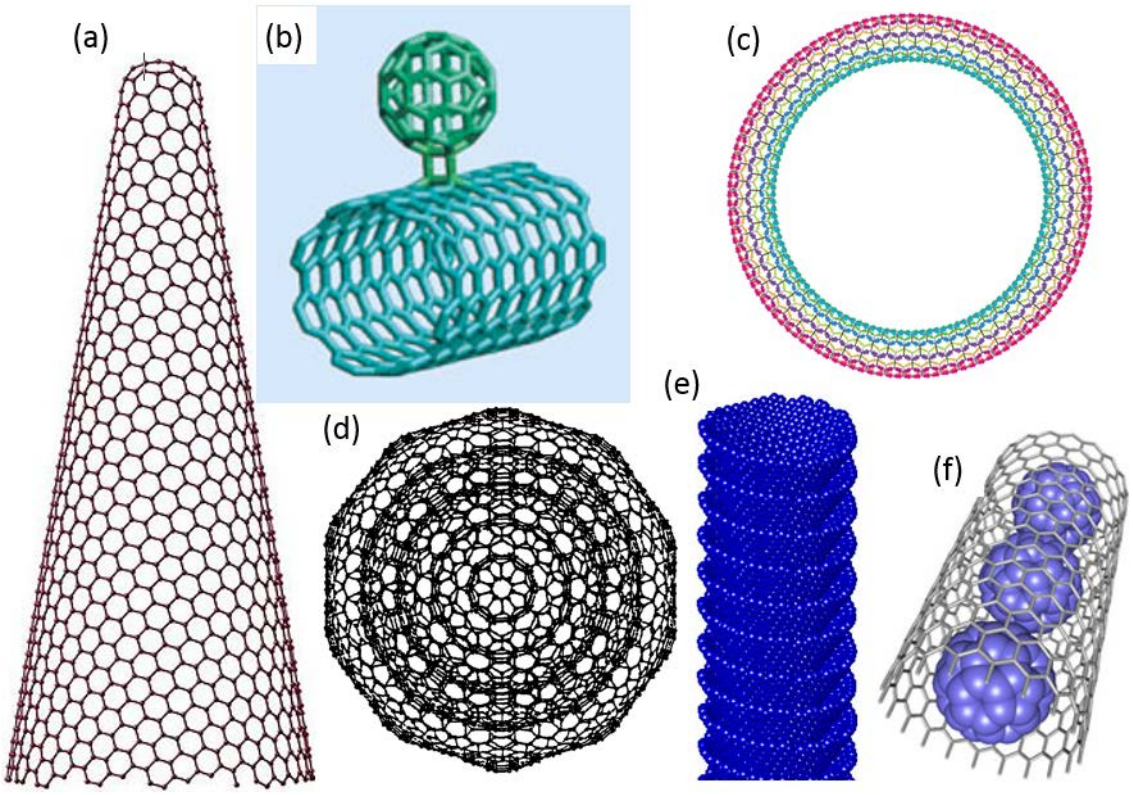

Figure 1. 2: (a) Carbon nano-horns [‡], (b) Carbon nano-buds [§], (c) carbon nano-torus [**], (d) Carbon nano-onions [††], (e) Carbon nano-cups [‡‡], (f) Carbon-peapods [§§]

Graphene still possesses more interest as compared to the above listed carbon nanostructures since its applications have reached out to other aspects of science due to its properties. Its outstanding properties; including thermal, optical, electrical, mechanical etc. Graphene is also exploited towards the development of new technologies and devices (Warner, 2013). Notwithstanding, the properties of carbon nanostructures has been explored

[‡] http://en.wikipedia.org/wiki/Single-walled_carbon_nanohorn
[§] http://www.rsc.org/chemistryworld/News/2007/February/26020701.asp
[**] http://physicsworld.com/cws/article/news/2002/may/22/nanotorus-nets-giant-magnetic-moment
[††] http://www.google.com/patents/US6599492
[‡‡] http://apsci.com/?page_id=19
[§§] http://www.chimica.unipd.it/enzo.menna/naphod.html

towards the reduction of agglomeration of particles when applied in a composite (Robles-Hernandez and Calderon, 2010). Soot, a nanostructural carbon particle has been used to produce a wide range of porosity, conductivity and hardness when applied towards the reinforcement of alumina matrix composites thereby reducing the electrical resistivity of the composite from 7 to 14 orders of magnitude (Fals et al., 2013). Generally, carbon nanostructural reinforcements are used to improve mechanical properties thereby ensuring integrity of a composite (Robles-Hernandez and Calderon, 2010, Garibay-Febles et al., 2000, Zhan et al., 2003, Zhan et al., 2002, Zapata-Solvas et al., 2010, Kim et al., 2012, Robles Hernandez and Calderon, 2012).

Due to the high demand on carbon and carbon based materials especially their nanostructures, it is objective to determine a cheap and commercially available methodologies of synthesizing this material which is part of the motivation in this project. The tendency of having a carbon based material with high strength and other optimum properties that could be utilized in many applications and industries to improve on some already established processes is the main motivation of this work.

This project intensively explains the cost effective techniques involved in *in-situ* transformation of readily available soot and proposes that further research should be carried on the tendency of making these techniques commercially available. The idea of transforming fullerene soot at solid state into a material that exceeds the mechanical properties of other materials of its kind used in structural applications is the core of this work. Previous studies have synthesized C_{60}, nanotubes and graphene through chemical reactions, laser vaporization, combustion etc. (Kroto et al., 1985, Scott et al., 2002, Iijima, 1991, Guo et al., 1995b), yet none was on solid state with readily available processing

methods. This *in-situ* transformation of fullerene soot at solid state was achieved through mechanical milling.

As another part of this work is the novel sintering technique of the powders which is used to get a consolidated sample at a low and high temperature, 300^0C and 2000^0C respectively. Our innovative sintering method supersedes the conventional methods of sintering by applying pressureless sintering performed using induction heating at different temperatures without causing a change in the chemistry of the material and yet retaining the required densification. It is interesting to note that this sintering technique was achieved with no applied pressure. Samples sintered using this technique requires no specific additives or sintering aids. Though the sintering temperature is high, it didn't affect the chemistry of the sample which was demonstrated using different characterization analytical tool to attain the nanostructural properties of the sample.

1.2 Project purpose

The main purpose of this project is to develop a cost effective technique for *in-situ* transformation of soot, which is a byproduct of a known process, into complex carbon nanostructures which can serve as a reinforcement for advanced composites. The driving force for this project is the tendency of this material to be utilized in several applications which is possible due to the optimum mechanical properties of this material. This properties was harnessed as a result of mechanical milling.

Applications of carbon nanostructures in supercapacitors have been a distinct in the field of researches for different types of supercapacitors especially the electrochemical double layer capacitors (EDLC) because of their relatively low cost and high operation

stability (Guo and Li, 2011). Due to the high demand of carbon based nanostructures in this field, this work poses an advantage to the industrial application. This is due to the technique which is cost effective and can be commercially viable for the strengthening of structural composites and application in batteries as an active material for their supercapacitors for a higher power density.Though the material possesses optimum mechanical properties, it was gotten from mechanical processing of the byproduct of a known process and after the *in-situ* transformation it poses as one of the most cost effective material of its kind.

1.3 Project objectives

The main objective of this study is to demonstrate the *in-situ* transformation of soot to form complex carbon nanostructures at solid state for reinforcement of advanced composites utilizing a cost effective technique. This complex carbon nanostructures possesses optimum mechanical properties. The driving force of this objective is the ability of this material to optimize the experimental conditions and improve properties for multiple applications. This objective was achieved through mechanical milling of fullerene soot to synthesize graphene, graphitic carbon and some traces of diamond.

As a second part of this study's objective is to achieve optimum properties after sintering this material without pressure using induction heating at a high and low temperature under a vacuum. Characterization of the samples will be done using Raman spectroscopy, x-ray diffraction and transmission electron microscopy. The objectives of this study as subdivided into different phases which are mechanical milling, sintering, mechanical testing & characterization and applications are as follows:

Mechanical milling:

- To demonstrate the in-situ transformation of the raw samples to nanostructural composites.

Sintering

- To demonstrate the solid state consolidation of the powder samples at different temperatures without affecting the chemistry of the sample or the nanostructural nature obtained during milling.

Mechanical testing & Characterization

- To analyze the microstructures of the sample and obtain the mechanical properties of the sample.

Applications

- To ascertain the various applications of the sample in composites with different matrices which include all carbon, polymer (epoxy, chitosan), metals and semicondutors (batteries – MoS_2) and ceramics (batteries – silicon).

Chapter 2

2.1 Literature review

This chapter shall explores the information about the state of the art in the literature currently available. These information are gotten from different literatures, research works and projects. It relates the evolution of the essential materials and methods as applied in previous works. It also identifies the relevance of this study when compared to the work previously reported in the literature. In this chapter, full mechanism working the different tools used for this study shall be demonstrated. This literature review will begin with a description of different carbon nanostructures, followed by the raw material used and the different processing undertaken to ensure that the required results are gotten.

2.2 Buckminsterfullerene

Fullerene is a molecule consisting of 60 carbon atoms that forms a hollow, cage-like structure bonded in hexagon and pentagon. Each of its orbitals contains sp^2 hybridized carbon atoms (Vul, 2002). It was first discovered by Harold W. Kroto, Sean O'Brien, James Heath, Robert Curl and Richard Smalley in 1985 when they tried to understand the absorption spectra of interstellar dust (Baggott, 1994). Though their experiment wasn't completely successful, they discovered the buckyball by vaporizing graphite with laser in an atmosphere of helium gas (Kroto et al., 1985). Some structures of fullerene were also discovered five years earlier through the use of an electron microscope in the form of bucky onion by Sumio Iijima (Iijima, 1980).

Buckminsterfullerene, as named after the American architect Richard Buckminster Fuller due to his geodesic dome, have been believed to exist naturally in space as noted by

Kroto (Kroto, 1996). The discovery of fullerene led to the increase in known allotropes of carbon which have been mainly diamond, graphite and amorphous carbon. Since its discovery, different structures of fullerene have developed which includes buckyball clusters, nanotubes (Miessler and Tarr, 2004), megatubes (Mitchell et al., 2001), polymers (Hiorns et al., 2010), nano-onions (Sano et al., 2001), linked ball-and-chain dimers (Shvartsburg et al., 1999) and fullerene rings (Li et al., 2001). Some applications of fullerene includes (1)solar cells, (2)catalysts, (3)optical limiters, (4)medicines, (5) lithographic films, (6)fullerene based polymers, (7)precursors for CVD diamond films and SiC, (8)lubricants and (9)starting constituent for extra-hard materials and diamond (Withers et al., 1997, Vul and Huffman, 1998).

Fullerene is mostly likened to a soccer ball due to its spherically shaped structure. Figure 2.1 illustrates a model of the structure of the buckyball forming a truncated icosahedron and comprises of 12 pentagons and 20 hexagons in which a carbon atom is located at the vertices of each polygon and bonds to form another polygon.(Pleshakov, 2014, Yang and Zhang, 2014)

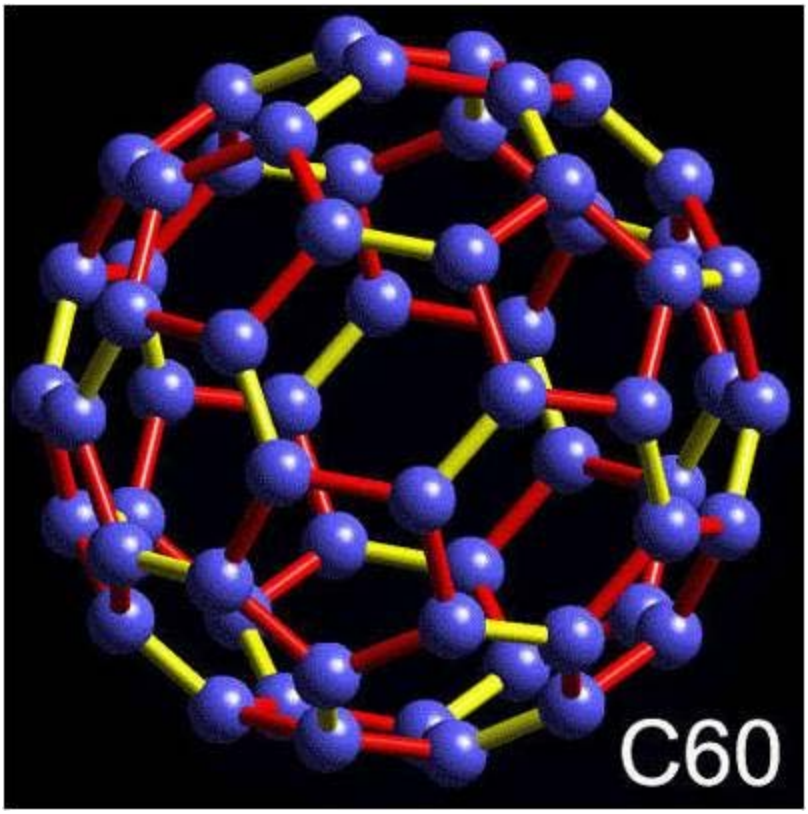

Figure 2. 1: Simulated model of buckyball (As taken from[***])

2.3 Carbon nanotubes (CNT)

Carbon nanotubes are allotropes of carbon in the nano-scale with a cylindrical structure and a part of the fullerene structural group. The chemical bonding in nanotubes are formed at the sp^2 atoms which is similar to graphene and that serves as a reason for their excellent strength (Mintmire et al., 1992). There are also reported chemical bonding of graphene leaves along the sidewalls of the nanotubes (Yu et al., 2011), which becomes the reason for their excellent supercapacitor performance (Stoner et al., 2011). Nanotubes have

[***] http://vivascriva.com/tag/buckminsterfullerene/

been developed at the length-to-diameter ratio of about 132,000,000:1 which supersedes that of any known nanomaterial (Wang et al., 2009) and are aligned into long tracks held together van der Waals force known as pi-stacking (Sygula et al., 2007).

Currently, CNT can be synthesis through arc discharge (Iijima, 1991), laser ablation (Guo et al., 1995a), plasma torch (Smiljanic et al., 2002) and chemical vapor deposition (Joseyacaman et al., 1993). There are properties that makes CNT outstanding as a structural material which includes high strength, hardness and thermal properties. These properties contribute to the numerous applications of CNT which include bulk nanotubes applied as composite fibers in polymers to improve mechanical, structural, thermal properties of the product (2009); chemical bonding to epoxy to form composite materials that are stronger than other composites (Pagni, 2010); tips for atomic force microscope probes (Willemsen et al., 2000) and scaffolding for bone growth in tissue engineering (Zanello et al., 2006). Figure 2.2 shows a computer simulated image of carbon nanotubes with different orientation.

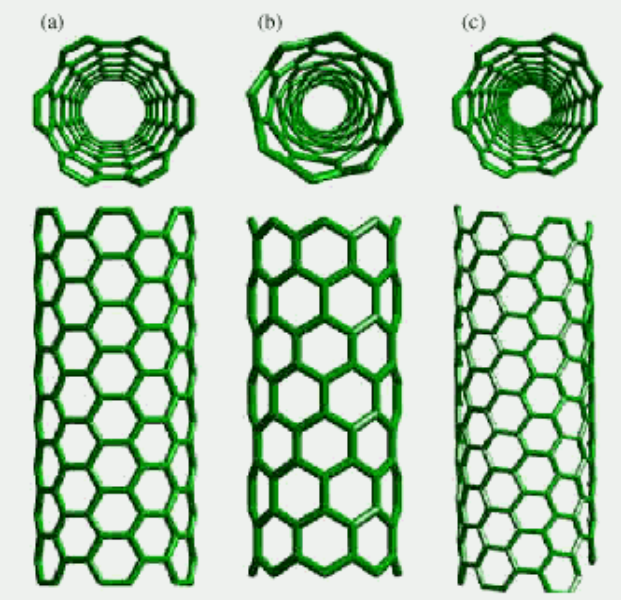

Figure 2. 2: (a) armchair; (b) zigzag; (c) chiral (As taken from[†††])

2.4 Graphene

Graphene exists as a single atomic layer of carbon which is bonded by sp^2 hybridized orbitals in a honeycomb lattice. It can be said that graphene is the foundation for the perception of the structures and functional attributes of graphite, fullerene and nanotubes (Guldi and Martin, 2010). The research group from Manchester, led by Andrei Geim and Kostya Novoselov, developed the 'scotch-tape' mechanical exfoliation technique for developing graphene (Wonbong and Lee, 2012)

Philip Kim also observed the quantum Hall effect and Berry's phase in graphene and discovered some electronic properties of graphene (Zhang et al., 2005). Rodney Ruoff improved the chemical vapor deposition growth of graphene using metal catalysts (Li et al.,

[†††] http://education.mrsec.wisc.edu/nanoquest/carbon/

2009). It is noted that more researches have been ongoing in this field but a few was mentioned to give an insight of what has been obtainable in that area. The high rate of research on graphene is driven by its properties which include high current, low resistance, high transparency over sheet resistivity, high surface to volume ratio, high mechanical strength/weight ratio density, high surface to volume ratio, ballistic transport, chemical inertness, high thermal conductivity, optical transmittance and super hydrophobicity at nanometer scale (Wonbong and Lee, 2012).

Though there have been so many research studies in exploring the properties of graphene, most of its applications are still developing (Wonbong and Lee, 2012).. Currently, the applications of graphene includes transparent electronics, flexible electronics, ultra-sensitive detectors, heat dissipation, field emissions, semiconductors, gas absorbers, sensors, solar cells, fuel cells, composites, energy and strengthening of tires (Wonbong and Lee, 2012, Masir, 2012).

Typically, graphene can be synthesized through four different methods which includes (1) chemical vapor deposition (Eizenberg and Blakely, 1979); (2) scotch tape method of mechanical exfoliation (Geim and Novoselov, 2007); (3) epitaxial growth of graphene films on an electrical insulating substrate (Berger et al., 2004) and (4) chemical reduction of graphene oxide derivatives from natural graphite flakes (Stankovich et al., 2007). Amongst these methods of developing graphene, chemical vapor deposition have been the most successful but graphene developed through this methodology turns out to be more than a single crystal which is as a result of nucleation and growth during the process. This can cause some degradation and variation in properties of graphene-based devices (Wonbong and Lee, 2012). This study presents the advancement of research in graphene

done in the aspect of cost effective synthesis, properties, characterization and applications of graphene. In this work is presented a new method to synthesize graphene and graphitic carbon. This method is simple and cost effective. In addition, the amount of synthesized particles is larger than conventional methods. Figure 2.3 shows a simulated model of graphene bearing an atomic-scale honeycomb lattice which comprises of carbon atoms.

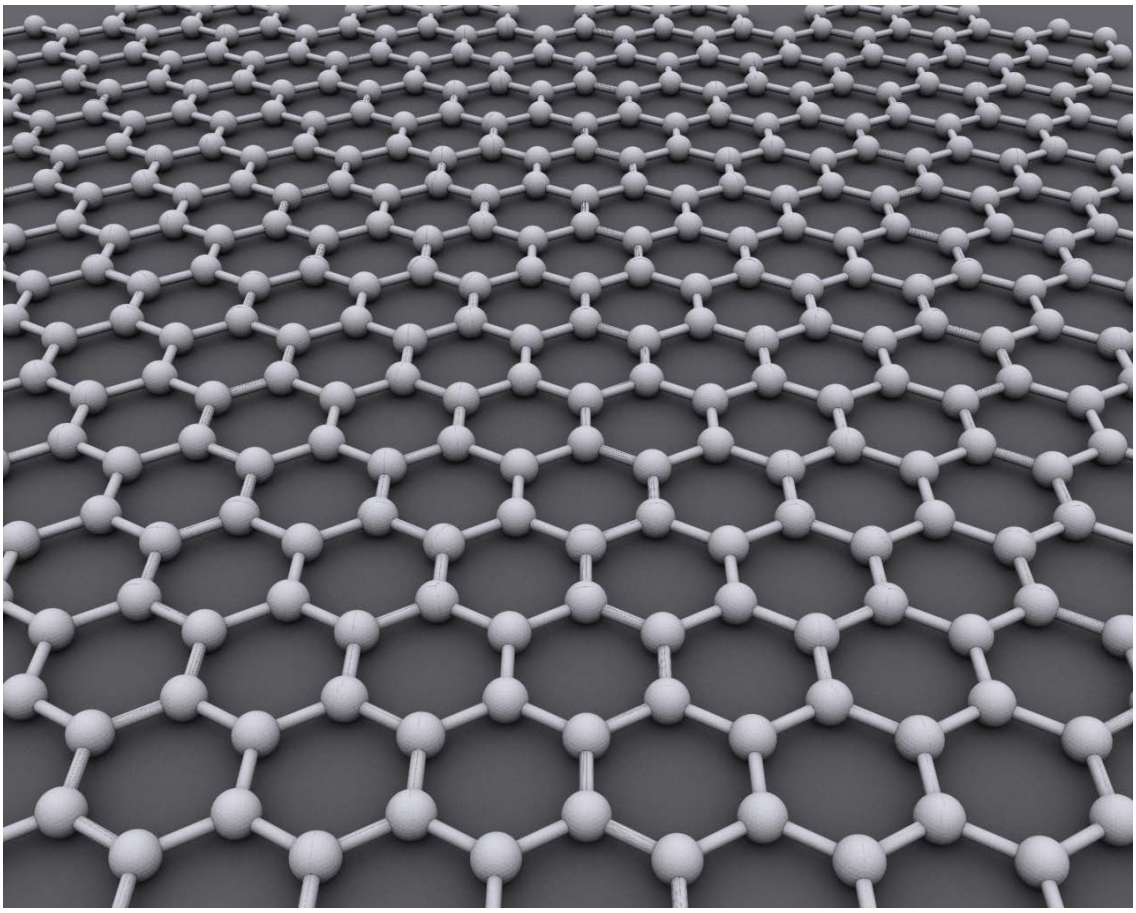

Figure 2. 3: Simulated model of graphene [‡‡‡]

[‡‡‡] http://en.wikipedia.org/wiki/Graphene

2.5 Soot

Soot is a black powdered and solid material consisting of carbon particles that forms from incomplete combustion of hydrocarbons. Soot is a byproduct of mostly gas phase combustion of fuel substances like coal, petroleum coke, charred wood etc. In this work, we are using fullerene soot that is the waste of the synthesis of fullerene. This byproduct is produced at a rate of >1µg per gram of fullerene. Theoretically, soot has accounted for a major part of global warming being the second largest cause (Bond et al., 2013).

This study illustrates the synthesis of carbon nanostructures through the *in-situ* transformation of soot. This soot synthesizes different carbon nanostructures which is characterized using different techniques and the results are analyzed to define the constituents of the final product. It is important to note that there are many similarities with the results gotten from different characterization technique as related to different carbon nanostructures. This is considered during the analysis to ensure that the sample contains the desired nanostructures.

2.6 Mechanical milling

Mechanical milling is a solid-state mechanical method of powder processing which introduces reactant substance to a powder to propel solid state reaction within the system. This technique involves continuous cold welding, fracturing and re-welding of powder particles using a high-energy ball mill (Suryanarayana, 2001). This technique can drive chemical reactions but it is usually applied to get amorphous, nanocrystalline and quasicrystalline materials, supersaturated solid solutions, reduced minerals, enhance surface area and reactive chemicals (Calka and Wexler, 2004). Over the years, mechanical milling

has proving to be a very convenient and effective way to produce nanoparticles (Wang and Jiang, 2007) with improved physical and mechanical properties (El-Eskandarany, 2001) due to its low cost, simple operation, high yield etc. (Wang and Jiang, 2007).

However, continuous deformation and fracturing of powder substances propels solid-solid, solid-liquid and solid-gas reactions while milling (Calka and Wexler, 2004). Besides inducing size reduction, there are mechanochemical effects observed on the milled particles which can be quantified by the degree of crystallinity, crystallite size, lattice strain and lattice parameters (Palaniandy and Jamil, 2009). These effects causes formation of dislocations and point defects in the crystalline structure, mechanical activation of solid materials and polymorphic transformation, amorphization and crystallization (Zhang et al., 2007). This effects contributes to the reason for the high intensity of the D band in our sample as we observed through the Raman spectroscopy.

In this study, we will show how mechanical milling propels the development of nanostructural carbon materials without the additions of catalyst material (Fe or Ni) at different times of milling. This is an advantage due to the numerous applications that require nanostructural properties in the chemical, mineral and ceramic industries. The mills used in this study is spex mills. It is very necessary to consider the material properties as a dry and fine particles is high recommended for the final product. This could be an issue due to the high possibility of adherence, aggregation and agglomeration as there are high interaction between the particles (Pourghahramani and Forssberg, 2007a, Pourghahramani and Forssberg, 2007b). Some additives can be used to prevent this issue such as alcohol, ketones, amines, carboxyl acids, esters, electrolytes, surfactants and neutral or changed polymers

(Zhang et al., 2007, Garcia et al., 2004) and in some cases of agglomeration, sonication can be applied to reduce it (Li et al., 2006).

Milling can result in contamination through the deposits of iron from the walls of the vial and media. The iron in our work helps to catalyze the *in-situ* transition of the raw material but this contamination were minimal. As the milling time increases, the material deforms and cold weld into layered formation with reduced ductility. This layered formations can be further deformed and fractured, as desired with greater milling time, thereby causing interdiffusional reaction at the surfaces of the layered formation to form the desired product (El-Eskandarany, 2001). In other words, milling time plays an important role in determining the properties of the final product. Spex mills uses a wide range of materials from metals and polymers to ceramics. Figure 2.4 shows an example of steel vial, o'ring and grinding balls of different sizes used in the spex mill.

Figure 2. 4: Steel vial set comprising vial, lid, cap, ball sets and o'ring

The mechanical milling was conducted using a Model 8000M spex mill manufactured by SPEX SamplePrep as shown in Figure 2.5. Figure 2.5 also shows an inset to clearly see the milling mechanism. The steel vial used can mill from 0.2 to 2 grams of carbon soot at a time. The steel milling balls are of ratio of 3:1 in sizes with the biggest ball being 0.25 inches.

Figure 2. 5: High energy spex mill

2.7 Sintering

Sintering is a metallurgical process of fusing powder together by heating the material in a furnace below is melting point. This process works on the basis of atomic diffusion (Kingery et al., 1976, Cizeron et al., 1974). This means that when powder materials are held together in a mold and heated below but near the melting point, the atoms diffuse across the grain boundaries of the particles thereby fusing the particles into one piece.

There has been an increased application of spark plasma sintering (SPS) in powder metallurgy as opposed to conventional method (Santanach et al., 2011a) which uses elevated temperatures and long holding time. Spark plasma sintering has proved to have advantages over other methods of sintering like the conventional method and hot-pressing, even at lower temperatures and shorter holding times when applied to ionic materials (Chaim et al., 2008, Artemenko et al., 2010, Santanach et al., 2011b). Depending on the material, SPS fuses powders at a certain temperature and pressure while passing direct current through an electrically conductive pressure die containing the sample. Uniaxial pressure is applied while sintering to attain full density easily. Figure 2.6 shows the comparison of conventional and SPS methods of sintering in terms of their working temperatures and holding times.

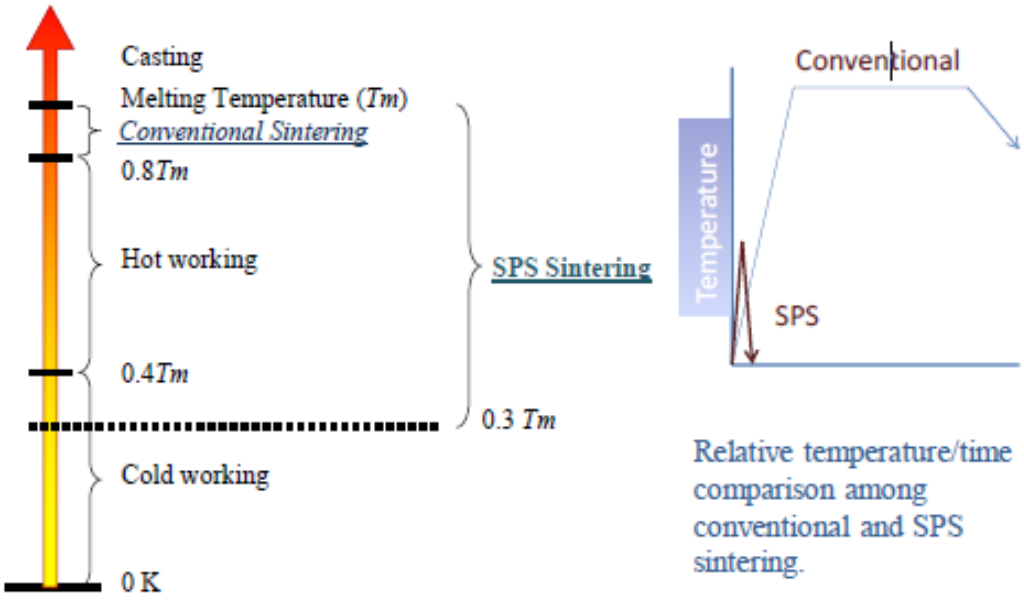

Figure 2. 6: Comparison between conventional and SPS method of sintering(Barber, 2013)

Pressureless sintering involves the sintering of a compacted powder at a temperature of about 2000^0C without the application of pressure (Lee and Speyer, 2003, Chamberlain et al., 2006). The powder is compacted in mold (depending on the material) in order to form the required shape before heating to sinter. This method solves the issue of density variations which is common with traditional hot pressing methods. Before near full density is achieved in hot pressing sintering process, sintering aids (like carbon, Al_2O_3, TiB_2) are added (Lee and Speyer, 2003). Improvements in flexural strength, modulus of elasticity and wear resistant of the final product have been achieved through the post-sintering hot isostatic pressing (HIP) applied to reach 100% of theoretical density (Schwetz et al., 1986). Pressureless sintering is often more preferable to avoid extra cost involved in machining to form complex shapes. An abrasive-grade B_4C powder of surface area of 3 m^2/g was sintered without pressure by Kuzenkova et al and achieved a 95% theoretical density at 2250^{o}C (Kuzenkova et al., 1979).

There have been studies focused on improving the pressureless sinterability of high grade abrasive materials like B_4C and TiB_2 through fine starting particles, a proper sintering schedule, control of oxygen impurities and some additives (Chamberlain et al., 2006). There have been some cases where some additives (Al_2O_3, TiB_2, AlF_3 and W_2B_5) was required while applying pressureless sintering to consolidate powders in order to improve their mechanical properties (Skorokhod et al., 1996, Lee and Kim, 1992, Kanno et al., 1987, Zakhariev and Radev, 1988). However, the addition of boron and carbon as sintering aids have significantly increased the fracture toughness of pressureless-sintered SiC ceramics to 2-3 MPa $m^{1/2}$ (Shih and Opoku, 1979, Faber and Evans, 1983).

Conventional method of sintering usually promotes grain growth which makes it necessary to control sintering temperature, method of heating and time in order to reduce grain growth (Khalil and Almajid, 2012, Kim et al., 2013). However, induction heating sintering has been very effective when applied towards the sintering of ceramics and metallic powders and have successfully attained the theoretical densities of these materials after consolidation (Khalil and Kim, 2006, Khalil and Kim, 2007a, Khalil and Kim, 2007c, Dewidar, 2010). Previous studies has shown the advantages of its quick densification to near the theoretical density of the nanostructural material through the rapid heat transfer to the materials through electromagnetic waves and also reducing the tendency of grain growth as it enhances the mechanical properties of the material (Khalil et al., 2007b, Khalil et al., 2007a, Khalil and Kim, 2007b, Khalil et al., 2007c, Kim and Khalil, 2006).

The electromagnetic field induces current flow into the conductive die and sample thereby allowing the right amount of heat to be applied exactly where it is required at a certain period of time ensuring controlled and accurate performance. More so, the non-contact heating technique prevents the material from being contaminated while heating (Kim and Khalil, 2006). Induction heating sintering involves the sintering of nanostructural materials in a short time under high temperature exposure with the application of pressure (Khalil and Almajid, 2012). Figure 2.7 shows the induction heating session as (a) demonstrates the schematic drawing of the set up and (b) demonstrates the real image.

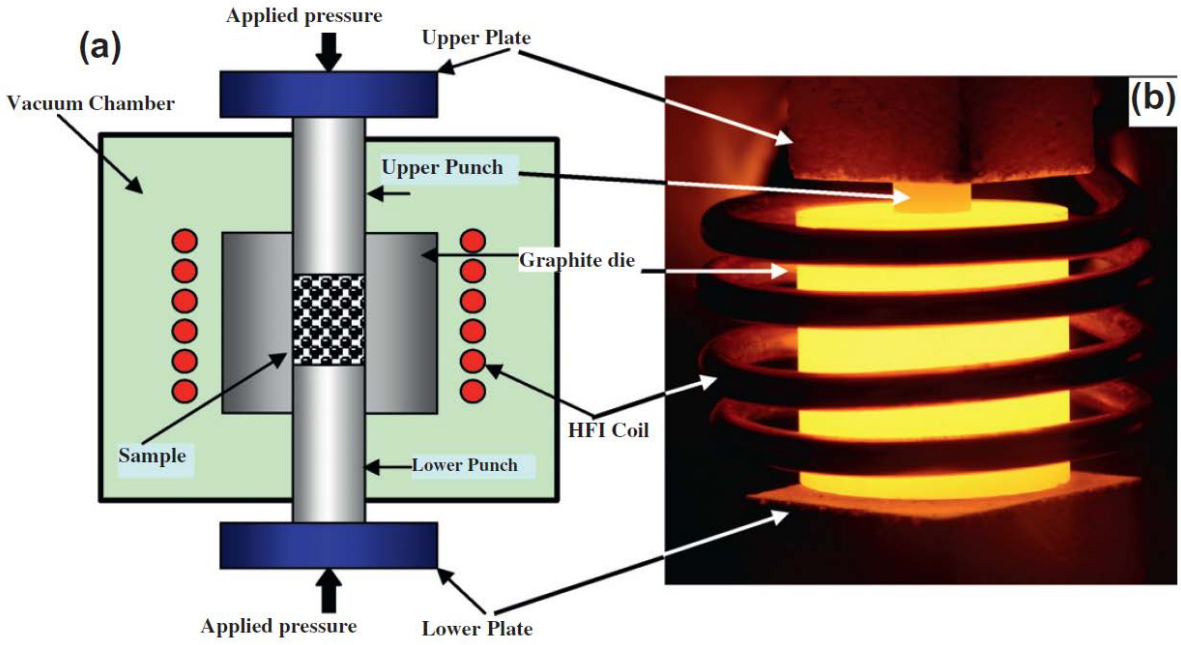

Figure 2. 7: Induction heating sintering (a) Schematic diagram. (b) Real image of the heated die

Generally, nanostructural materials possess better mechanical and physical properties than those of conventional materials especially when applied towards advanced engineering (Jafari et al., 2010, Kim et al., 2013). Carbon nanostructures have high tensile strength, high elasticity, high hardness, high aspect ratio and relatively good ductility and toughness (Iijima, 1991, Rochie, 2000, Fu et al., 2001, Berger et al., 1997) therefore they are attractive materials for the reinforcement of various materials (Xu et al., 2014). They also have strong bonds within their atoms that makes it easier for them to fuse together. In this study, we illustrated the mechanism that was involved in pressureless-sintering of our carbon nanostructures using induction heating. This involves the compaction of fine powders, proper post-sintering design of experiments, and good control of the environment to avoid oxygen impurities. We designed a near perfect method of achieving good sintered

samples as we combined the advantages of both pressureless sintering and induction heating sintering. Our method was able to consolidate the powdered samples at solid state without changing the chemistry of the samples. Conclusively, our sample was able to compact in solid state fusing together particles through our innovative pressureless sintering that was achieved through induction heating without requiring any form of additive.

Chapter 3

3.1 Project methods and process

This chapter introduces an overview of the methodologies applied in this study. It represents details of sample preparations and the processes involved in all the procedures necessary to achieve the desired results. This study applies mechanical milling as the main process to synthesize the material used for sintering and other applications as will be discussed in the subsequent chapter. Sample preparation is very important in this project as it very necessary to get the samples in the conditions necessary for each process. These samples were clearly labeled for reference purposes. In this study, different characterization tools were employed to compare results from known data. Figure 3.1 shows the flow diagram for the design of experiment, testing and analysis conducted throughout this study.

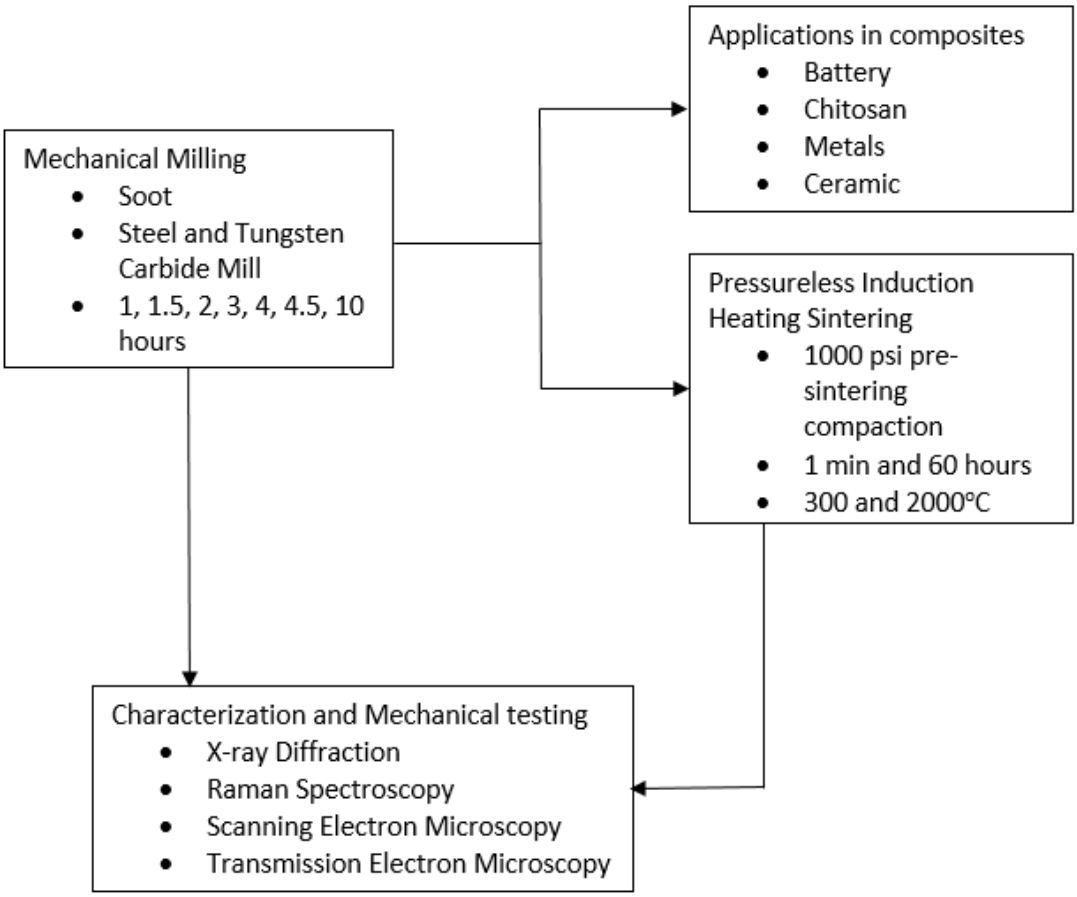

Figure 3. 1: Research flow diagram

3.2 Sample preparation

3.2.1 Mechanical milling

The samples were prepared using the commercially available fullerene soot. This raw material has traces and less than 1% wt. of fullerene as it is the byproduct after the (C_{60}) is extracted and was purchased from SES Research Company. The samples were milled using the SPEX 8000M mixer/mill for times from 0 – 10 hours. Vials of different materials were used to investigate their effect on the *in-situ* synthesis of carbon nano-reinforcement;

1, 2, 4 and 10 hours with steel round end vial and 1.5, 3 and 4.5 hours with tungsten carbide vial as shown in Table 3.1. It was milled in batches of 2 grams.

Table 3. 1: Milled samples with high energy spex mill

Sample Name	Milling Vial	Milling Time
S1	Steel	1
S2	Steel	2
S4	Steel	4
S10	Steel	10
WC1.5	Tungsten Carbide	1.5
WC3	Tungsten Carbide	3
WC4.5	Tungsten Carbide	4.5
Zr1	Zirconia	1
Zr2	Zirconia	2
Zr3	Zirconia	3
Zr4	Zirconia	4
Zr5	Zirconia	5

3.2.2 Sintering

The samples used for the pressureless induction heating sintering were milled samples except those milled with zirconia. This exception was due to high level of contamination from the walls of the milling vial and balls. The samples with little to no contamination were selected in batches of 350 mg each. Each of these samples was pre-compacted using pressure of 1000 psi and dried prior to sintering. Table 3.2 shows the list of the samples that were sintered in relation to the sintering temperature.

Table 3. 2: Pressureless induction heating sample preparation

Sample Name	Milling Time (hours)	Substance	Sintering Temperature (^oC)	Sintering Time (minutes)
S1	1	Soot	300	1
S1	1	Soot	2000	1
S2	2	Soot	300	1
S2	2	Soot	2000	1
S4	4	Soot	300	1
S4	4	Soot	2000	1
S10	10	Soot	2000	1
S10	10	Soot	2000	10
S10	10	Soot	2000	60
WC1.5	1.5	Soot	300	1
WC1.5	1.5	Soot	2000	1
WC3	3	Soot	300	1
WC3	3	Soot	2000	1
WC4.5	4.5	Soot	300	1
WC4.5	4.5	Soot	2000	1

The sintering process used in this work is a new method developed by our group and it is in process of patenting. This process involves the making of a die and two punches from niobium pipe and rod respectively at a length of 1cm each. The inner diameter of the niobium pipes was smoothened by sanding through the hollow pipes to allow free passage of the niobium rods. The niobium rods were reduced in their outer diameter to ensure that the two punches can freely pass through the hollow pipes. This was done in preparation for the compaction of the sample to prevent the punches from getting stuck in the pipe after compacting of the sample due to deformation from the applied pressure. Figure 3.2 shows the die and punch, made with niobium pipe and rod respectively, used in this study.

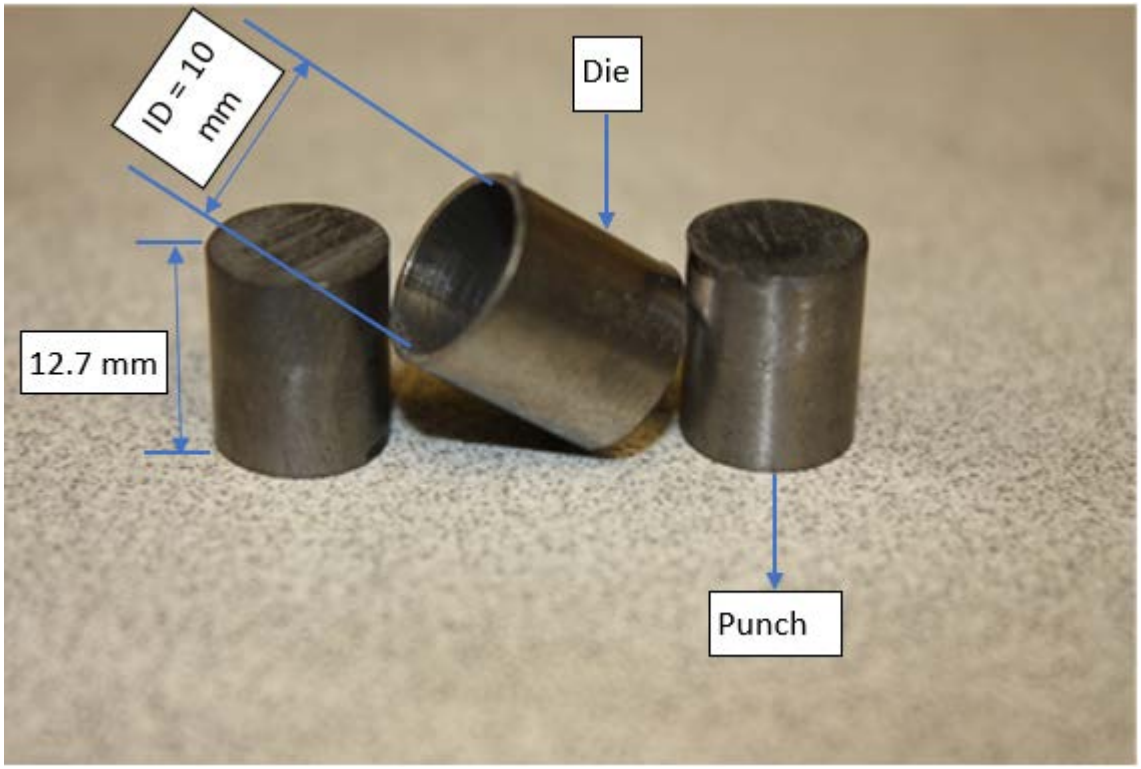

Figure 3. 2: Die and punch for sintering

Each of the samples was pre-compacted using a hydraulic press to apply a pressure of 1000 psi. Since the purpose of this sintering process is to obtain a consolidated sample at solid state with pressure while heating, it was very necessary to compact the sample prior to heating because compaction expedites diffusion of the atoms while heating. Figure 3.3 shows the hydraulic press used for this study, which was made by Carver Laboratory Press. The insets in the picture show a closer look at the applied pressure on the sample and the die and punch holding the sample for compaction.

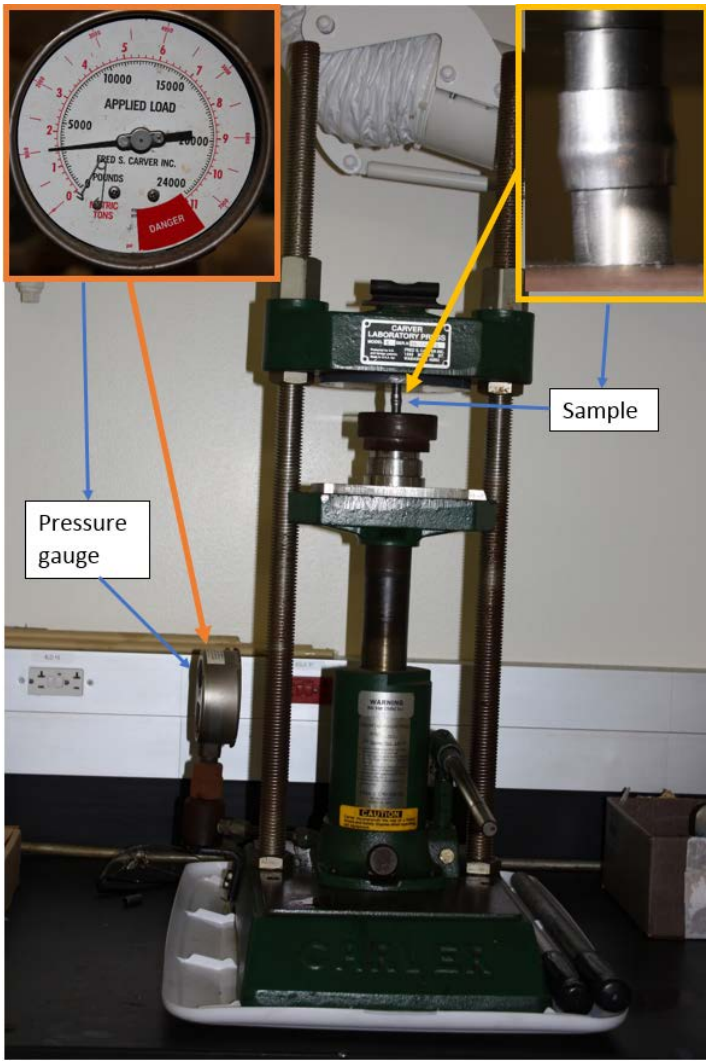

Figure 3. 3: Hydraulic press (insets showing the applied pressure and compacting die and punch

The compacted sample, still in the die, was vacuumed in a quartz tube sealed off at the upper end. The vacuumed chamber is connected to the quartz tube through the neck that has an on/off knob for air inlet/outlet. After compaction the sample was dried up in vacuum at a low temperature of 200^{o}C with the heat applied to the lower part of the quartz tube through a resistance heating system. The samples are dried to remove moisture in the compact. The drying is done in vacuum to prevent oxidation and contamination of the

sample. The processes of compaction and drying the sample were done twice subsequently to ensure better compaction of the sample after drying. Figure 3.4 shows the vacuum system as the sample is been dried and vacuumed at the same time to eliminate trapped moisture and avoid oxidation while sintering.

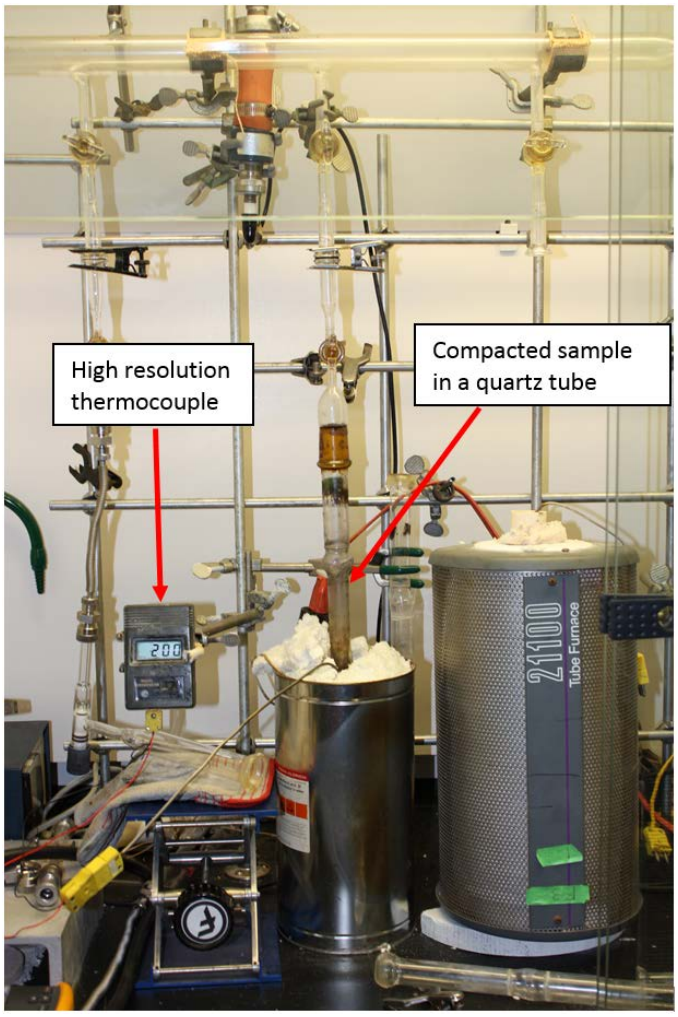

Figure 3. 4: Drying a sample at a low temperature

The second part for the pressureless sintering of the sample is the heating of the sample. There are two processes involved in this procedure which are sintering at low temperature using the resistance heating system and sintering at a very high temperature

using the induction heating system. For the low temperature sintering, the sample is sintered at 300^0C under vacuum for 1 minute. The source of the heat is from a resistance heating furnace for low temperature. This same heating system is used for drying the sample but the difference is that both processes are done at a different temperature.

The second process involves sintering with high temperature using an induction heating furnace. The sample, still in vacuum, dried and compacted, will be connected to the high frequency induction heating system. Held firmly at the upper end of the quartz tube, the lower end is passed through the coil of the induction heating system. The electromagnetic force from the coil induces eddy currents to the electrical conductive die (niobium) and the resistance causes the heating of the niobium. The sample is heated at an increment of 200^{o}C per 10 seconds until it reaches 600^{o}C before the temperature is raised to 2000^{o}C and held for a minute. The material is allowed to cool after the sintering. With the help of another niobium rod, the sintered sample is pushed out from the die. Figure 3.5 shows the sample in a vacuum tube as it is heated using an induction heating system to 2000^{o}C while sintering without pressure. Figure 3.6 shows the consolidated samples with their dimensions.

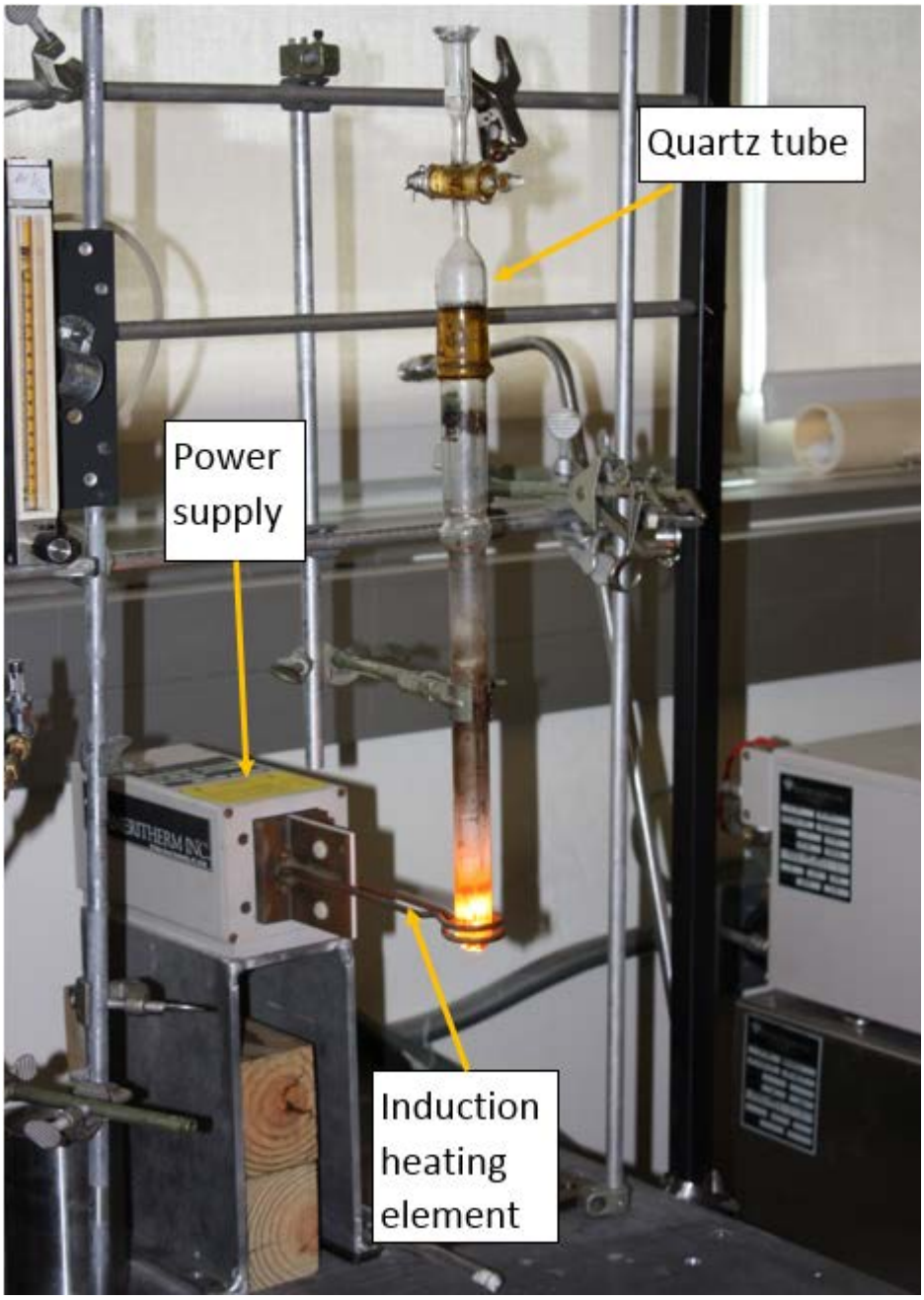

Figure 3. 5: Pressureless sintering of the sample using induction heating system

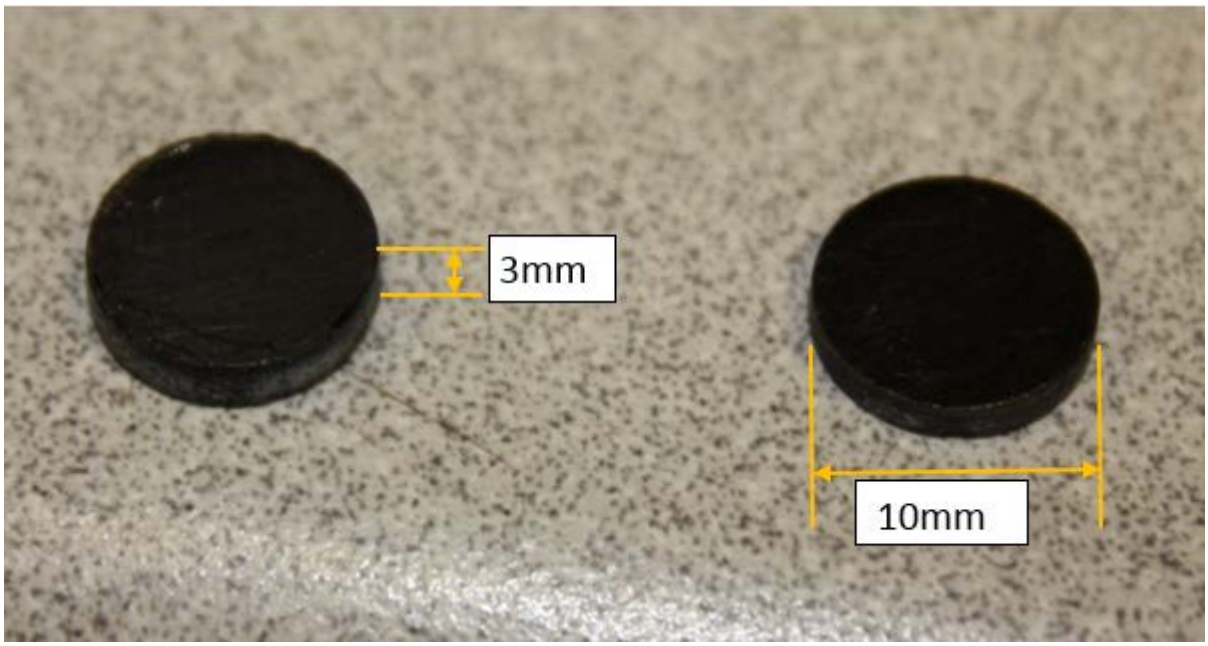

Figure 3. 6: Sintered samples

3.3 X-ray diffraction (XRD)

X-ray powder diffraction (XRD) is a rapid analytical technique primarily used for phase identification of a crystalline material and can provide information on unit cell dimensions (Merritt and Streib, 1964). This tool works by the diffraction of x-rays in a manner as described by the Bragg's law and their incident beam as,

$$n\lambda = 2d \sin\theta \quad \text{.....Equation 3.1.}$$

Where d is the interplanar spacing, θ is the incident angle, λ is the incident beam wavelength and n is an integer. The angle at which each peak appears in the spectrum as gotten from the result of the diffraction is the solution to the Bragg's equation for the interplanar distance and it's specific to each material which can be compared to a database managed by the International Center of Diffraction Data. Figure 3.7 shows a computer sketch of the Bragg's

law as the incident beam hits the atoms of a substance with their interplanar distance clearly shown

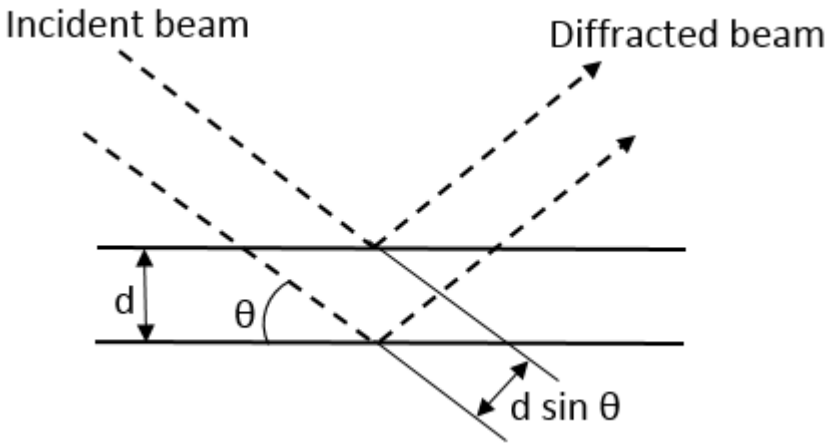

Figure 3. 7: Bragg's law demonstration

XRD was one of the characterization techniques used in this study. It is the fundamental tool used for studying the stacking of carbon nanostructural layers, interatomic plane distances and the constituents of a material, and the lattice parameters.(Brooker and Nuffield, 1966, Seung Hun et al., 2010). The carbon stacking structure can be calculated using the following structural parameters which includes the fraction of amorphous carbon (χ_A), aromaticity (f_a), interlayer spacing of the crystalline structure (d_{002}) and crystallite sizes (L_a and L_c) (Manoj and Kunjomana, 2012). A constructive interference occurs as the interplanar distance of the atoms are arranged in symmetrical pattern that synchronizes with the source of the x-ray thereby obeying the structural factor (Kennedy and Thorley, 1999).

In this study, XRD was used to determine the grain size of our material, interlayer spacing and stacking of the nanostructural layers present in each material. The XRD

machine was set to shoot incident beam of x-ray at a range of angle (10^o – 90^o). The parameters utilized for the XRD measurement in this study is shown in Table 3.3

Table 3. 3: Operating parameters for D5000 diffractometer

Parameter	Value
Voltage	30V
Current	40A
Diffraction Angle	10° - 95°
Exposure Time	1second per step
Cu tube with (λ)	0.154nm

3.3.1 Grain size calculation

In order to calculate the grain size of the sample, Scherrer's equation was used.

$$\tau = \frac{K\lambda}{\beta \cos\theta} \quad \text{.....Equation 3.2,}$$

where:

K is the shape factor

θ is Bragg's angle

λ is the incident beam wavelength, 0.154 nm

β is the full width half maximum

τ is the grain size

This equation illustrates the size of a nanoscale powder utilizing the broadness of the peak from a diffraction pattern (Patterson, 1939). Figure 3.8 illustrates the parameters required for grain size determination using the Scherrer's equation as β is the parameter used in the Scherrer equation to determine grain size. The data from the XRD was analyzed using Origin 8 to get the full width half maximum data of the spectrum.

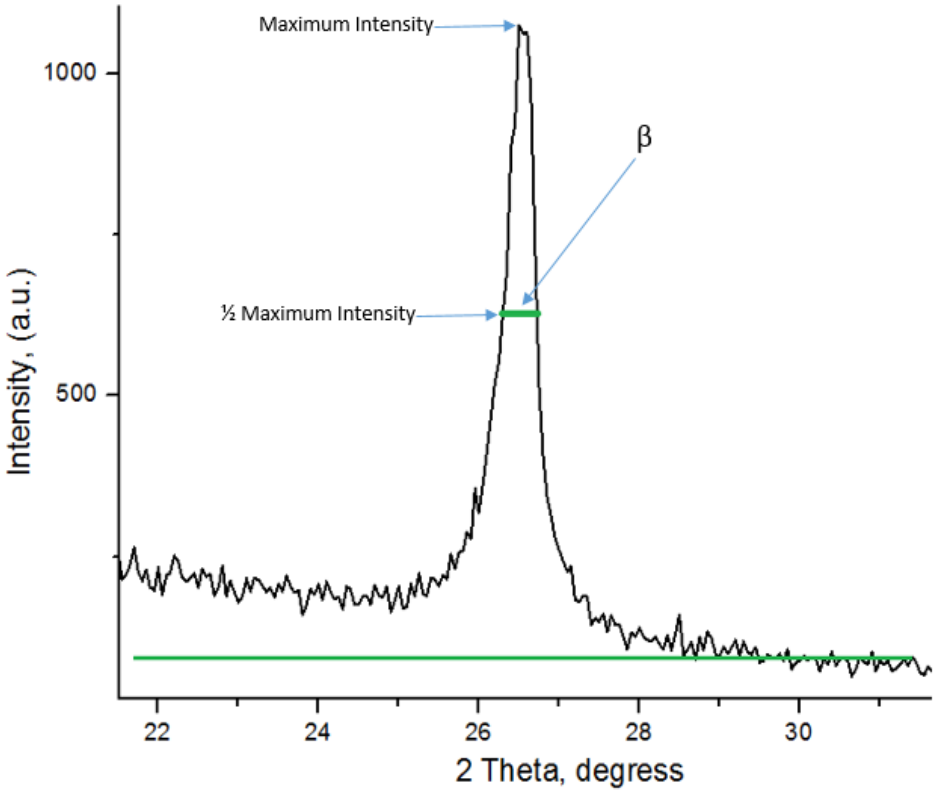

Figure 3. 8: XRD reflection showing the principal characteristics on the XRD peaks required for Scherrer's Equation

3.4 Raman spectroscopy

Raman spectroscopy was invented by Sir C. V. Raman with which he won a Nobel Prize in Physics in 1930 (Gardiner, 1989). Raman spectroscopy has become the most suitable tool used in the analysis of carbon based nanostructures (Jorio et al., 2011). It is also very sensitive in probing disorder in carbon nanostructures. Raman spectroscopy can be used to differentiate many types of sp^2 carbon structures and also for the identification of defects. (Ferrari and Robertson, 2000, Pimenta et al., 2007). Defects can be of importance due to their ability to modify the electronic and optical properties of a system.

Application of Raman has broaden over time; ranging from chemistry, security industry to medical applications. Portable devices that possess much quicker processing and integrated imaging hardware and software have been developed for Raman measurements which broadens the general usage of the technique for characterization purposes (Barber, 2013). Figure 3.9 shows the Horiba Raman spectrometer that was used for this study with an inset showing the integrated computer system which operates the machine using a software called LabSpec 5. Table 3.4 shows the parameters used for the Raman measurements.

Figure 3. 9: Horiba spectrometer and inset showing the integrated computer system

Table 3. 4: Raman measurement parameters

Parameter	Value
Laser	Solid state: YAG laser 532 nm 638 nm 7
Optical zoom	1000x

3.4.1 Raman spectroscopy data collection

Raman measurements were made using the Horiba spectrometer with an integrated optical and computer system. The data collected from the measurement was plotted in a spectrum of intensity against Raman shift in energy levels that was plotted in unit of 1/cm. The data obtained was used to demonstrate the synthesis that occurred as a result of different milling times and medium. The sintered samples were prepared by polishing to obtain a smooth surface with no contaminant for better Raman measurement. The powder samples doesn't require special preparation for Raman measurement. The data were further analyzed for the crystallite sizes and level of disorder.

3.5 Scanning electron microscopy

Scanning Electron Microscopy (SEM) examines the surface composition of a sample using an electron beam and the reflected beam of electrons are collected and displayed as images on a cathode ray tube at the same scanning rate (McMullan, 2004). The equipment transmits beam of electron through stacks of lenses focusing on an area in the sample to produce signals which include secondary electrons, cathodoluminescence, specimen current, backscattered electrons, characteristics x-ray and transmitted electrons (Poelman and Smet, 2014, Gheriani et al., 2010, Seiter et al., 2014, Sich et al., 1989). These signals produced depends on the standard equipment used and are produced from interactions of electron beam with atoms at or near the surface of the sample. As backscattered light passes through the circular rear aperture of the objective lens and hits the surface of a specimen, the various points of a specimen displays in image as small

patterns. The resolving strength of a microscope can be determined by the limit to which different small objects are seen as separate substance (Goldstein et al., 2003). SEM displays the surface features of a sample to a magnification ranging from 10 to an excess of 300,000. Figure 3.11 shows the working mechanism of the SEM.

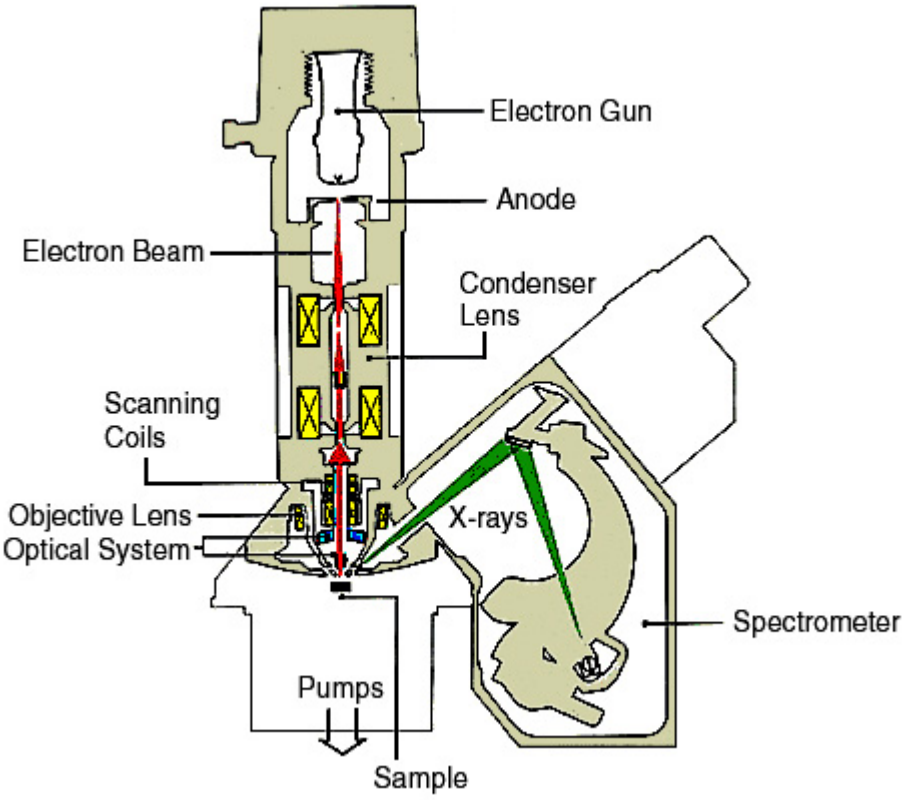

Figure 3. 10: SEM working mechanism (As taken from[§§§])

3.6 Transmission electron microscopy

In this study, TEM was employed to analyze the samples for imaging diffraction and high resolution. Bright field, diffraction and high resolution were applied for analysis in this

[§§§] http://www4.nau.edu/microanalysis/Microprobe-SEM/Instrumentation.html

study to illustrate the atomic lattices. These results were compared to the theoretical values for interplanar distances and crystal structure. Figure 3.13 shows the TEM that was used for this study. It is located at Texas Center for Superconductivity, University of Houston (TcSUH). Table 3.5 shows the parameters that was used for the TEM.

Table 3. 5: TEM operational parameters

Parameter	**Value**
Resolution	UH – 0.2nm, LBNL – 0.05nm
Exposure Time	Automatic
cuumed chamber	10^{-5} Pa

Chapter 4

4.1 Results

In this chapter, we illustrate the results obtained from this study. We begin with a full description and characterization of the raw and further synthesis of the new materials. We also show the results from the characterization of these new materials using Raman measurements and XRD. Detailed information about their applications and results gotten from testing of these applications follows subsequently. Other techniques applied for characterization such as SEM and TEM is included for additional confirmation of results.

4.2 Fullerene soot

In this project, we recognize our raw material as fullerene soot and should further be referred as so. The raw material has been characterized to have a limited crystallinity. This raw material was characterized and results presented here to be able to recognize further changes as a result of mechanical milling and sintering as we go further into analysis of results gotten from this study. The raw material is a commercially available fullerene soot as purchased from SES Research which still contains about 1 %wt of fullerene as it is a byproduct from the known process of evaporation of fullerene through Krätschmer method (Kratschmer et al., 1990). Table 4.1 shows the grain size and lattice parameters of the raw material.

Table 4. 1: Crystalline characteristics of material as determined by XRD (Fals et al., 2012a, Robles Hernandez and Calderon, 2012)

Commercial fullerene lattice parameter (nm)	
C_{60}	1.437
C_{70}	1.924
Grain Size (nm)	
Soot	~40

XRD analysis performed on the raw material is shown in Figure 4.1. It is compared to the results from the pure fullerene (C_{60}). Fullerene reflections are present in the raw material but not so clear as it almost incorporates with the background. This reflection as compared with the background is a proof of the material's limited crystallinity. It is also as result of the presence of less than 1 wt% C_{60} as described by the manufacturer in the XRD spectrum of the raw material. Figure 4.1 shows the comparison of the raw material and pristine quality fullerene (mainly C_{60}) as compared using XRD results.

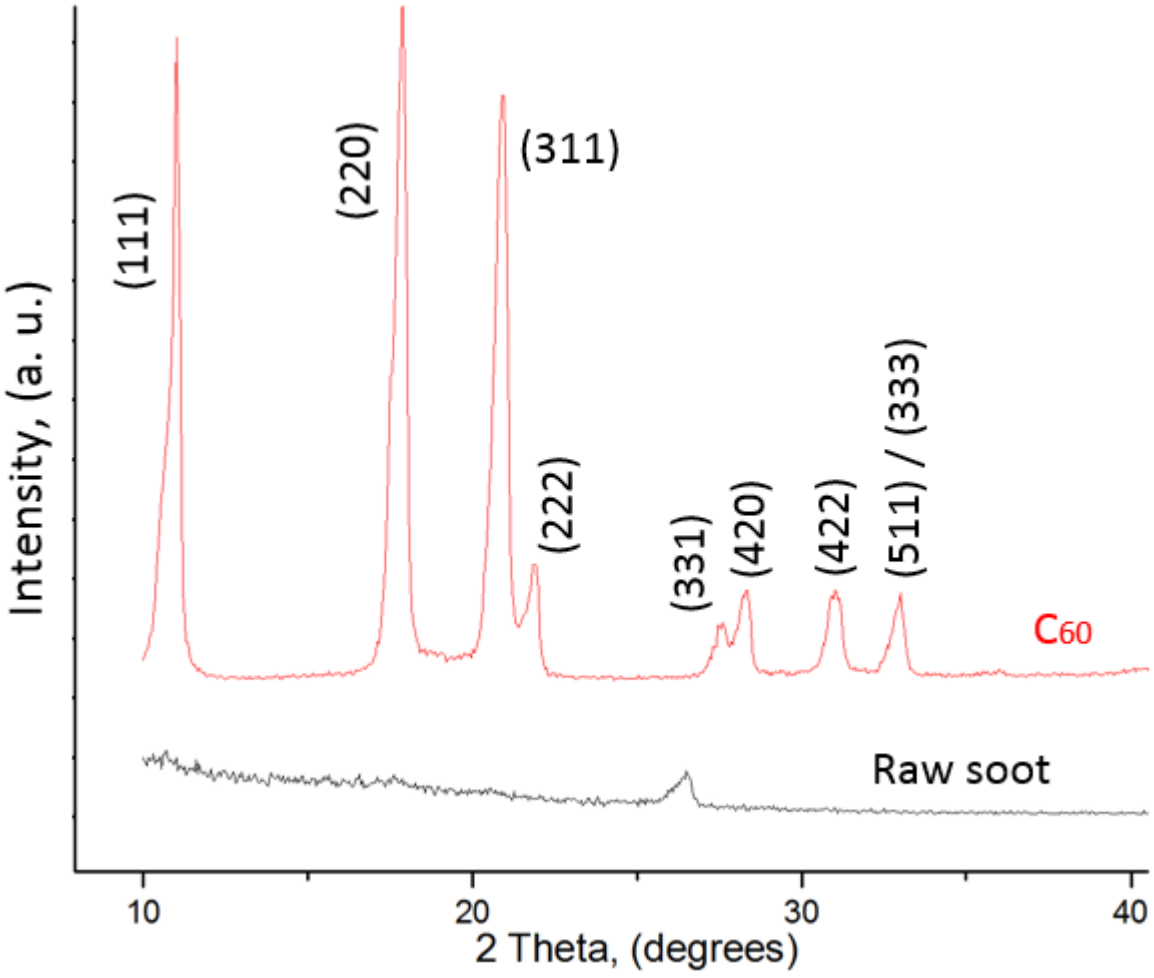

Figure 4. 1: XRD comparison of raw soot and pure fullerene

Further analysis were performed using Raman measurements as the raw material is compared to pure fullerene to support the results gotten from XRD. The Raman spectra shows that the raw material has graphitic particles due to the presence of D and G band. The D band, also known as disorder band, in the raw material is clearly seen showing that there is large presence of defect in the material. The Raman results shows both materials have their G band at the same point (1578). It is clearly noted in Figure 4.2 that the raw material possesses no graphene or graphitic carbon as there is no presence of 2D band. Figure 4.2 shows the Raman spectra of the raw material as it is compared with pure C_{60} and analyzed for the presence of graphene.

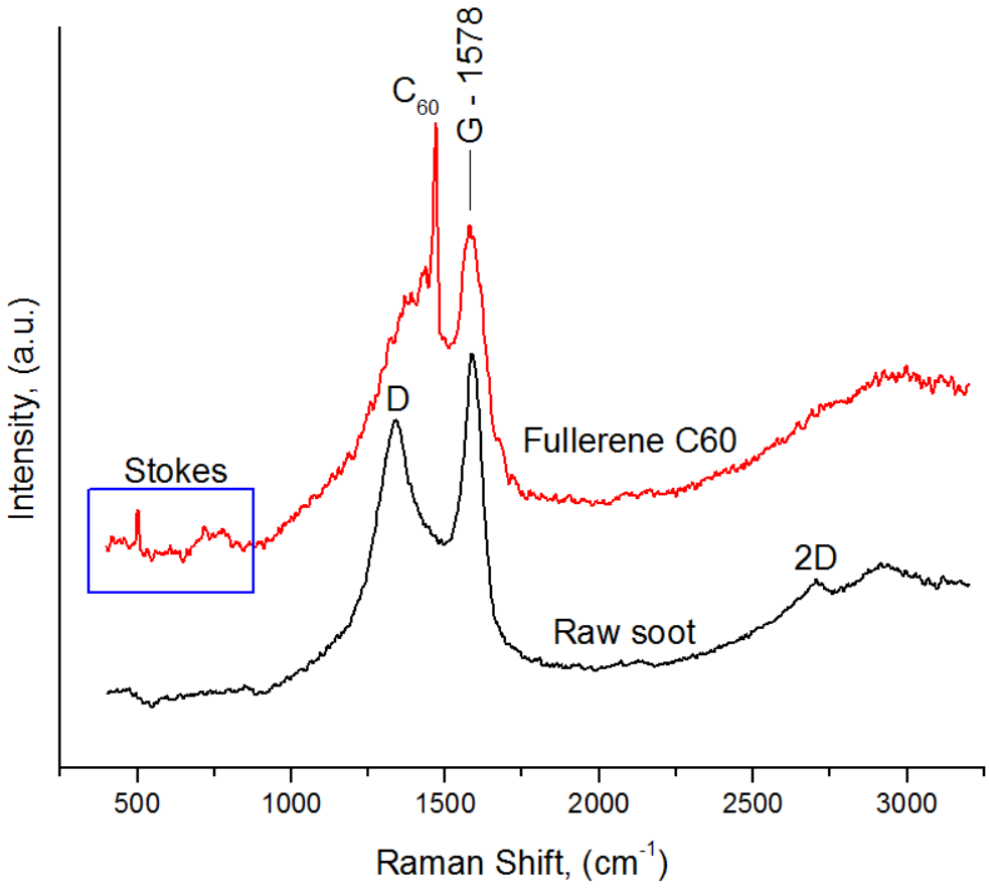

Figure 4. 2: Raman spectra for comparison between Fullerene C_{60} and raw material

The raw material was scanned with the SEM and images taken are shown in Figure 4.3. The image shows the scattered carbon particles in a wooly form telling the story of a residue of an evaporation process. At most part, it seems like it is in agglomeration due to the property of the material (Van Der Waals forces) that makes it to form a “cluster” of itself. Figure 4.3a shows a lower magnification and Figure 4.3b shows a high magnification image of the raw material as taken from the SEM.

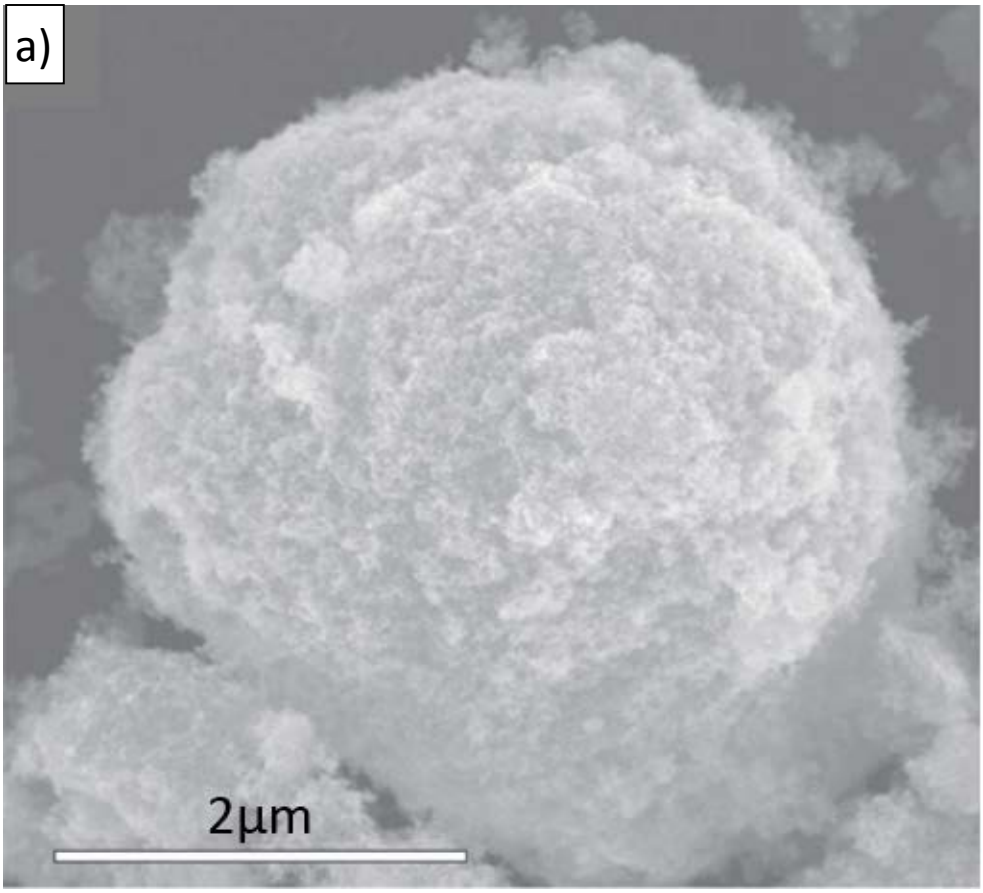

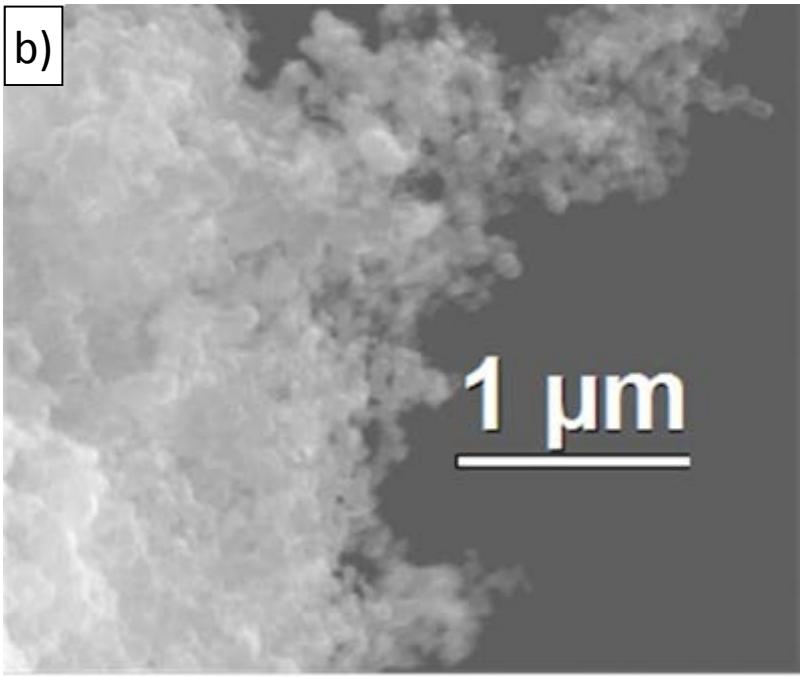

Figure 4. 3: SEM image of the raw material

The raw material was further observed under the TEM and the collected images proved the results of the XRD showing that the raw material is of limited crystallinity. Figure 4.4 shows the high resolution images collected from the TEM. It is evident that the clusters shown in Figure 4.3 are agglomerates of nanoparticles of carbon.

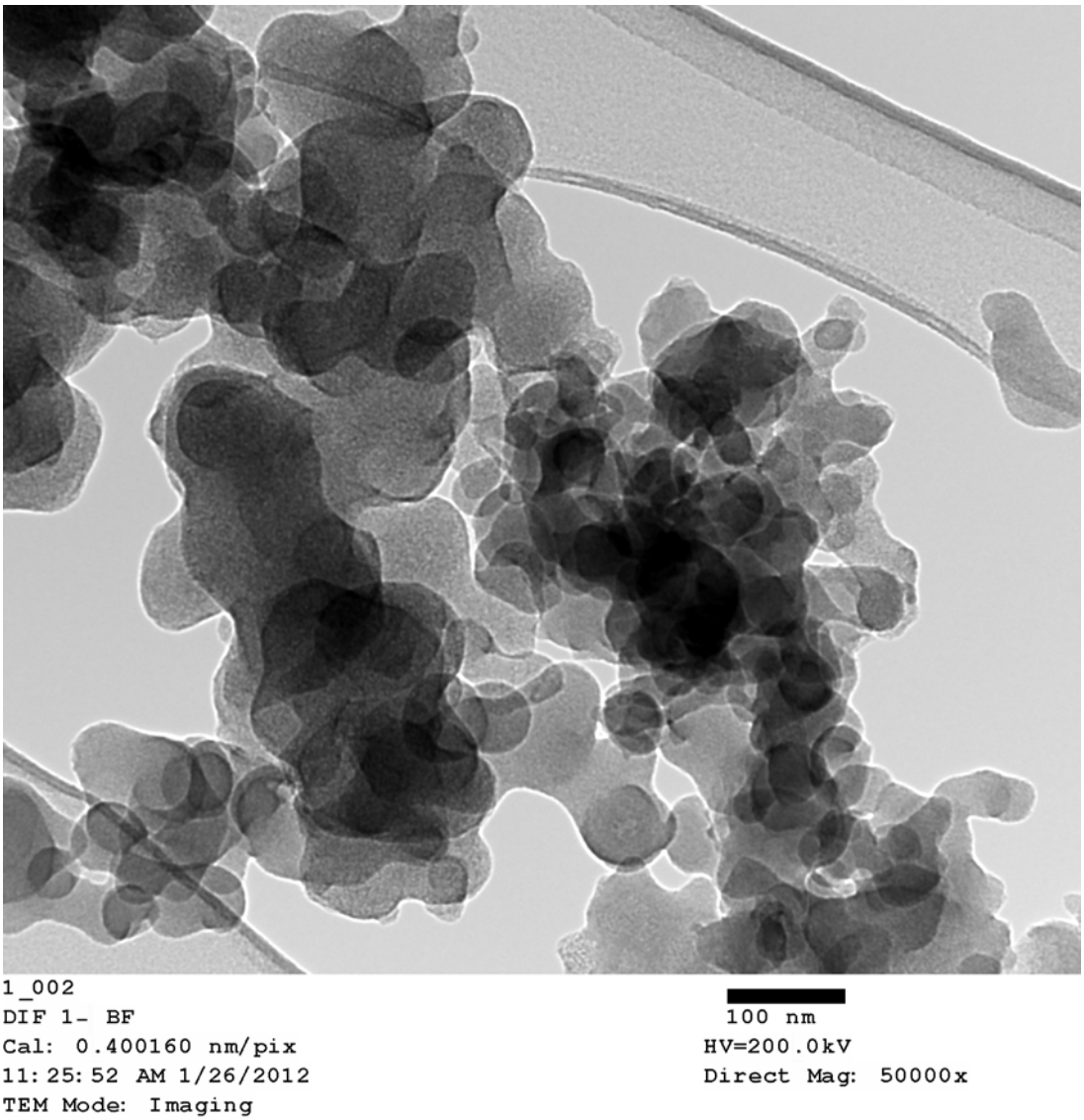

Figure 4. 4: TEM image of the raw material

4.3 Milled soot

Samples were milled from 1 hour to 50 hours to illustrate the synthesis present as a function of milling times. Raman measurements were carried on some milled samples to show the synthesis and the effects of milling media and times. Observing the synthesis of these carbon nanostructures, we found out that as the sample is milled, the D and G band begins to develop. This phenomena is unique and have not been reported in any literature. This is a unique process and indicates the fact that mechanical milling is capable of inducing crystallization of carbon soot into complex structures such as graphitic carbon and graphene. Figure 4.5 shows the Raman spectra for steel vial; Figure 4.6 shows the Raman spectra for tungsten carbide vial and Figure 4.7 shows the Raman spectra for zirconia vial. The scales are shown in the spectra representing the same arbitrary number for the intensity of the peaks. This is to understand the behavior of the peak intensity with respect to milling times.

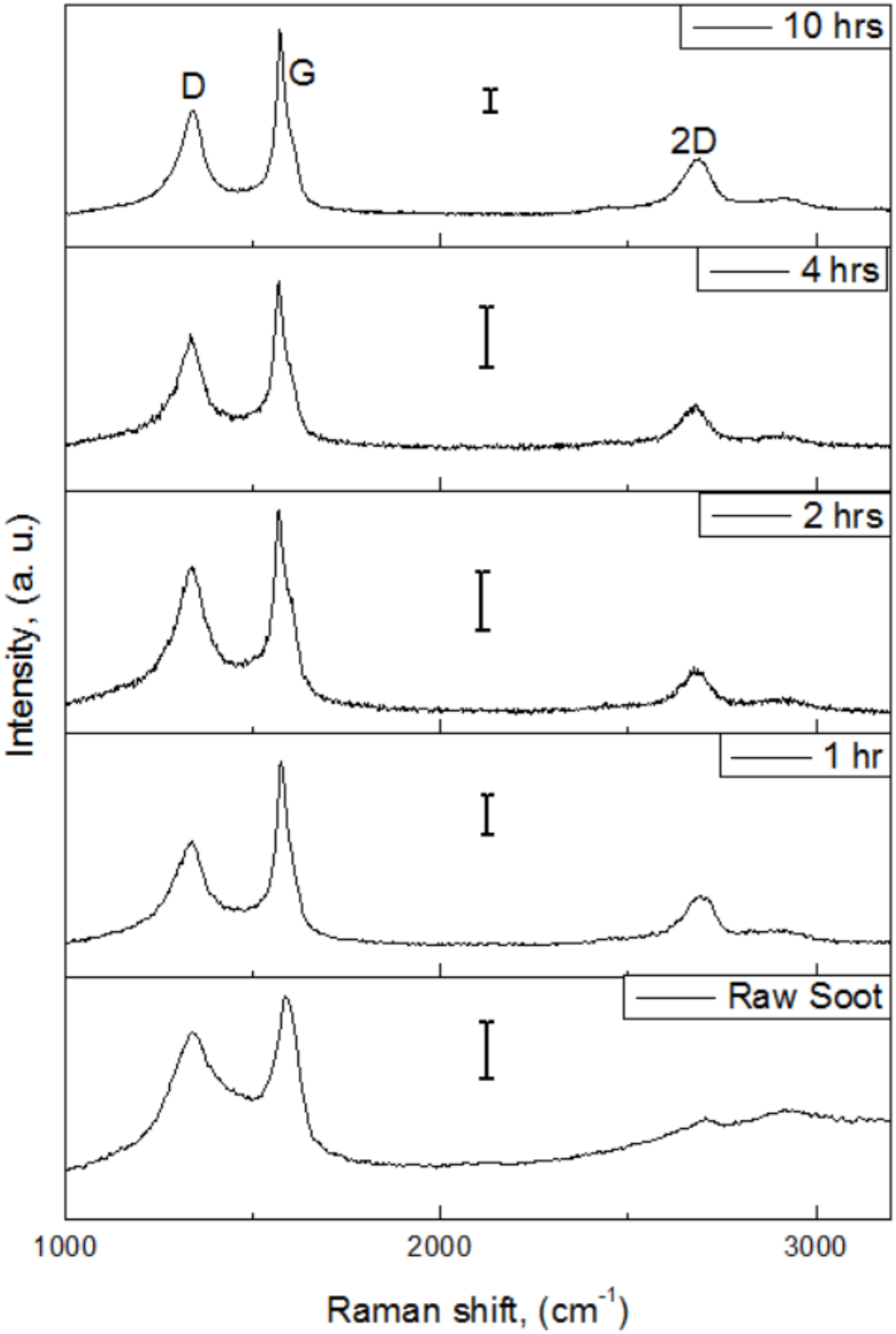

Figure 4. 5: Raman spectra for steel milled samples

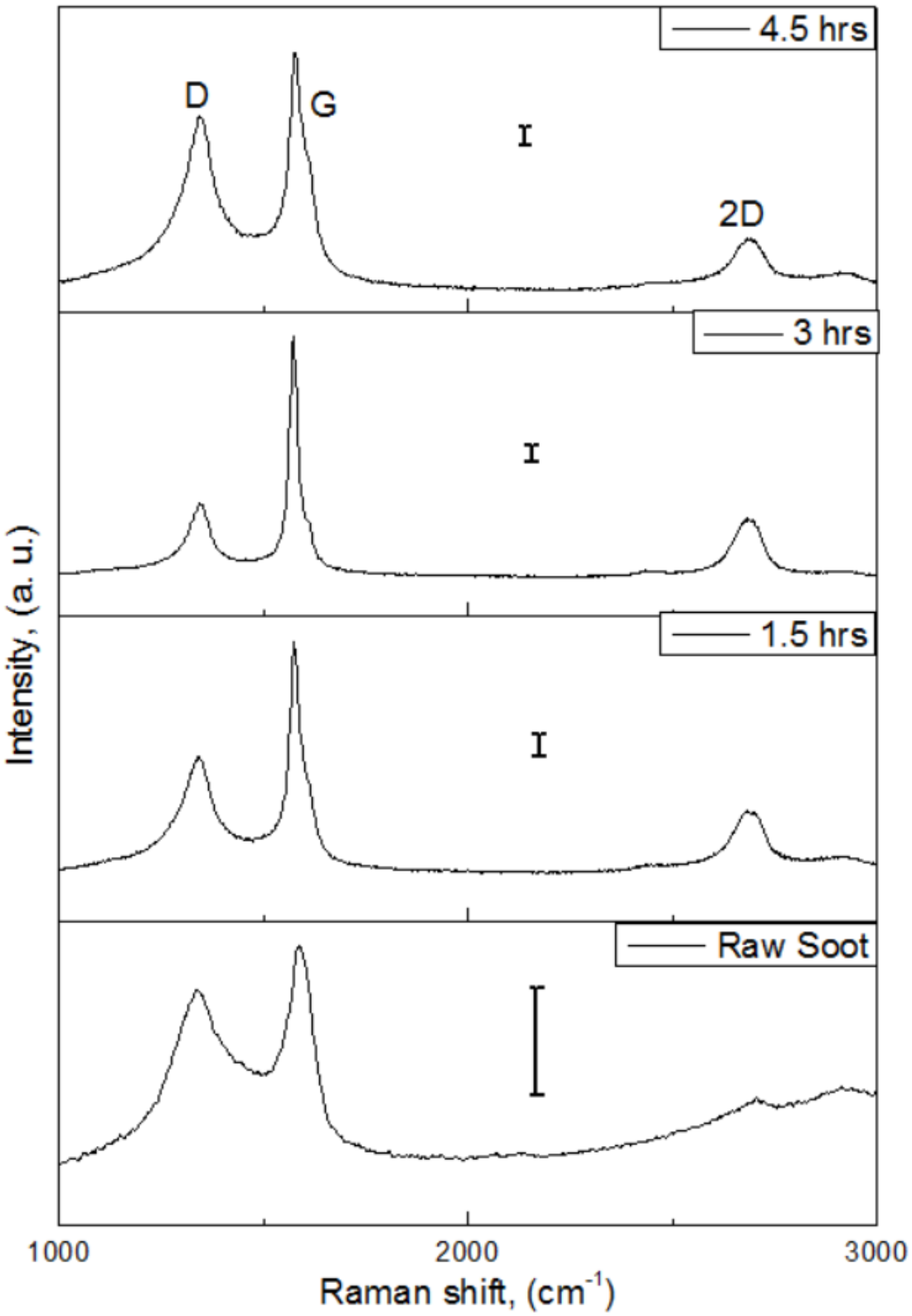

Figure 4. 6: Raman spectra for tungsten carbide milled samples

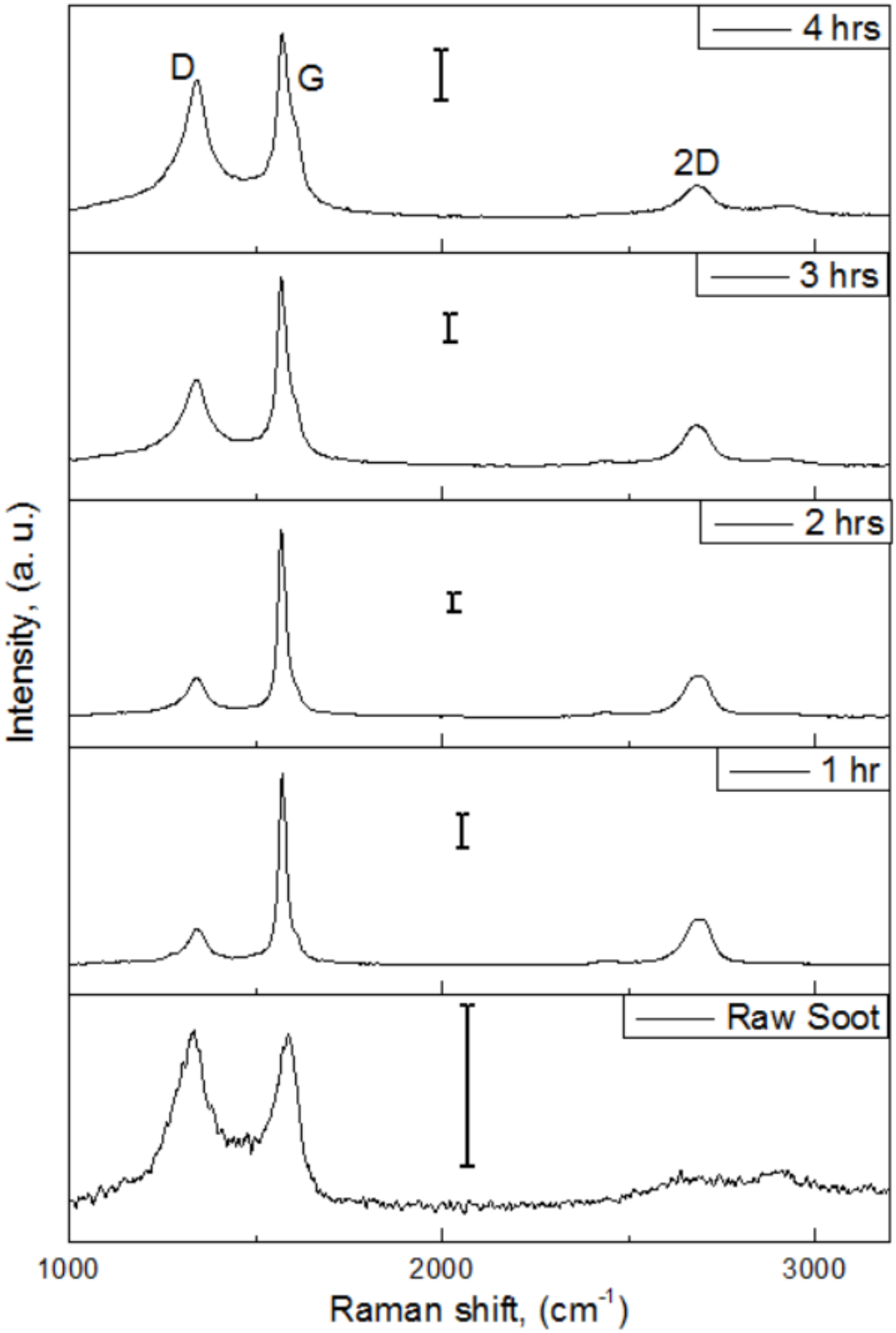

Figure 4. 7: Raman spectra for zirconia milled samples

Due to the high level of contamination of the samples milled with zirconia, we didn't go further with characterization of these samples. This contamination came from the wall of the milling vial and the milling media. It was determined through the weight of the sample after milling which resulted in some samples having about 12% increase in weight after milling notwithstanding the possibilities of sample loss due to handling. Table 4.2 demonstrates the contamination level of the milled samples as it is calculated with the weight of the sample before and after milling.

Table 4. 2: Milled samples weight assessment

Sample Name	Milling Vial	Milling Time (hour)	Weight Before Milling (gm)	Weight After Milling (gm)	Weight change (%)
S1	Steel	1	2	1.9	-5
S2	Steel	2	2	1.93	-3.5
S4	Steel	4	2	2.03	1.5
S10	Steel	10	2	2.1	5
WC1.5	Tungsten Carbide	1.5	2	2.06	3
WC3	Tungsten Carbide	3	2	2.10	5
WC4.5	Tungsten Carbide	4.5	2	2.13	6.5
Zr1	Zirconia	1	2	2.12	6
Zr2	Zirconia	2	2	2.15	7.5
Zr3	Zirconia	3	2	2.19	9.5
Zr4	Zirconia	4	2	2.21	10.5

It is necessary that the Raman spectra (as shown in Figure 4.3 and 4.4) of the samples with little or no contamination are analyzed to illustrate the material with better composition of nanostructural particles and the material with the best ratio of D band intensity to 2D band intensity. The D band, 2D band intensity ratio helps to determine the intrinsic properties of graphene which is the key to its structural applications (Frank et al., 2007).

The intensity ratio of the G, D and 2D bands are necessary in Raman spectroscopy due to their tendency to compute the graphene crystallite sizes as they relates to some disorder present in graphene which is shown in Equation 4.1.

$$La\ (nm) = \ 2.4 * 10^{-10} * A^4(I_G/I_D)$$…….Equation 4.1,

where La is the particle size, A is the excitation energy, I_D and I_G are the Raman intensity of the D and G bands respectively (Cancado et al., 2006).

These band intensity is also necessary for the determination of arrangement (zigzag or armchair) of the atomic structure at the graphite edges with previous works having shown that the absence of D band is a clear indication of a zigzag arrangement while a small or non-null D band shows a non-perfect zigzag or armchair (Cancado et al., 2004, Neubeck et al., 2010). These analysis were done using Origin 8. We have to analyze these spectra to be independent of each other in terms of their hierarchal intensity to be able to get a better picture of what we want to illustrate in this analysis. Figure 4.8 shows the intensity ratio analysis for the samples milled with steel while Figure 4.9 shows the intensity ratio analysis of the samples milled with tungsten carbide vial.

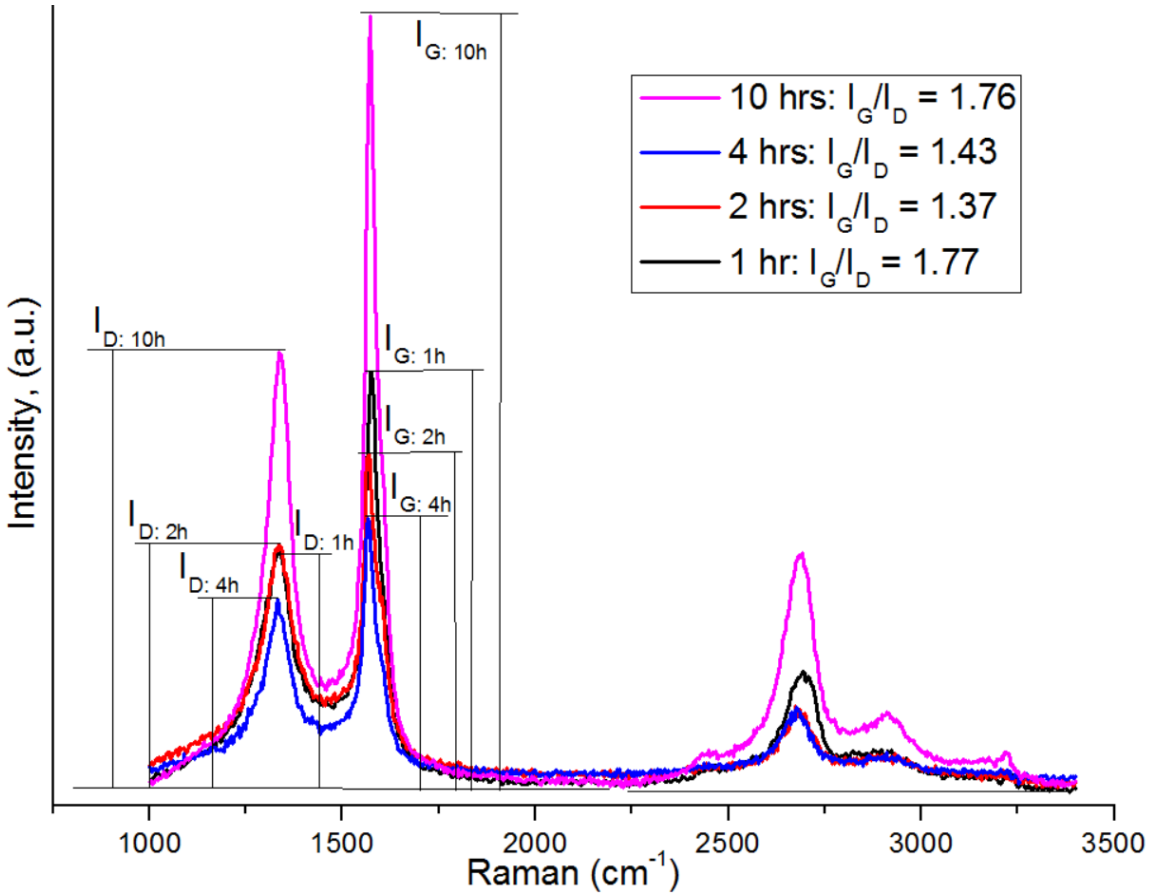

Figure 4. 8: Intensity ratio analysis of steel milled samples

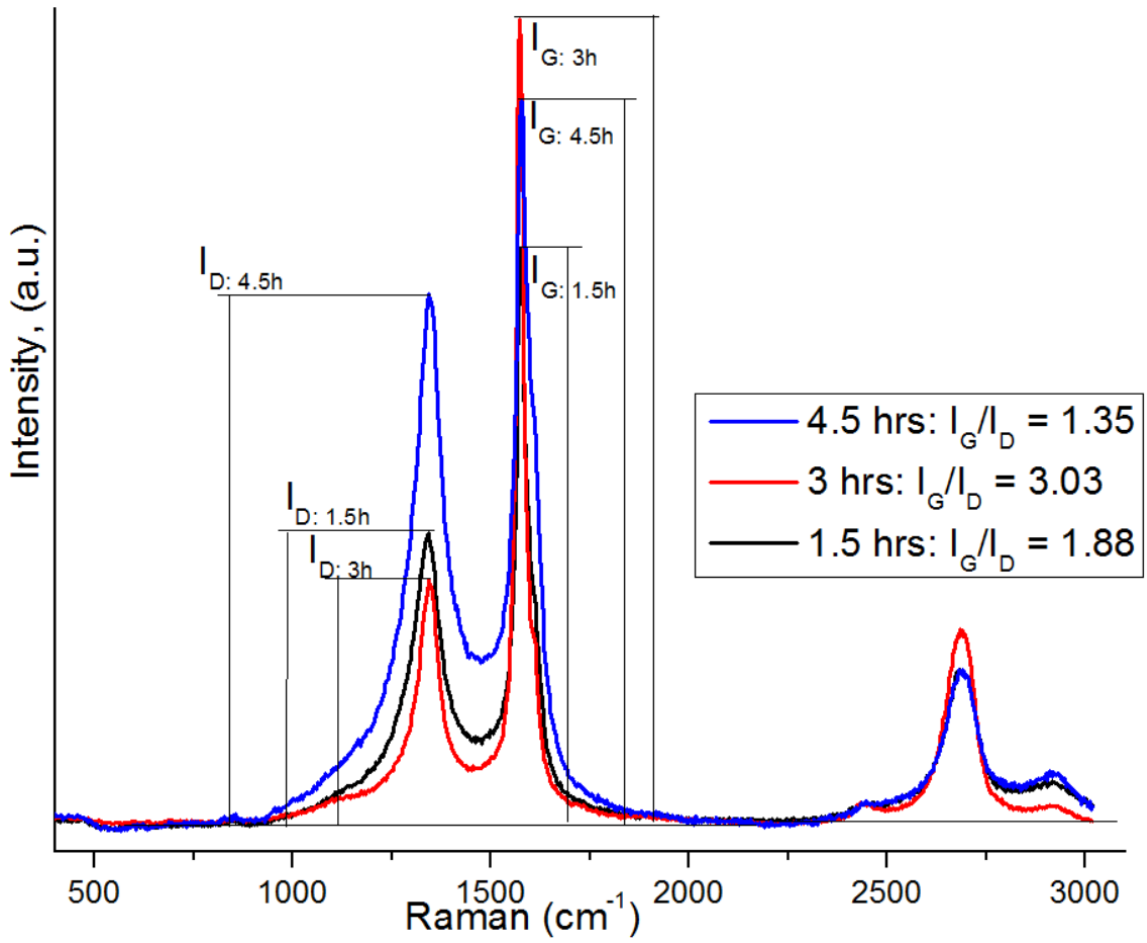

Figure 4. 9: Intensity ratio analysis of tungsten carbide milled samples

The high intensity in the 2D band especially for the samples milled for 1 and 10 hours with steel vial and 3 hours with tungsten carbide is an evident of graphitic carbon that was fractured that leads to the development of graphene. With 2D band peaks being important in carbon based material (Barber, 2013) and carbon nanostructures being identified with their 2D band around 2600 cm^{-1} (Jones, 1996), we can demonstrate the presence of complex carbon nanostructures in the milled samples. Furthermore, 2D band of graphene is usually of high intensity and could dominate the 2D spectra (Fals et al., 2013) thereby showing that there are presence of graphene or graphitic structures in the above

mentioned samples due to their strong well defined 2D band peak with intensity close to that of their D band. The sample milled with steel vial for 1 hour was further observed using the HRTEM and the image shown in Figure 4.10 illustrates the presence of graphene. Figure 4.10 shows the TEM image of graphene layers as observed in the sample milled for 1 hour using steel vial.

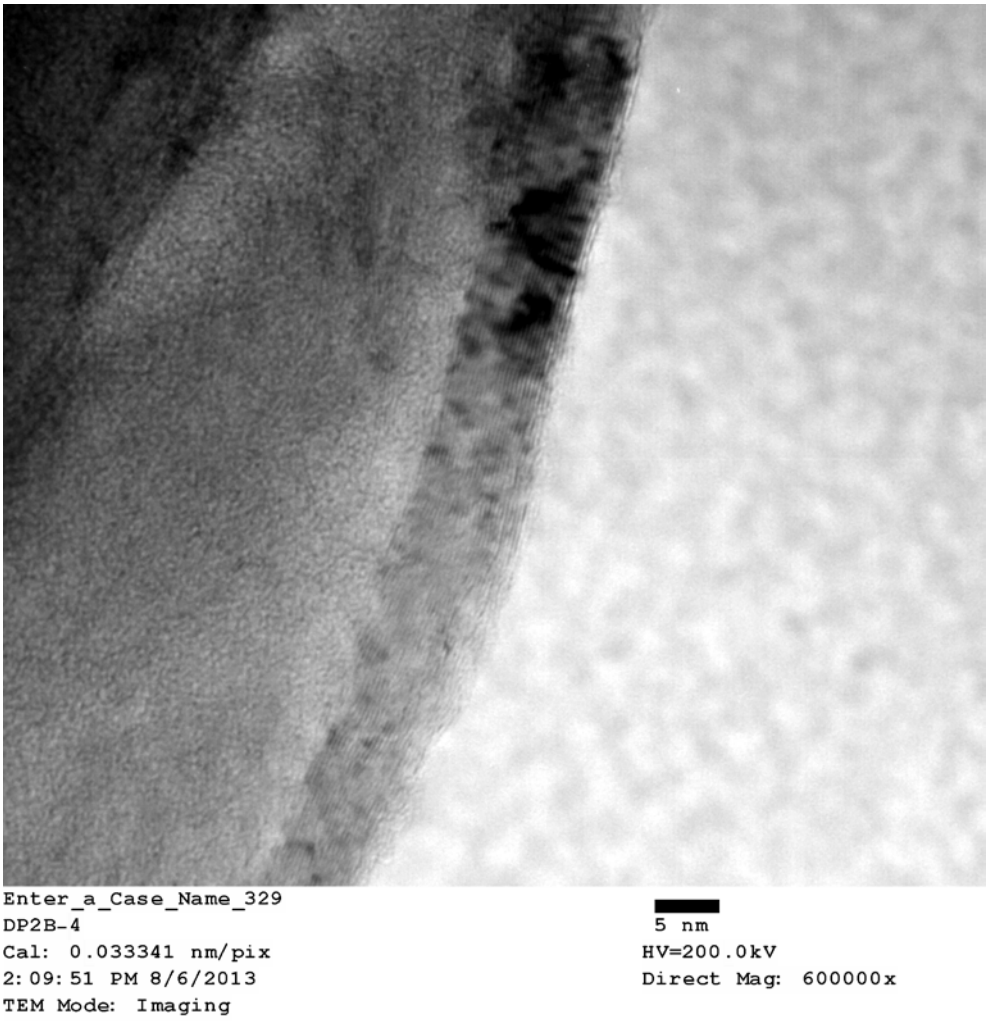

Figure 4. 10: TEM image of 1 hour steel milled sample

Using the formula shown in Equation 4.1, the grain sizes were calculated and represented in Table 4.3. Further analysis was performed on the recorded grain size of the

powders as their individual grain size is plotted against their milling time for each milling media. This was performed to determine the milling medium that propagates an increase in particle size as the milling time increases. From Figure 4.11, we can clearly see that the samples milled with steel vial demonstrates an increase in particle size as the milling time increases. Table 4.3 shows the calculated particle size of the milled samples with their individual milling times. Figure 4.11 shows the graph of particle size of the milled powder samples against milling time for their individual milling media.

Table 4. 3: Particle size determination

Milling Vial	Milling Hours (Hrs)	Particle Size (nm)
Steel	1	33
Steel	2	26
Steel	4	27
Steel	10	33
Tungsten Carbide	1.5	25
Tungsten Carbide	3	58
Tungsten Carbide	4.5	35
Zirconia	1	88
Zirconia	2	84
Zirconia	3	40
Zirconia	4	24

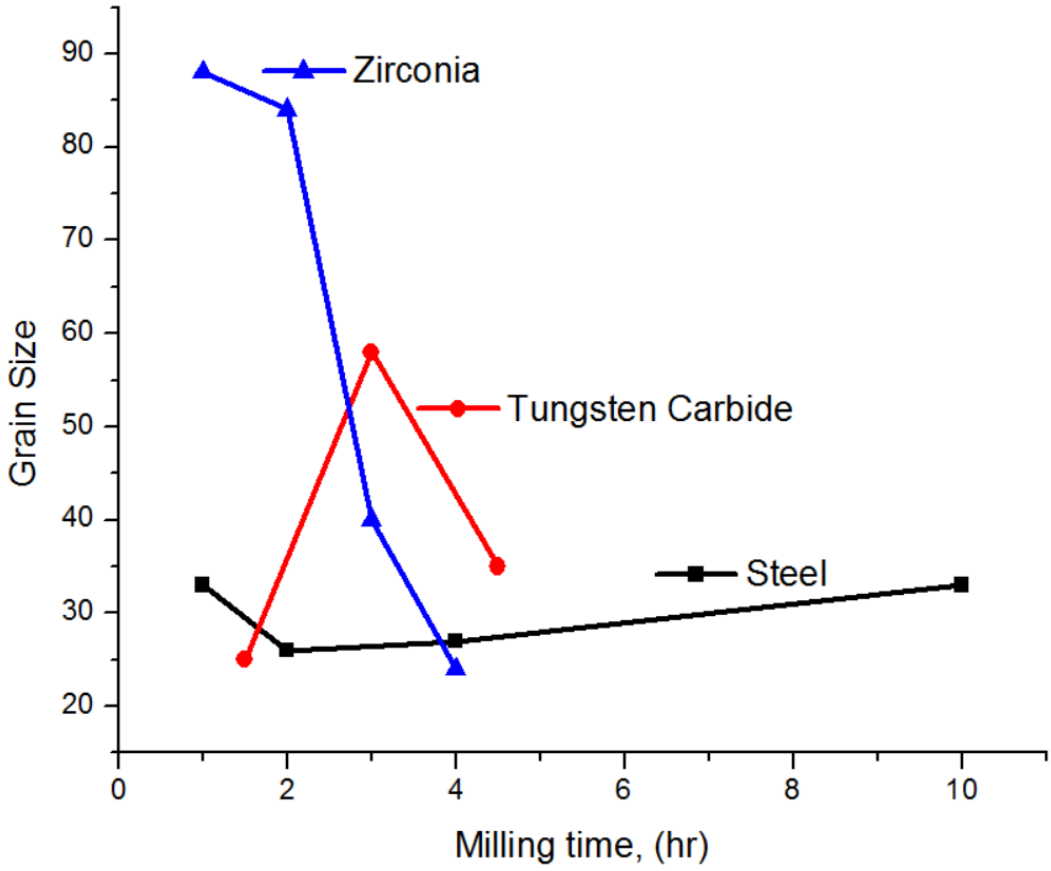

Figure 4. 11: Graph of particle size vs milling time for all milling media

4.4 Longer milling times contamination and diamond search

The milled samples are characterized using Raman spectroscopy and X-ray diffraction to determine the carbon state of the samples and possible contaminations due to longer milling times. The results are illustrated in the subsequent subsections with full description of the analysis performed on the samples.

4.4.1 Raman measurements

After analyzing the milled samples based on longer milling times, it was noticed that from 20+ hours of milling with steel vial, the sample becomes so contaminated that it starts

developing peaks which is suggested to be an oxide (especially FeO) (Barber, 2013). These results are shown in Figure 4. 12

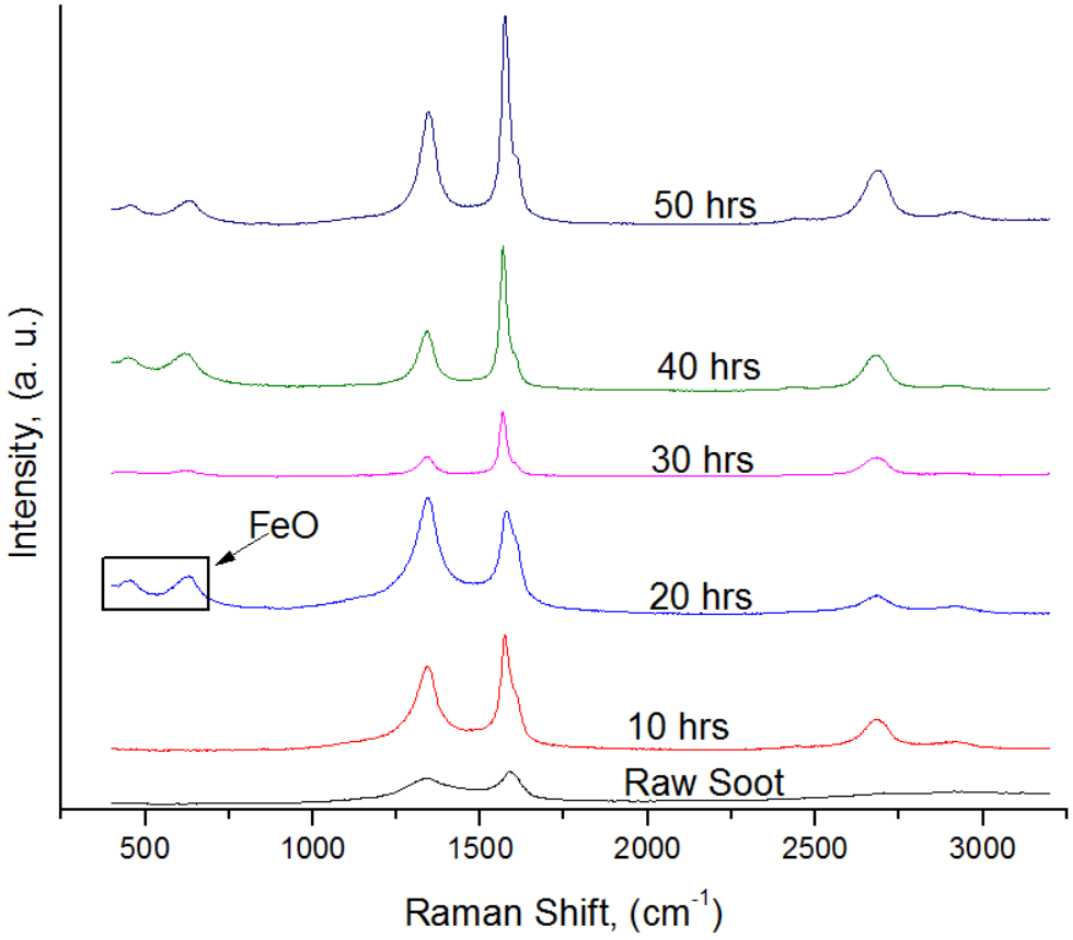

Figure 4. 12: Raman spectra of longer milling times with steel vial

Same irregularities was observed using tungsten carbide. As of milling time of 6+ hours, the D band increases significantly as the 2D band diminishes till it becomes no more. These results are shown in Figure 4.13.

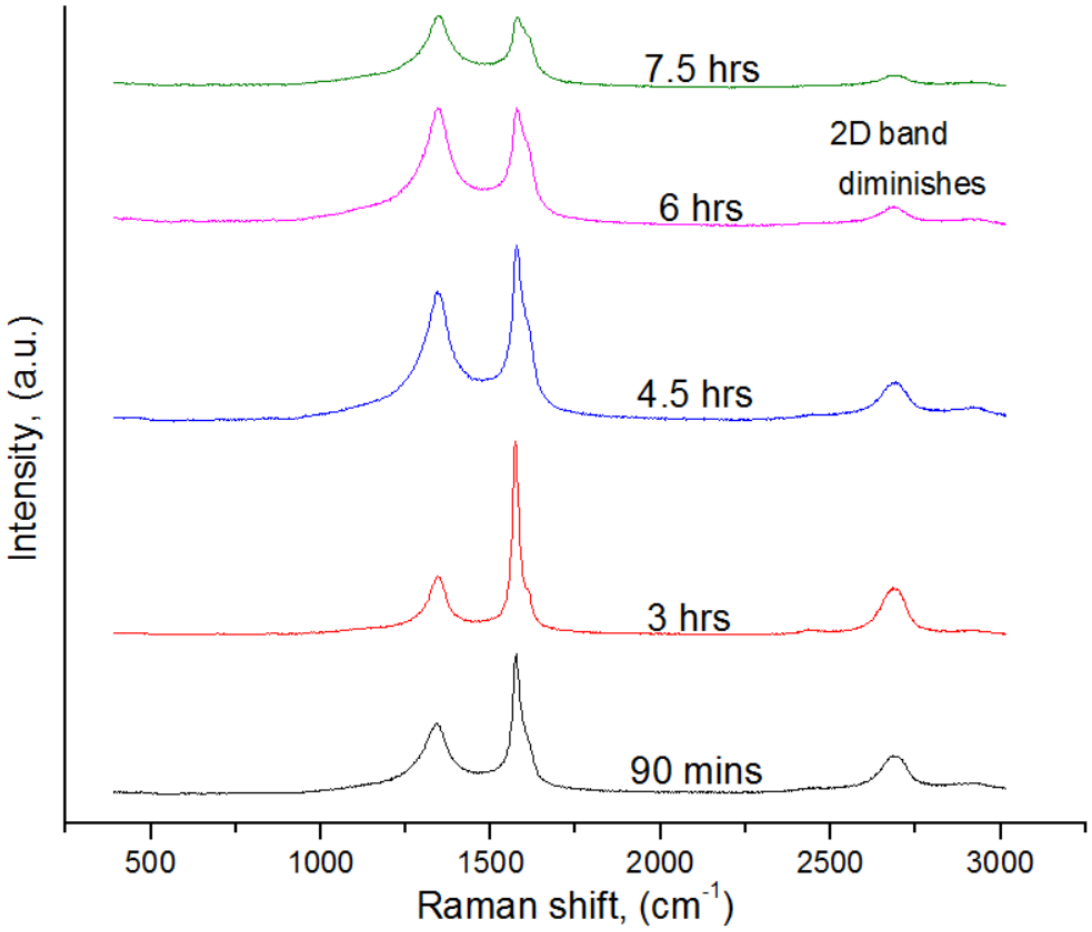

Figure 4. 13: Raman spectra of longer milling times with tungsten carbide vial

As a result, those samples of longer milling times (more than 4.5 hours) with tungsten carbide vial were left out since we require samples with less contamination and more carbon nanostructural particles. In the case of steel vial, it was quite different. As the milling times increases in steel, there appear peaks that is suggested to be diamond peak. This is possible due to the tendency of longer milling times to increase welding (Suryanarayana, 2001) and the synthesized graphene, graphitic carbon start transforming into diamond particles consequently. We observed an increased intensity of the G band compared to the D band within the Raman spectra of the samples with less than 10 hours of

milling times as shown in Figure 4.5, 4.6, 4.7, 4.12 and 4.13. This is caused by grain growth as a result of cold welding (Fals et al., 2013). Subsequent increased milling times above 10 hours causes an increased intensity of D band which is attributed to fracturing that leads to the grain size potentially decrease.

Further analysis were performed on the sample with longer milling time (10 hours) with steel vial by observing the sample under the TEM. The TEM image shows that the quasi-amorphous milled carbon particles has ingrained diamond nanostructured crystal. Figure 4.14 shows the TEM image of the sample milled with steel vial for 10 hours with insets showing a magnified image of the well-defined crystalline structures.

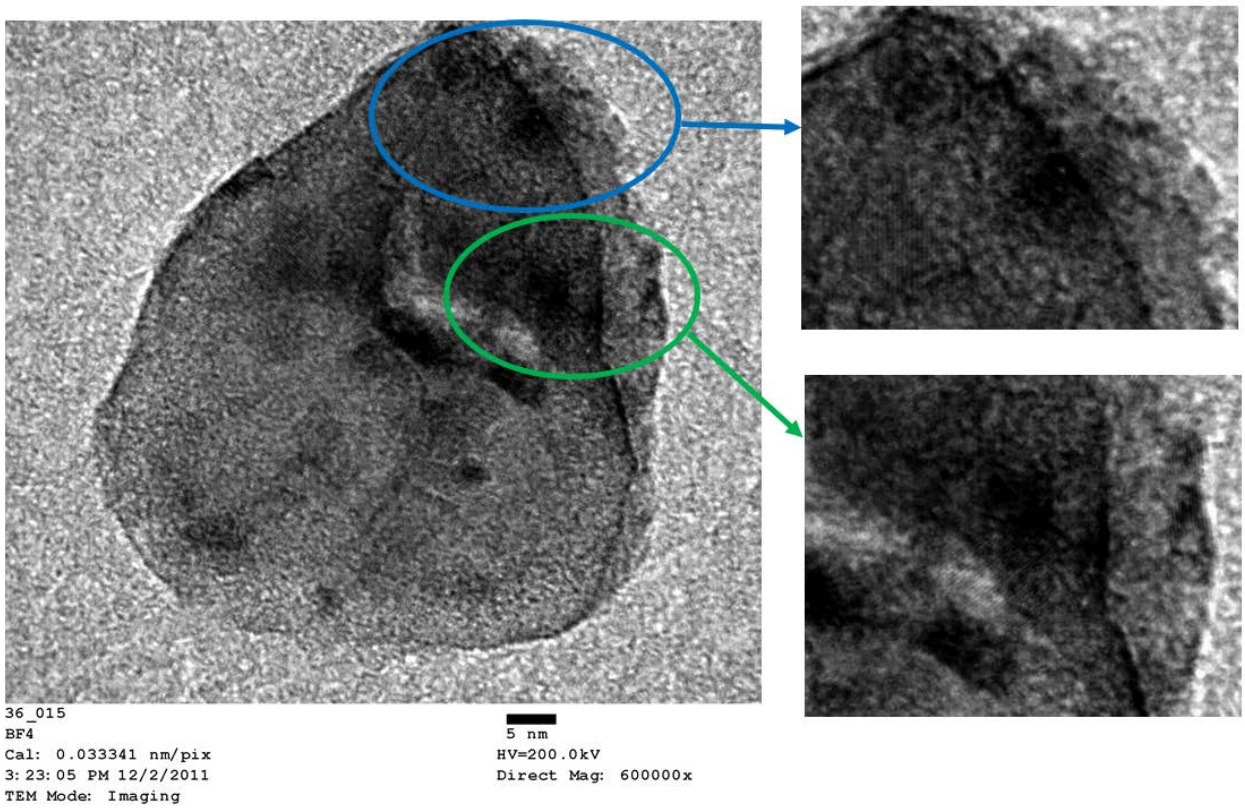

Figure 4. 14: TEM image of sample milled with steel for 10 hours

Further analysis on the Raman measurement shows that after milling the sample for 10 hours there was a shift of the D band which was at 1338 cm^{-1} for the raw material but now appears at 1334 cm^{-1} as shown in Figure 4.15. This shift of the D band as function of increased milling times suggests the synthesis of diamond which usually has its peak at 1334cm^{-1}(Setasuwon and Metanawin, 2009, Ferrari and Robertson, 2004). Though there could be some particles that has peaks at similar locations like Fe_2O_3 (Kim and Tannenbaum, 2011). However, similar peaks are present in the samples milled with tungsten carbide and zirconia with no iron contamination. The position of the peaks for the milled samples is represented in Table 4.4 to demonstrate the above stated shift. The sample represented as S1 being the sample milled for 1 hour in a steel vial (same for the others) and WC1.5 representing the sample milled for 1.5 hours in a tungsten carbide vial. Figure 4.15 shows the D band analysis of the sample that was milled for 10 hours using a steel vial. Table 4.4 shows the point at which the Raman peaks exist in the milled samples as gotten from the Raman spectra.

Table 4. 4: Peak positions from raman measurements

Sample Name	Milling Time (hrs)	D Band (cm^{-1})	G Band (cm^{-1})	2D Band (cm^{-1})
S1	1	1334.5	1574.1	2688.9
S2	2	1334.8	1567.8	2684.9
S4	4	1332.4	1567.2	2677.6
S10	10	1334.8	1571.5	2688.2
WC1.5	1.5	1334.3	1569.1	2688.3
WC3	3	1335.3	1567.2	2684.1
WC4.5	4.5	1335.9	1570.7	2686.1

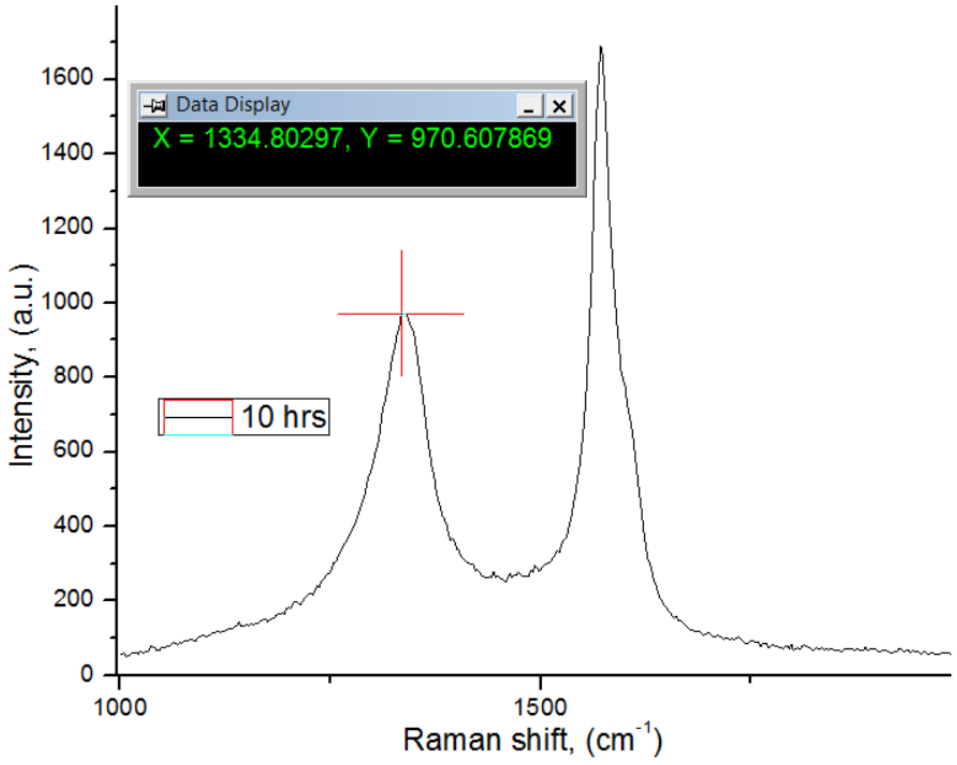

Figure 4. 15: D band analysis of 10 hours steel milled sample

The family of samples milled with steel vial shows better synthesis of diamond nanostructures. The samples milled for 1, 2 and 10 hours with steel and 1.5 hours with tungsten carbide show a well-defined D band peak at 1334 cm^{-1} demonstrating the clear presence of diamond nanostructures. It is very necessary to observe that these synthesis were achieved at a low milling time as 1 hour and was still maintained after 10 hours of milling with a relatively low intensity on the D band. This synthesis was attained with no inclusion of transition metal to propel the synthesis due to their catalytic nature. Observing the synthesis attained from the samples milled with tungsten carbide, we noticed the development of the D band at 1334 cm^{-1} which started to deviate further away as the milling time increases and at 6 hours of milling, the D band is 1345 cm^{-1}. This may be attributed to

the tungsten carbide additions due to excessive wear to the milling media and potential *in-situ* reactions.

Finally, many samples as selected from the milling groups and listed in Table 4.4 above have demonstrated a common well-defined D band peak synthesizing around 1334 cm^{-1}, G band peak around 1570 cm^{-1} and the 2D band dominating the 2D spectra at around 2680 cm^{-1}. These peaks and their positions are used to have a detailed information of the overall crystalline characteristics of the identified species such as graphite, graphene, graphitic carbon and diamond.

4.4.2 XRD analysis

The milled samples were characterized with the XRD and the results represented in spectra arranged according to their milling media. Observing the spectra from each milling family, we can see that they are similar with their peak position as milling times increases except for the reduction in intensity and width of the peaks. All the samples possess peaks at $2\theta = \sim26, \sim43, \sim54$ which all represents carbon peaks of different state and planes which will be discussed later in this study. We noticed that at lower milling times, the peaks are well defined, narrow of high intensity but as the milling times increases, we identify more noise, wider and less intense peaks at approximately same position which illustrates a particle size reduction.

Figure 4.16 shows the XRD pattern of the group of samples milled with steel followed by Figure 4.17 showing the XRD pattern of the group milled with tungsten carbide. The pattern shows three synthesized diamond peaks as a result of milling. These peaks represented at (1 1 1), (2 0 0), (2 2 0) diffraction of diamond is a definition of synthesized

diamond that possesses cubic orientation. Diamond nanostructures can be synthesized using different raw materials of different carbon state and methods. For example, the synthesis of nanoscale diamond texture possessing both cubic and hexagonal diamond crystal structure by applying planar impact on a grey cast iron sample (Chen et al., 2004). The high intense of the background in the XRD pattern illustrates the presence of some amorphous carbon. The peak at 2θ = ~26 for the XRD pattern represents the (0 0 2) lattice planes of graphite which explains the presence of layers of graphite as shown in the TEM image above. We observed another peak at 2θ = ~83 represents the (2 1 1) lattice planes of α-Fe which is attributed to the iron contamination from the steel milling vial as we cannot observe the same peak at the XRD pattern of the sample that was milled with tungsten carbide.

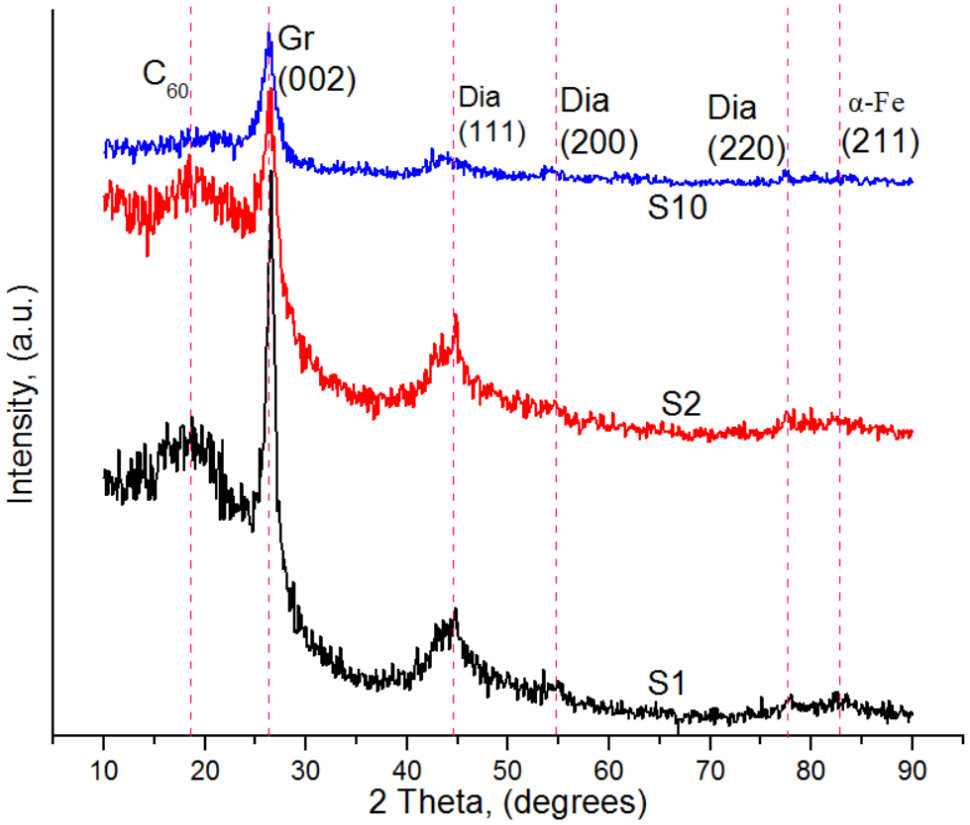

Figure 4. 16: XRD spectra of samples milled with steel identifying the carbon state and planes

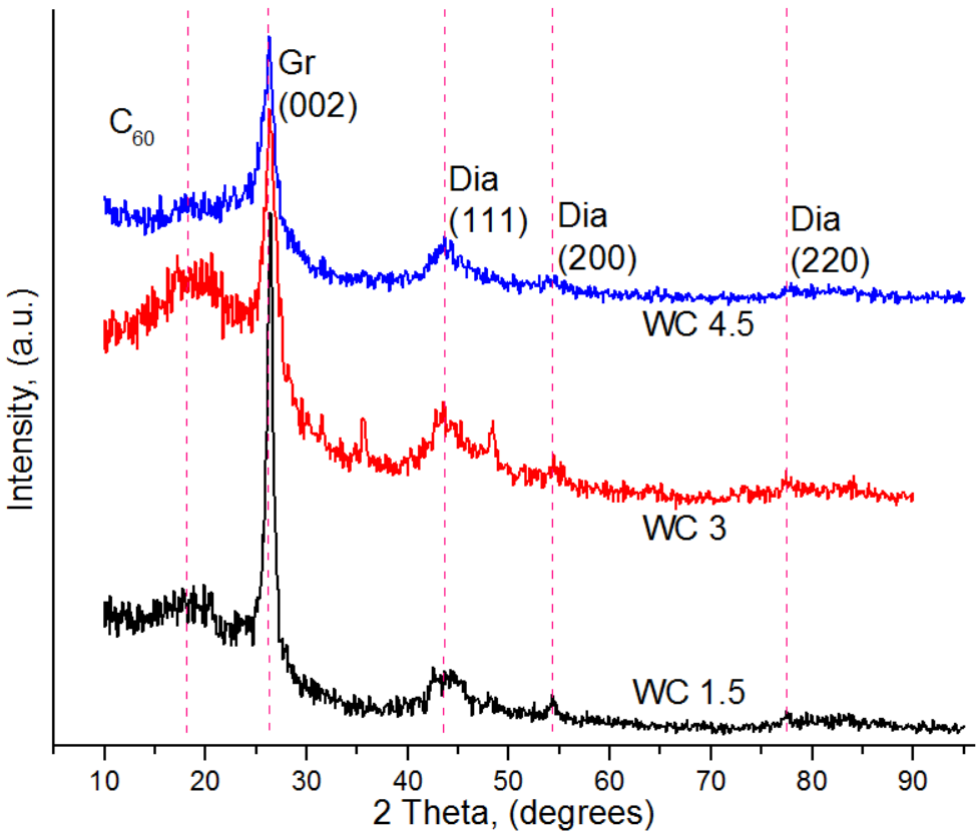

Figure 4. 17: XRD spectra of samples milled with tungsten carbide identifying the carbon state and planes

The samples milled with steel demonstrated the best synthesis of graphene, graphitic carbon and nanodiamond especially the sample milled for 1 hour. The samples milled with steel shows a D band peak at 1334.5 cm^{-1} after 1 hour of milling and synthesize at 1334.8 cm^{-1} after 10 hours of milling. This synthesis was achieved without the additions of transition metals. Though the samples milled for 1 hour and 10 hours possess their D band at approximately the same position but the sample milled for 1 hour ranks better than the latter due to its lesser milling time. Actually, all the samples milled with the steel vial bears similar contour as their D band position is at ~1334 cm^{-1}, the G band appears at ~1574 cm^{-1} and their 2D band has a peak position at ~2688 cm^{-1}. These peak positions are necessary

due to its demonstration of the presence of diamond, graphene and graphitic carbon structures. These nanostructures makes it possible for the samples to be used for reinforcement.

4.5 Sintered samples

Samples are sintered and named to be represented as S1-300C-1min or WC1.5-300C-1min as the first letter represent the milling medium, steel and tungsten carbide respectively followed by the number of hours milled. The second part of the name represents the sintering temperature and the last part represents sintering time.

4.5.1 Raman measurements

Raman measurements were performed on these samples and their spectra are demonstrated below according to their milling vial and sintering temperature. Figure 4.18 shows the Raman spectra of the steel milled samples of different milling times sintered at 300^0C. The samples were sintered at low temperature of 300^0C but the same sintering time to that of 2000^0C to understand the effects of sintering temperature on the sample. First, it is important to state the sample was able to consolidate at as low as 300^0C. Comparing the Raman measurement from the samples sintered at 300^0C and 2000^0C, we observed that there is no changes in the width of the spectra except for minimal shift in their peak position which is presented in Table 4.4 above.

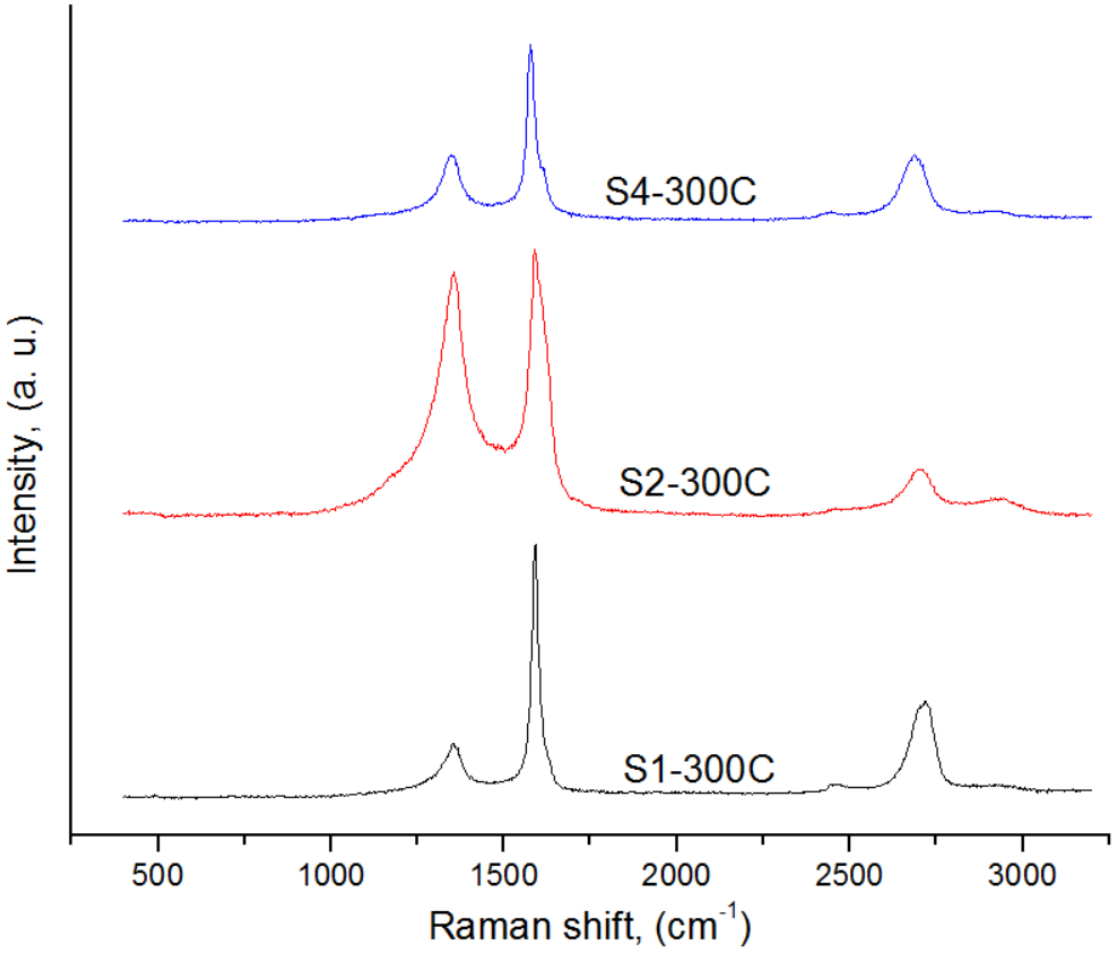

Figure 4. 18: Raman spectra of steel milled sample sintered at 300C

Figure 4.19 shows the Raman spectra of the steel milled samples with different milling times sintered at 2000^0C. The samples sintered at 2000^0C still possess all the peaks present in the as milled samples but more defined with improved intensities. We observed that the sintering at high temperature did not trigger any chemical reaction or phase change which can be proved by the inexistence of any peak that was not present at the Raman spectra from the as milled samples.

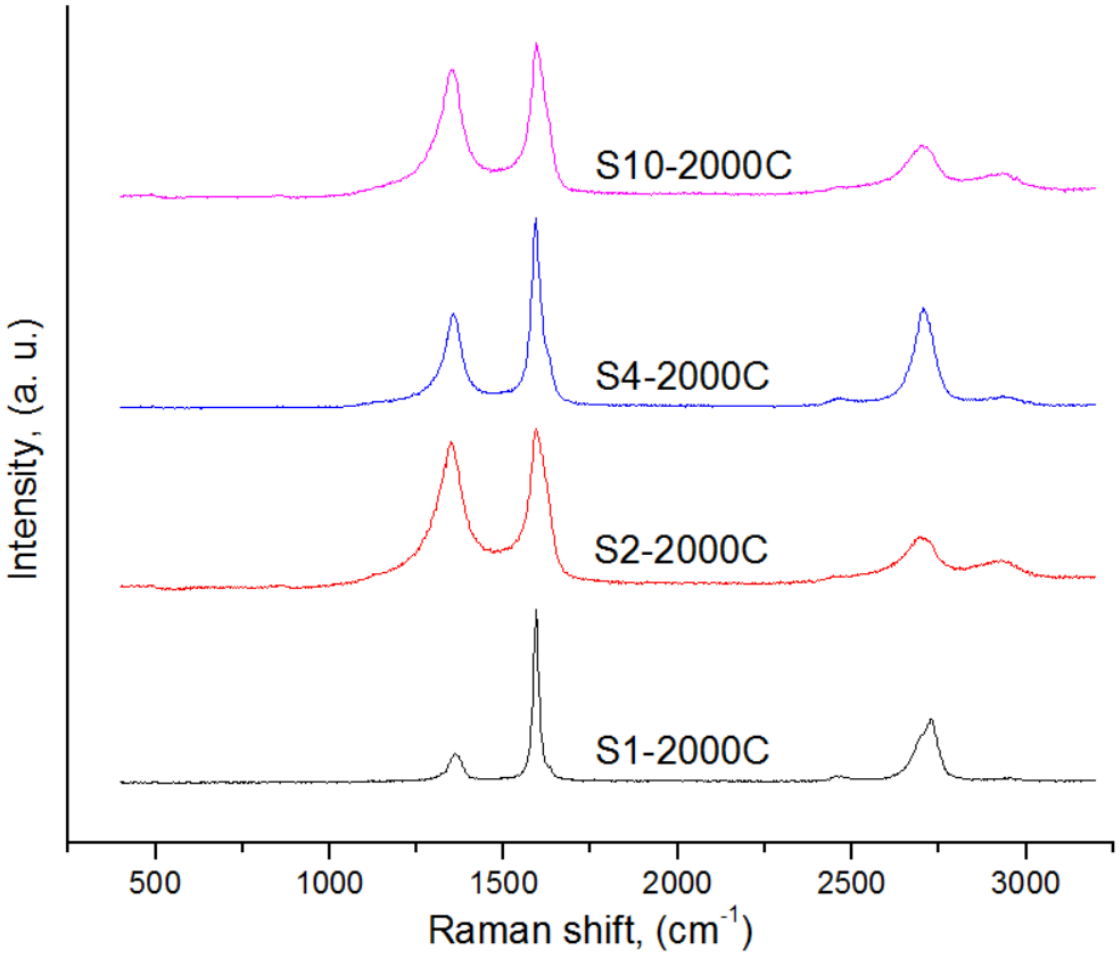

Figure 4. 19: Raman spectra of steel milled sample sintered at 2000C

Figure 4.20 show the Raman spectra of the samples milled with steel for 10 hours and sintered at the same temperature but different sintering times. This was done to understand the effect of milling time on the sample. Observing the spectra closely, we noticed that as the milling times increases, the peaks becomes narrower and well defined. This entails an improvement in the mechanical properties of the sample. Though the peaks becomes more defined, the peak positions still remains the same indicating no changes in the nanostructural constituents of the material.

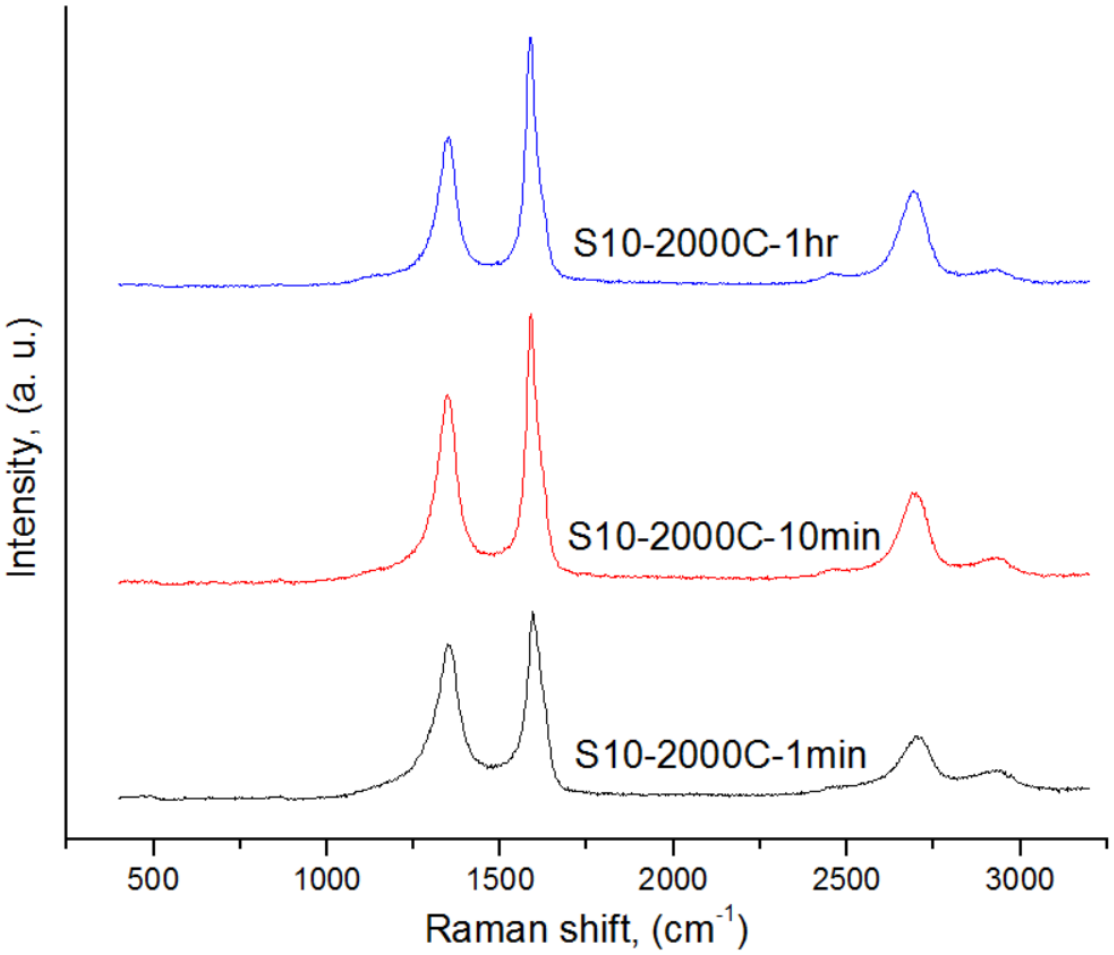

Figure 4. 20: Raman spectra of 10 hours steel milled sample sintered at 2000C

Figure 4.21 shows the Raman spectra of the tungsten carbide milled samples of different milling times sintered at 300^0C. Just like we mentioned with the samples milled with steel, these samples came out well consolidated after sintering with low temperature and still retained the same width of the peaks present but minimal shift with the peak position. We also observed the high intensity of the D band which can be attributed by the defects caused by the milling media. We can also say that the peaks are well defined with

none of them hidden within the background which shows good presence of the nanostructural particles.

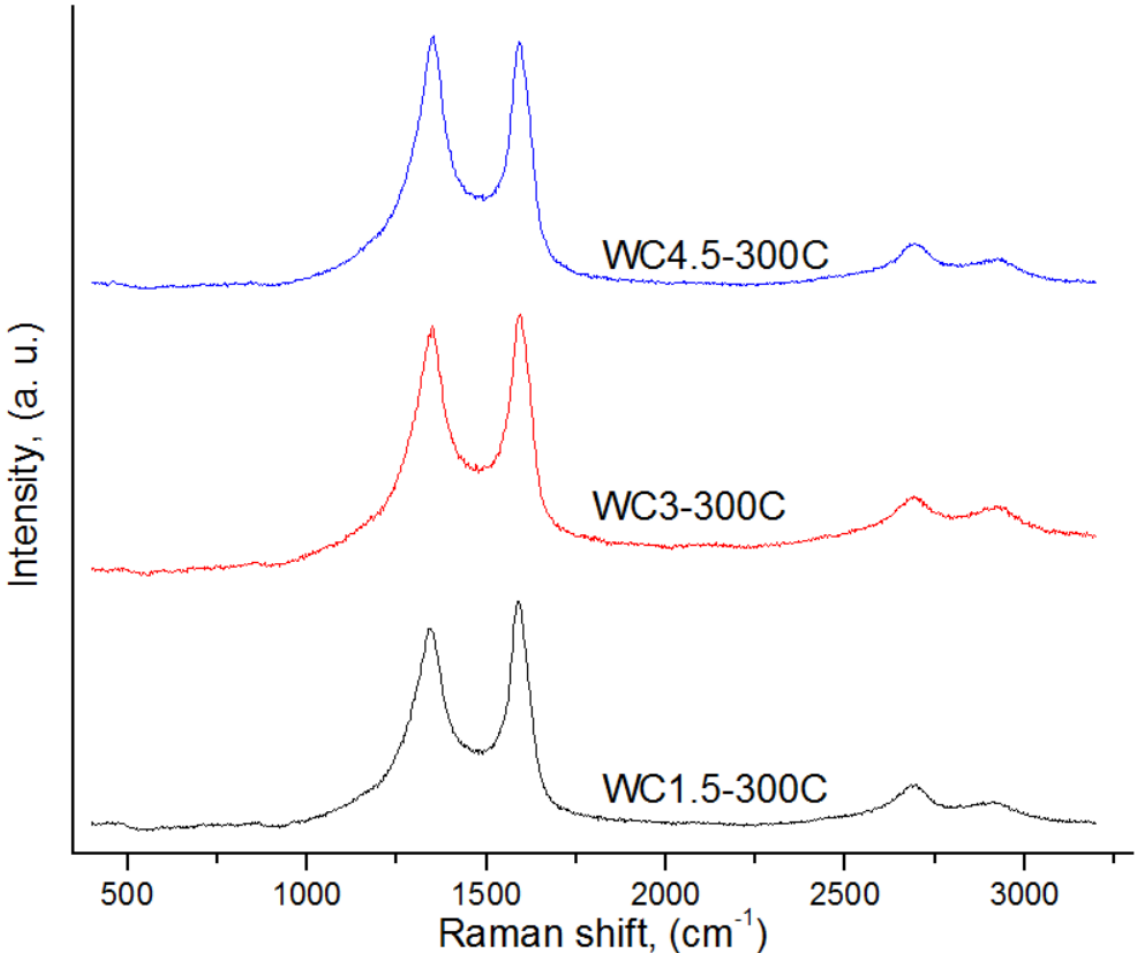

Figure 4. 21: Raman spectra of tungsten carbide milled sample sintered at 300C

Figure 4.22 shows the Raman spectra of the tungsten carbide milled samples with different milling times and sintered at 2000^0C. Comparing the Raman measurement from these samples with the samples that were sintered at 300^0C, we cannot see much of a different as to the width and position of the peaks for the D and G band. The 2D band rather has higher intensities and are narrower yet there is no development of new peaks showing

that the nanostructural constituents remains the same. The D band still retained its high intensities as compared to the spectra of samples sintered at 300^0C

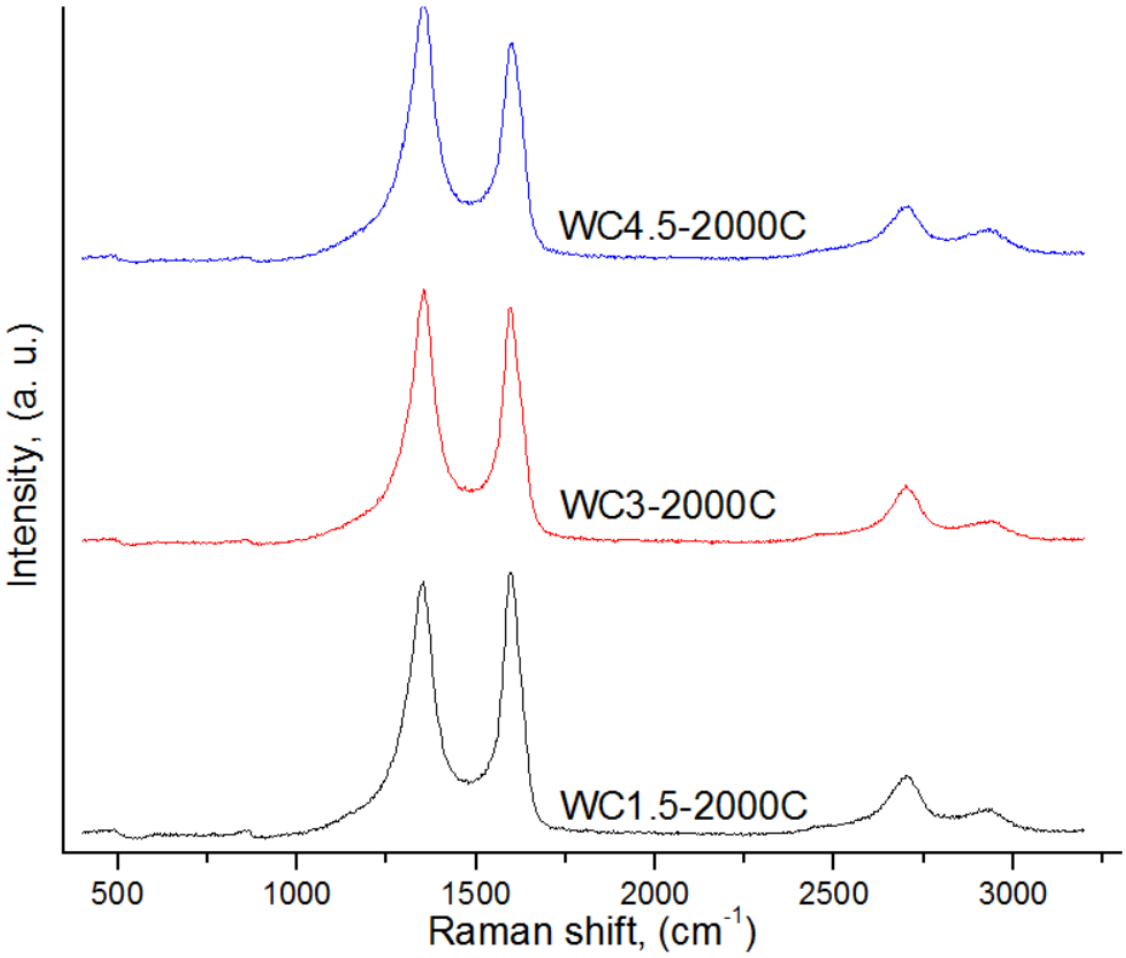

Figure 4. 22: Raman spectra of tungsten carbide milled sample sintered at 2000C

The sintered group of samples still shows the same D, G and 2D band peaks that synthesized during milling. These peaks were improved as a result of sintering. Comparing the Raman spectra of the sample milled with steel before and after sintering for 1, 4 and 10 hours, we observed an increased and well defined 2D band peak in the sintered sample as the D band reduces which is a clear indication of the presence of graphene in the sintered

samples while the samples that were milled with tungsten carbide show a well-defined D and G band peak with their 2D band peak reducing in intensity as they become wider in spectrum after sintering.

We observed that sintering at a low temperature of 300^0C gave almost similar Raman results as that of the samples sintered with high temperature of 2000^0C using our innovative pressureless induction heating sintering. This is so obvious that our innovative sintering process is able to consolidate our sample at a low temperature and still preserve the properties of the sample as when they are sintered at 2000^0C

More studies were conducted on the sample that was milled for 10 hours using a steel vial as the sample was sintered at a temperature of 2000^0C for 1 minute, 10 minutes and 1 hour. The Raman measurement from the sample is compared to analyze the synthesis on the D, G and 2D band. Figure 4.23 shows the Raman measurements for the sample milled for 10 hours in a steel vial and sintered at different times.

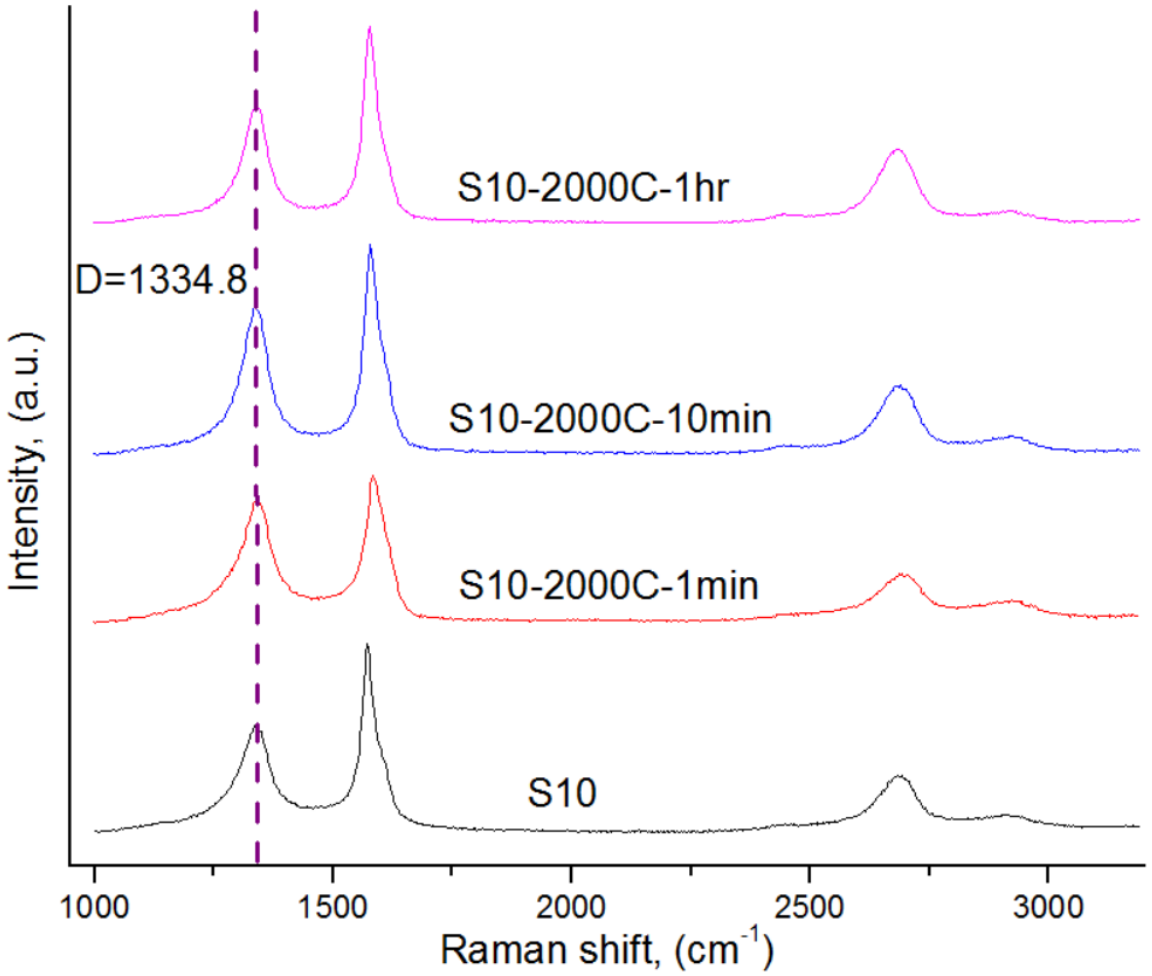

Figure 4. 23: Raman 10 hours steel milled sample and sintered samples at different times

Observing the Raman spectra of this samples, we could see that they still retain the peak positions for the D, G and 2D band of their spectrum. This is a clear indication of consolidating the powdered sample without disorienting the crystal structures of the sample. Furthermore, we still have our D band at 1334.8 for the sample milled for 2, 4 and 10 hours with steel and sintered which strongly illustrates the presence of diamond nanoparticles and will further be analyzed using the XRD results to proof the presence of the diamond. Observing the Raman shift in the sintered samples as listed in Table 4.5, we can say that

there wasn't really a significant shift in the peak positions of the sintered samples as compared to those of the as milled sample. Table 4.5 shows the peak position of the D band as compared between the as milled samples and the sintered samples

Table 4. 5: Peak position for the milled and sintered samples

Sample Name	D Band, as milled (cm^{-1})	D Band, as sintered (cm^{-1})
S1-300C-1min	1334.5	1340.6
S1-2000C-1min	1334.5	1345.8
S2-300C-1min	1334.8	1340.6
S2-2000C-1min	1334.8	1334.7
S4-300C-1min	1332.4	1335.4
S4-2000C-1min	1332.4	1340.6
S10-2000C-1min	1334.8	1334.8
S10-2000C-10min	1334.8	1334.2
S10-2000C-1hr	1334.8	1334.8
WC1.5-300C-1min	1334.3	1338.6
WC1.5-2000C-1hr	1334.3	1335.4
WC3-300C-1min	1335.3	1338.6
WC-2000C-1min	1335.3	1340.6
WC4.5-300C-1min	1335.9	1338.6
WC4.5-2000C-1min	1335.9	1340.6

Generally, the most common method to determine the quality of carbon nanostructures in a carbon sample is calculating the peak intensity ratio of the D and 2D band (Robles Hernandez et al., 2014). Analysis to determine the sample with the best quality of carbon nanostructures was performed using the peak intensity ratio of the D band and 2D band and was compared to the as milled intensity ratio to determine if there is any significant difference. Table 4.6 shows the intensity ratio of the milled samples and sintered samples.

Table 4. 6: Intensity ratio of the milled samples and sintered samples

Sample Name	D, 2D band intensity ratio for as milled	D, 2D Band intensity ratio for as sintered
S1-300C-1min	1.92	0.58
S1-2000C-1min	1.92	0.46
S2-300C-1min	2.82	4.03
S2-2000C-1min	2.82	2.54
S4-300C-1min	2.34	0.99
S4-2000C-1min	2.34	0.94
S10-2000C-1min	1.83	2.32
S10-2000C-10min	1.83	1.98
S10-2000C-1hr	1.83	1.53
WC1.5-300C-1min	1.71	3.25
WC1.5-2000C-1hr	1.71	3.75
WC3-300C-1min	1.21	2.45
WC-2000C-1min	1.21	3.96
WC4.5-300C-1min	3.00	3.94
WC4.5-2000C-1min	3.00	4.24

Analyzing the comparison of the peak intensity ratio, we observed that there was significant increase in the intensity ratio of some samples indicating an increased defect on the sample especially for the samples that were milled with tungsten carbide while the samples milled with steel for 1, 4 and 10 hours witnessed a decrease in the intensity ratio which suggests an improvement in the graphene particles of the samples. This is very necessary as we can illustrate the improvement of the samples achieved through the solid state consolidation of the samples using our innovative Pressureless induction heating sintering.

Over the years, studies have developed methods for quantifying the disorder using Raman measurement for nano-graphite (Cancado et al., 2006, Ferrari and Robertson, 2000, Pimenta et al., 2007, Tuinstra and Koenig, 1970) and graphene (Jorio et al., 2010a, Lucchese et al., 2010, Martins Ferreira et al., 2010, Teweldebrhan and Balandin, 2009). In this study, we used the most advanced method that was developed for the edge –defects in nano-

graphitic particles in which the in-plane crystallite size ranges from La = 20nm (Jorio et al., 2010b) to La = 40nm (Fals et al., 2012b). To obtain the crystallite size of the sintered samples, we use the expression in Equation 4.1 above.

This equation provides good opportunity to analyze the nano-graphitic crystallite size of our sample as it relates to the type of disorder present at the graphene edges. The results are represented in the Table 4.7 as it is compared with the results gotten from the as milled samples. Table 4.7 illustrates that there were differences in the crystallite size of some of the samples especially the ones milled with the tungsten carbide and one hour milling with steel as the rest encountered slight changes to the crystallite size. It is important to say that the grain size is not a function of the sintering temperature as we observed the same samples sintered at high and low temperature to be relatively the same grain size. This is necessary as we can be able to consolidate our samples at solid state using our innovative sintering method without significantly altering the microstructural topography of our sample at different temperatures. Table 4.7 shows the results of the crystallite size of the sintered samples in comparison with the as milled samples.

Table 4. 7: Crystallite size results

Sample Name	Crystallite size for as milled samples (nm)	Crystallite size for as sintered samples (nm)
S1-300C-1min	23	56
S1-2000C-1min	23	73
S2-300C-1min	17	13
S2-2000C-1min	17	13
S4-300C-1min	18	33
S4-2000C-1min	18	25
S10-2000C-1min	22	15
S10-2000C-10min	22	17
S10-2000C-1hr	22	21
WC1.5-300C-1min	17	14
WC1.5-2000C-1hr	17	13
WC3-300C-1min	39	12
WC-2000C-1min	39	11
WC4.5-300C-1min	24	12
WC4.5-2000C-1min	24	10

4.5.2 XRD analysis

The sintered samples were characterized with the XRD and their spectra plotted according to their milling media, sintering temperature and sintering times. Observing the XRD pattern of the sintered samples, we still have the peaks at 2θ = ~26, ~43, ~53, ~77 and ~85 as we noticed from the XRD pattern of the as milled samples except that the peaks are more defined in the pattern of the sintered samples. We can also observe the reduction in the intensity of the peaks as the milling times increases which is a proof to what was stated earlier in this study about the samples tending to become more amorphous as the milling times increases. Comparing the sintered samples of different temperature, we noticed that there wasn't any significant changes between the samples sintered at low and high temperature. They all have well-defined peaks of diamond and graphite except for the steel milled samples which still bears the α-Fe peak at lattice plane of (2 1 1) at 2θ = ~85.

There is a significant change for the sample milled for 4 hours with steel vial and sintered at 300^0C. There is a peak at 2θ = ~36 which is attributed to Fe_3C peak at lattice plane (2 1 0). This same peak is observed at the same sample but sintered at 2000^0C. The peak is not clear as there is a lot noise at the background and it seemed to be embedded in the noise. Also, another peak exists at 2θ = ~55 attributed to diamond at lattice plane of (2 0 0) present in the sample milled with steel for 1 hour and sintered at both 300^0C and 2000^0C. This peak disappeared at the sample milled for 2 and 4 hours with steel medium and sintered at both 300^0C and 2000^0C but can be seen clearly with the XRD spectra of the 10 hours milled and sintered samples. This peak is so clear with all the samples milled with tungsten carbide. Figure 4.24 shows fully characterized XRD pattern of the samples milled with different media and sintered at different temperatures.

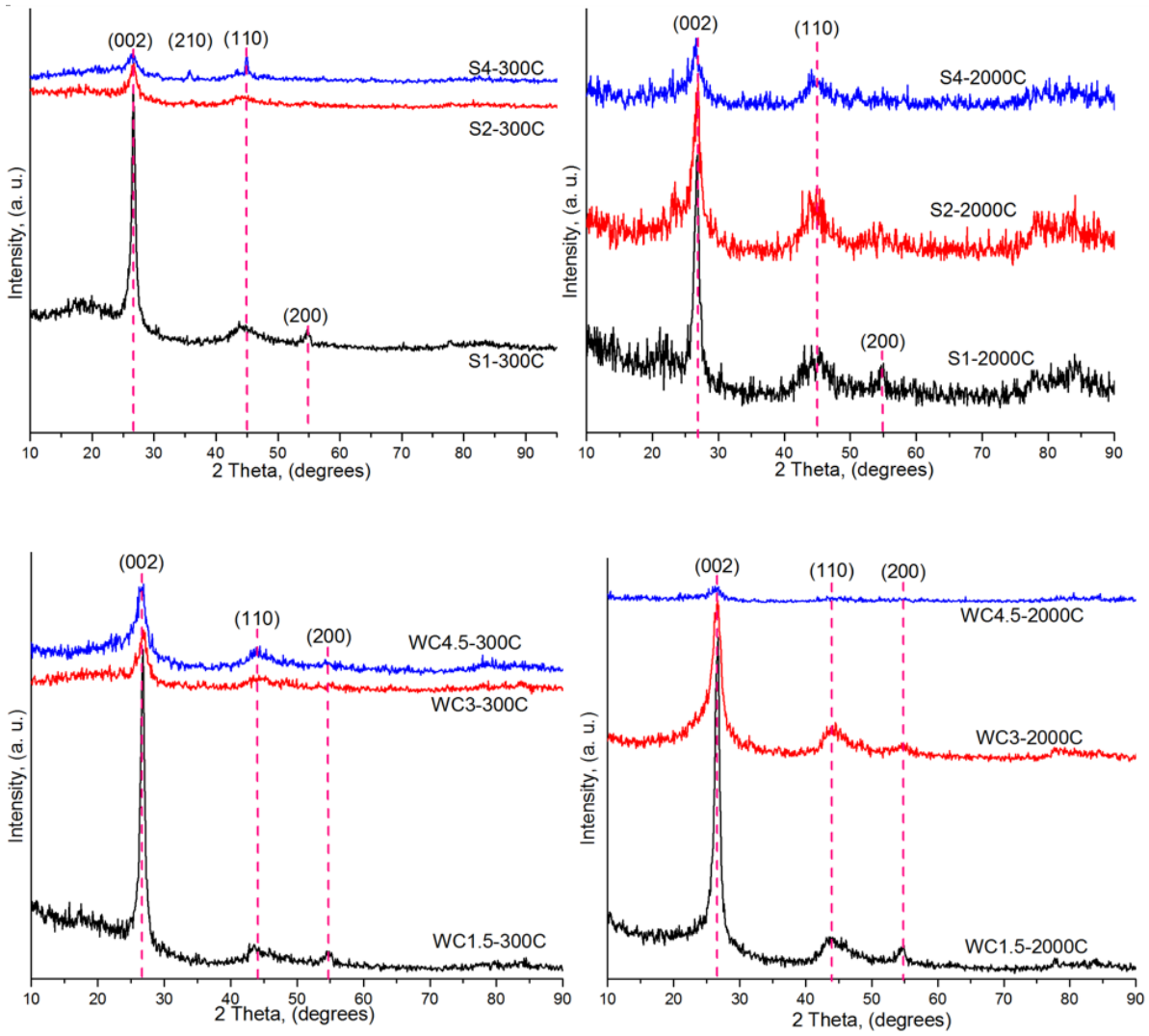

Figure 4. 24: XRD pattern of samples milled with different media and sintered at different temperatures

It is important to identify the only significant change in the sintered sample which is the splitting of the peak at 2θ = ~43 into ~43 and ~45 for the sample milled with steel for 10 hours. The peak splits into lattice planes of (1 1 1) and (1 1 0) representing diamond and α-Fe respectively (Wen et al., 2006). This is as result of the iron contamination from the milling vial into the sample thereby catalyzing the synthesis of many complex carbon nanostructures and over time resulting into the formation of α-Fe due to high milling times.

We also observed another clear peak of α-Fe in the 10 hours milled sample that was sintered for 1 hour at 2000^0C. This peak exists at 2θ = ~65 at a lattice plane of (2 0 0) of α-Fe. This peak also exists in the other samples milled for 10 hours and sintered for 1 and 10 minutes but they are mostly covered by the background. Figure 4.25 shows the XRD pattern of the samples, milled in steel for 10 hours and sintered at different times and a temperature of 2000^0C, indicating all the lattice planes present. These lattice planes represents different carbon states and are stated as so: diamond – (1 1 1), (2 0 0) and (2 2 0); graphite - (0 0 2); α-Fe – (1 1 0), (2 0 0) and (2 1 1).

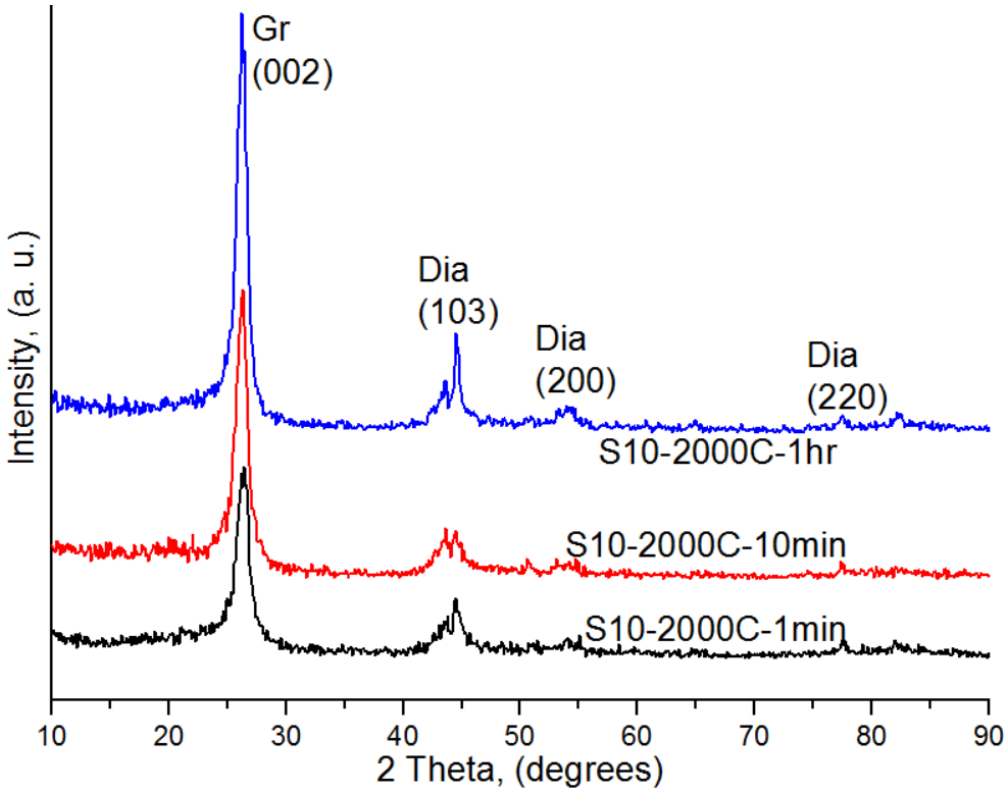

Figure 4. 25: XRD pattern of 10 hours milled samples sintered at different times showing lattice planes

Conclusively, the characterization of the samples using the XRD results illustrated the presence of the nanostructures identified. We were able to identify the planes at which

these nanostructures exist. The results of the XRD also concurred with what we showed with the SEM and TEM images. We were also able to prove that the Raman measurement was right showing the presence of the complex carbon structures. This results illustrates that the sintering both at high and low temperature did not cause any chemical changes within the material.

Finally, grain size of the sintered samples were determined as part of the analysis performed with the XRD spectra. This was done using the Scherer's equation as stated in Equation 3.1. It was done specifically for the graphite peak at $2\theta = \sim 26$. Where τ is the grain size, K is the shape factor which has a typical value of 0.9, λ is the wavelength of the X-ray which is 0.154 nm, β is the full width half maximum of the XRD peak and θ is the Bragg's angle. It is very important to state that this equation provides the lower bound of the particle size due to the different factors that contributes to the width of a diffraction peak. Table 4.8 shows the calculated particle size of the sintered samples.

Table 4. 8: Particle size of the sintered samples

Sample Name	Particle Size (nm)
S1-300C	27
S1-2000C	19
S2-300C	16
S2-2000C	16
S4-300C	28
S4-2000C	41
S10-2000C-1min	13
S10-2000C-10min	13
S10-2000C-1hr	12
WC1.5-300C	16
WC1.5-2000C	13
WC3-300C	18
WC3-2000C	14
WC4.5-300C	25
WC4.5-2000C	29

4.6 Discussions

This part provides a general discussion of the results obtained from this work. Commercially available fullerene soot was milled at different hours ranging from 1 hour to 50 hours using different milling vials like steel, tungsten carbide and zirconium. The synthesis of the nanostructural particles as a result of mechanical milling were discussed. The samples were characterized to obtain samples with better properties. The selected milled samples were sintered through our innovative pressureless sintering using induction heating. This study explores the effects of these processes towards the synthesis of carbon nanostructures and the consolidation of the sample to get better properties. It also demonstrates different successful applications of the samples.

The grain size of the samples were calculated using the Scherer's equation. Results gotten from XRD and Raman measurements were compared to ensure accuracy of information gotten from both techniques. This project explored the in-situ transformation of the fullerene soot without any inclusion of transition metal and the consolidation of the powder without any sintering additives. We concluded that the in-situ transformation occurring in the samples is as a result of a welding process that takes place during the milling activity. The milling process generates high energy that causes the atoms to deform which leads to the actual transformation.

The raw soot transforms in-situ after 1 hour into graphitic particles. This work demonstrates that after milling the raw soot for 10 hours in a steel vial, nano-diamond particles are synthesized. It tells that this is the best and cost effective method for the synthesis of nano-diamond particles while longer milling times with tungsten carbide generates a lot of contamination which is not required for the synthesis of the carbon

nanostructures. We also understand that milling with zirconium also generates great contamination even at shorter milling times.

More so, the introduction of our innovative pressureless sintering using induction heating is the most efficient, unconventional and cost effective method of consolidating our powder samples at solid state as it preserves the densification of the samples. This sintering method helps to propagate the synthesis of graphene and other complex carbon nanostructures. It is very necessary to note that sintering does create the synthesis rather it improves on it. Raman measurements were analyzed and the spectra show peaks identified at the position of fullerene, graphene and diamond. It is important to reiterate that though there are always issue with the position of peaks for Fe_2O_3 and diamond which has led to so many study on these carbon states. We identified diamond peaks in the spectra of samples milled with steel vial and tungsten vial with no Fe inclusions.

Chapter 5

5.1 Applications

In this chapter, we are going to present some successful studies whereby our samples were applied to where good results were obtained. This part explores the state of the art applications of the milled sample as it is used to reinforce structural materials and improve low-cost lithium ion batteries. The results of the improvements achieved are presented herein. It is important to state that this is the first time that structural material of this kind with complex nanostructures are applied towards reinforcement of epoxy, improvement of anodes for lithium ion batteries and producing a pure elastic condition for carbon-carbon composites

5.1.1 Epoxy matrix composites

This involves the reinforcement of epoxy polymer matrix with our milled samples for coating applications. The results obtained from this study include significant increase in tensile elongation of more than 13% in 1wt% additions of our sample thereby resulting in a change of the failure mechanism of the polymer when in tension from brittle to ductile (Okonkwo et al., 2014). We also obtained a reduced coefficient of friction from 0.91 as gotten from the plain epoxy to 0.15 in the 1wt% composite of our sample. Other properties of the polymer with great improvement include 43% and 94% increment in the elastic modulus and hardness respectively with a reduction of about 80% of the lateral forces during nanoscratch. Thermogravimetric analysis performed on this sample present our sample as being stable to the temperatures of ~350^0C with a 7wt% loss in weight and an accumulated

weight loss of 83wt% at 700^0C. This weight loss is as a result of the oxidation of the amorphous material and the short-order graphitic structures.

We obtained results from Raman which shows a similar spectra as the one obtained from the raw samples (as milled samples). Figure 5.1 shows the Raman spectra of the raw epoxy (E/0), carbon sample milled for 1 hour (S1), 1wt% inclusion of the milled sample to the epoxy (E/CS1/1) and 3wt% inclusion of the milled sample to the epoxy (E/CS1/3). We can clearly observe the synthesis of the D, G and 2D band as the milled sample is added to the raw epoxy. The 2D band is partially embedded to the background is as result of the amorphous nature of the carbon material when added to the epoxy and we can see an increase in intensity of the 2D band as the weight percentage increases. The Raman spectra of the composites still retains the peaks of the epoxy and bears little shift in the characteristics graphitic carbon bands which means that there was no possible alteration of the initial milled sample. Furthermore, no chemical interaction occurred between the epoxy and the milled samples except for their interactions through van der Waals forces

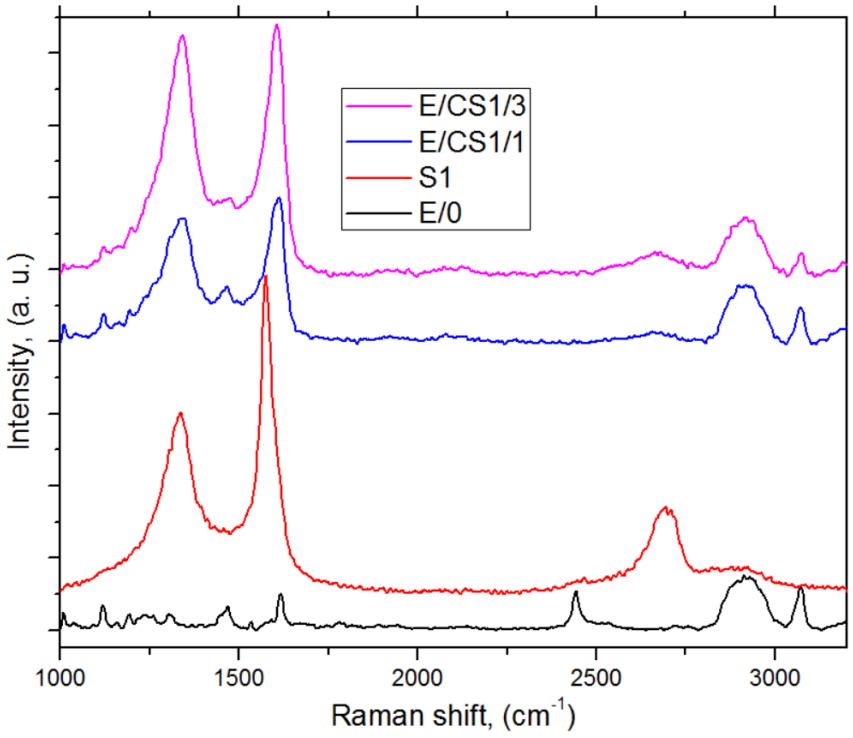

Figure 5. 1: Raman spectra of the composites, raw epoxy and milled samples

The D and G bands observed in the Raman spectra are mainly for the sp2 carbon samples (Robertson, 2002). The G band is attributed to the E_{2g} carbon vibrational mode allowed by Raman selection rules while the D band is as a result of the carbon vacancies, functional carbon-oxygen groups and boundaries of nano-sized graphite particles involved with defect-induced Raman scattering (Okonkwo et al., 2014).

SEM images were taken from the sample of the epoxy and the composites with 1 and 3 wt% soot. We observed a significant difference in the surface morphology. The epoxy shows an almost clear opaque picture except for the dirt of alumina gotten from the polishing of the sample while the composites with the milled samples inclusions shows the embedded spherical nanostructures in the polymeric matrix. The spherical soot particles creates a work-hardening effect in the epoxy composites by preventing the free crack grow. Figure

5.2 shows the SEM images of the epoxy and the composites with 1wt% and 3wt% of the milled samples.

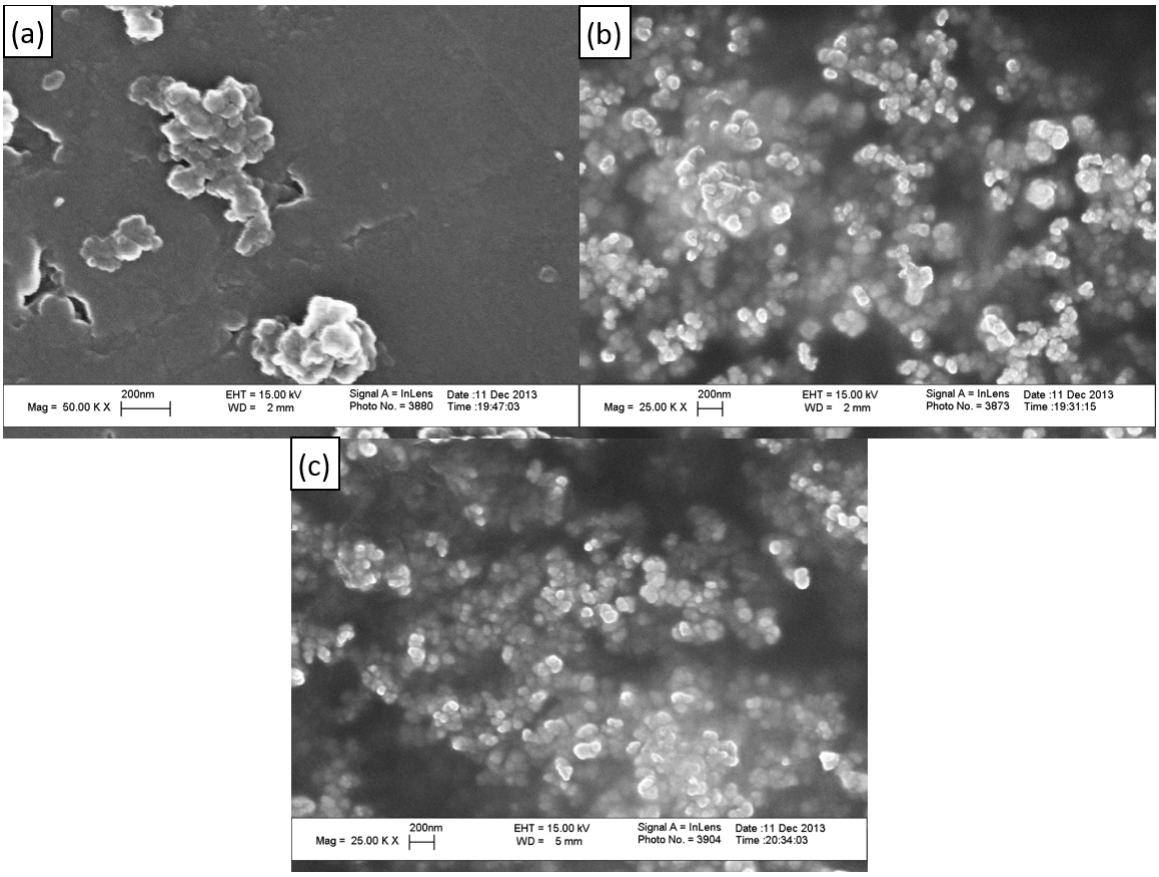

Figure 5. 2: SEM images of (a) epoxy and composites with (b) 1wt% milled sample (c) 3wt% milled sample (Okonkwo et al., 2014)

Conclusively, the milled samples were used to reinforce the epoxy matrix to obtain a high ductility with a recorded change in failure mechanism from brittle to ductile achieving an enormous elongation from 0.7% in the epoxy to above 13% in the composite with 1wt% of the milled sample. More enhancement of the properties of the epoxy achieved as a result of the reinforcement with the milled sample include strength, coefficient of friction (reduced by 83%), hardness (increased by 93.7%) and modulus of the composites

(increased by 49%). Figure 5.3 shows the stress-strain curve of the epoxy and the composites with 1 wt% and 3 wt% carbon.

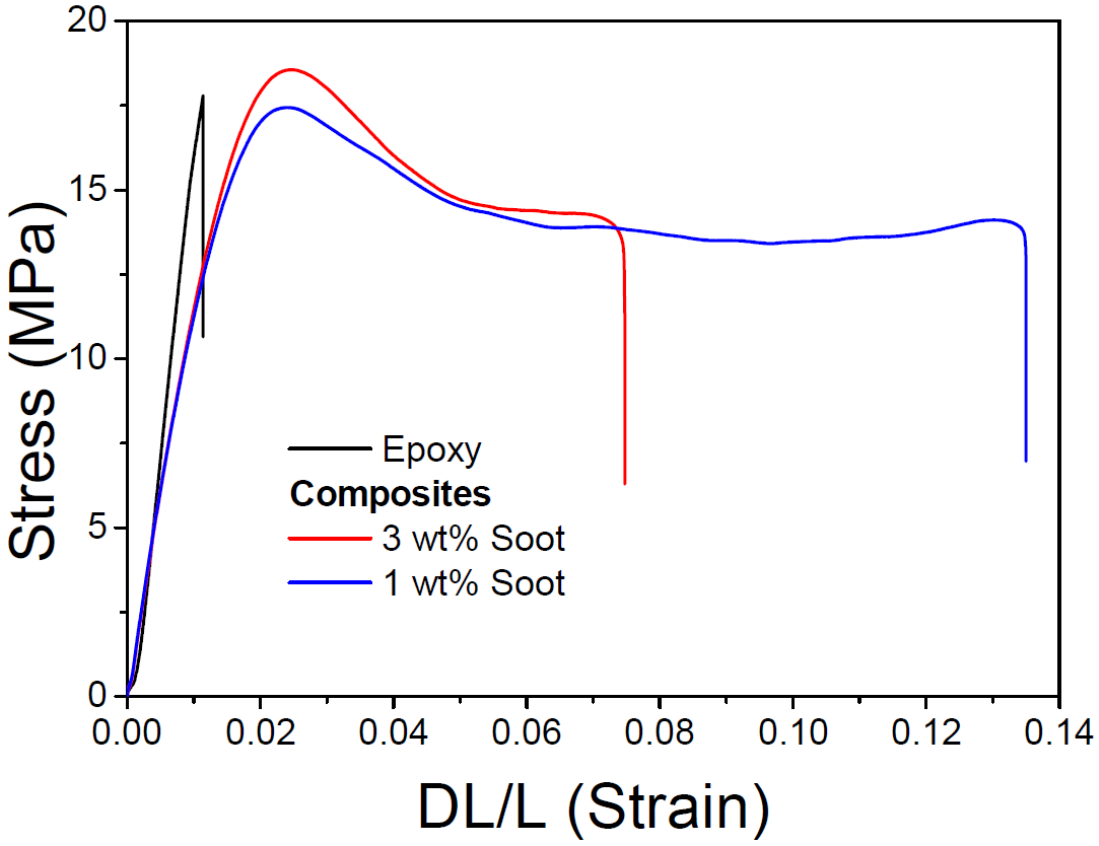

Figure 5. 3: Tensile test results of the epoxy and composites with 1 wt% and 3 wt%(Okonkwo et al., 2014)

5.1.2 Anodes for lithium ion batteries

This involves the use of our milled samples and hybrid carbon-silicon nanostructures to produce a low-cost but high energy lithium ion battery anodes. These anodes comprises of large quantity of our milled sample with quasi-amorphous nature and scrap silicon with crystalline nature. The nanocomposites formed with our milled sample and silicon combines the superior mechanical, electrochemical and electrical properties of our sample with the exceptional lithium intercalation ability of silicon. This nanocomposite is synthesized

through mechanical milling. Notwithstanding the success achieved previously through the use of carbon-silicon composites for lithium anodes, the fading effects of the composites is still inevitable (Wu et al., 2012, Park et al., 2009) but our milled samples increases the mechanical and electrical properties of the composite by coating the silicon particles thereby preventing the fading effect in specific capacity observed in previous studies of carbon-silicon composites

SEM images of the nanocomposites were taken and shown in Figure 5.3. We can observe the silicon structures embedded in the carbon nanostructures as the carbon acts as a coating agent. This is possible due to the high elastic properties of the graphene and graphitic particles present in the milled sample. The remaining part of the composite comprises of the polymeric binder, in form of a fiber, used to hold the silicon-carbon nanostructures together. For this study, silicon wafers were milled to submicrometric and nanometric sizes to improve their surface area and enhance adhesion to lithium. Figure 5.4 shows the SEM image of the composite as one contains 20% silicon and the other has 50% silicon.

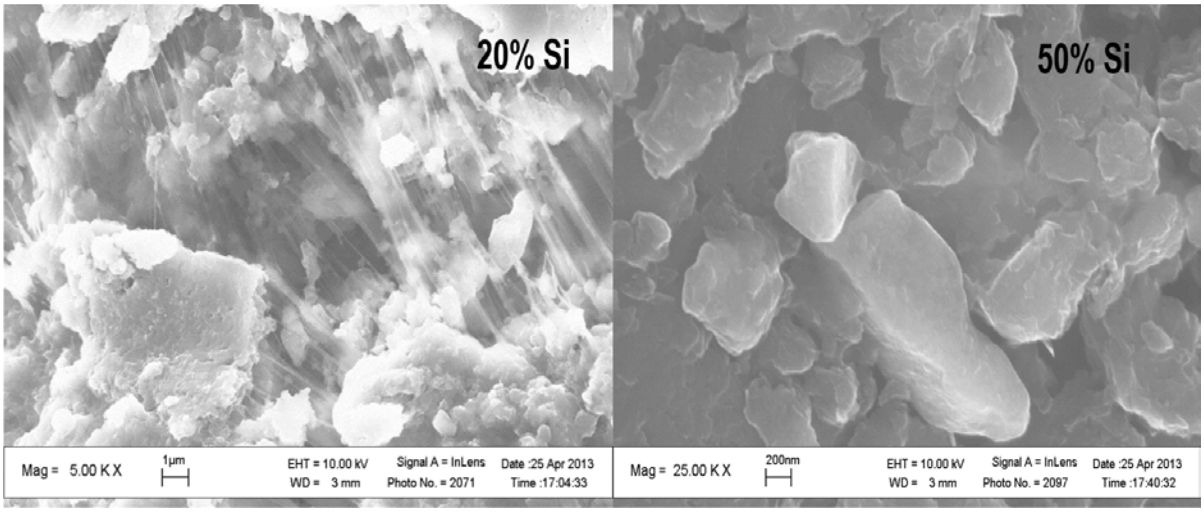

Figure 5. 4: SEM image of the composite (Badi et al., 2014)

Raman measurement was performed on the samples and the constituent peaks for both element and their particles are represented. The silicon peak (normally at 521 cm^{-1}) is present but rather small for the sample with 1wt% of silicon and increases as the percentage of the silicon increases since the Raman spectra is normalized. This increase in intensity is best noticed when compared with that of the G band as 0, 0.15, 1.25 and 5.6 goes for G band intensity and 0, 10, 20 and 50 goes for Silicon band intensity and represents 0wt% Si, 10wt% Si, 20wt% Si and 50wt% Si. 2D band present in the Raman spectra confirms the presence of graphene in the nanocomposite and it is responsible for the excellent elastic behavior of the nanocomposite. We can also observe the high dominance of the silicon peak in the Raman spectra which is attributed to the high crystallinity of silicon. Nevertheless, all carbon peaks are likewise identified in the spectra. Figure 5.5 shows the Raman spectra of the nanocomposites as they plotted according to the percentage of silicon present.

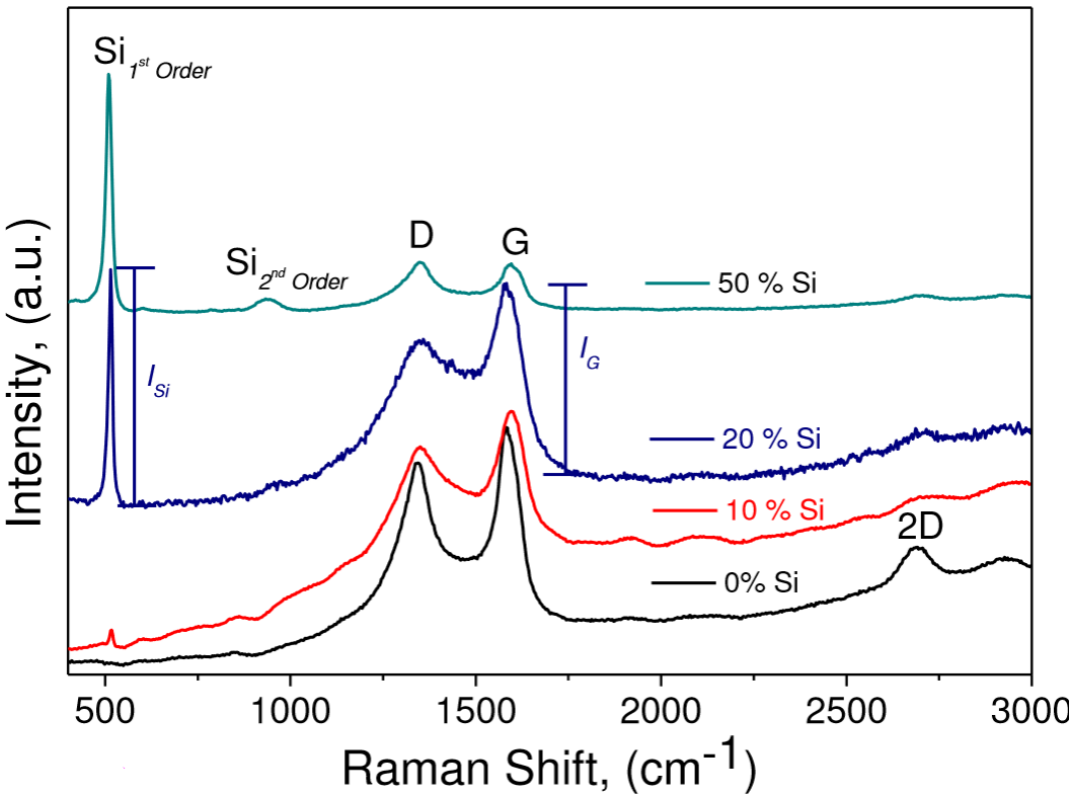

Figure 5. 5: Raman spectra of the nanocomposites with different constituent %

Raman mapping performed on the sample shows a great order of homogeneity of the sample. Figure 5.6 shows the Raman mapping of the nanocomposite. The image in (a) shows no sign of silicon as the sample is pure carbon while (b) shows great signs of silicon. The mapping of the nanocomposite with silicon present clearly shows that the mixture is highly homogenous and can be observed for the entirety of the analyzed portion. This confirms that the nanocomposite has been homogenously synthesize still possessing the graphene and graphitic nanostructures as they improve the fading effect initially stated in this study through mechanical milling and can be efficiently used for rechargeable batteries (Badi et al., 2014).

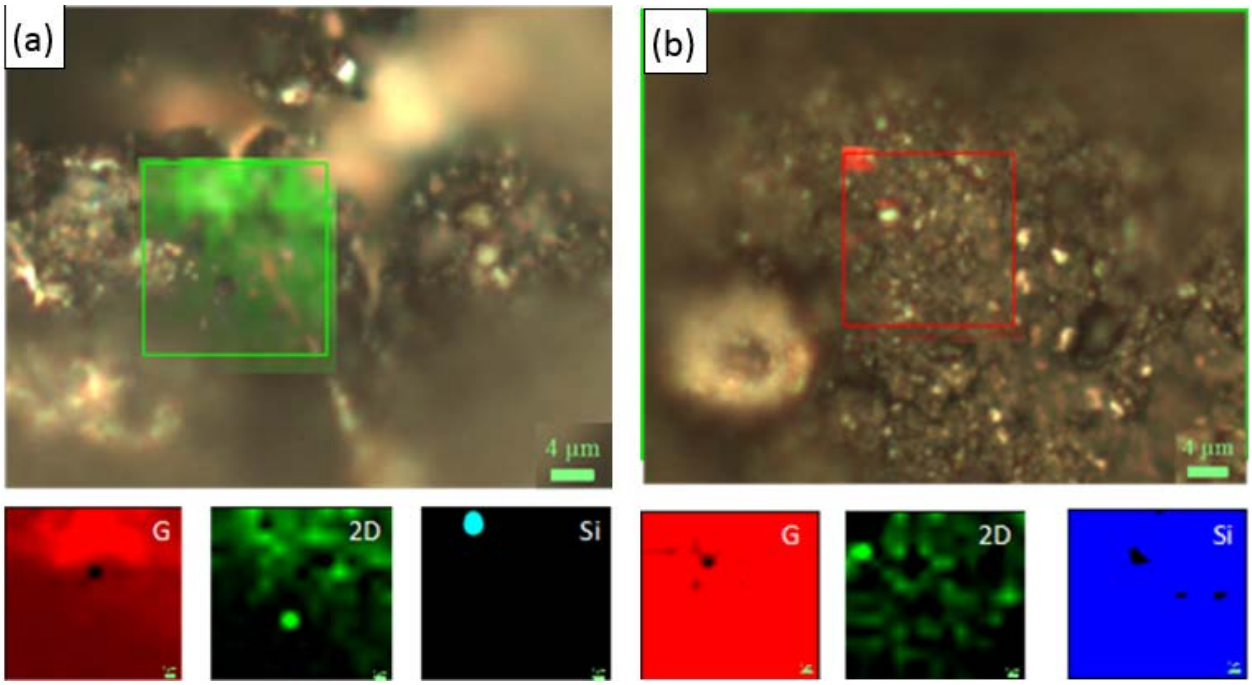

Figure 5. 6: Raman mapping of the nanocomposite (a) without silicon (b) with silicon (Badi et al., 2014)

The results from the electrochemical characterization are plotted in Figure 4.40 which shows the efficiency and capacity against the cycleability of the batteries made from the nanocomposites. The anode that was produced using only the activated carbon shows a reversible capacity of 112mAh/g after the 9^{th} cycle with a coloumbic efficiency of 21%. The anode produced with 20% silicon retains a capacity of 50mAh/g with a coloumbic efficiency of 10% and stabilizes after 16 cycles. While the anode that has just the milled sample retains a capacity of 61mAh/g with a columbic efficiency of 21% after stabilizing at 28 cycles (Badi et al., 2014). The nanocomposites that comprises of the silicon and milled sample was expected to increase the overall capacity of the cell as it increases the capacity of the anode. Rather it was the battery that bear the anode made from just the milled sample retains a higher capacity and efficiency and was able to stabilize after 28 cycles. Therefore, we can

say that increasing the silicon content reduces the properties of the battery thereby causing low performance of carbon-silicon based cells. This is attributed to the low electrical conductivity of the hybrid carbon-silicon material as a result of the oxidation of silicon particles during the thermomechanical milling process. Figure 5.7 shows the results from the electrochemical characterization of the composites.

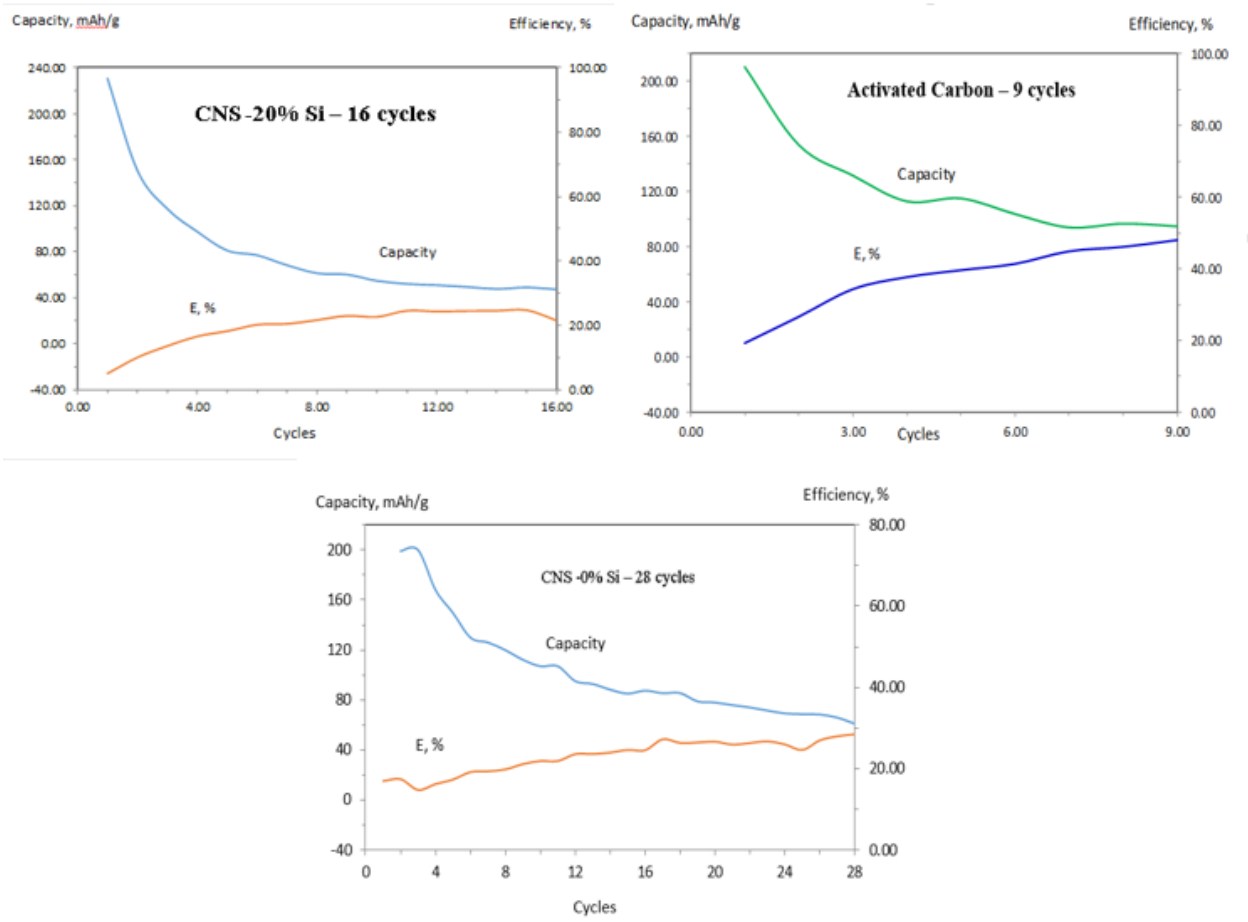

Figure 5. 7: Electrochemical characterization of the nanocomposites (Badi et al., 2014)

Conclusively, we were able to enhance the specific capacity, efficiency and cyclability of the anode of the lithium ion battery through the application of our milled sample as opposed to the currently available activated carbon. An important attribute of this

study includes the low cost of achieving such an enhanced properties of the anode as opposed to the currently available activated carbon.

5.1.3 Composites reinforcement

We have been able to efficiently reinforce many composites of different base matrix with nanostructural particles of our milled samples. This reinforcements have led to enhancements of different properties of the composites ranging from toughness, electrical conductivity, ductility, hardness etc. This enhancement is as a result of a homogenous coating of the milled carbon samples on the base matrix. The base matrix ranges from ceramics for applications in aerospace to extreme environmental conditions and biomaterials like chitosan. Though they form a composite with different matrix for different application but their chemical states are not altered. These reinforcements are achieved mostly through thermomechanical milling in order to enhance homogeneity, integrity and mechanical properties (Gilman and Benjamin, 1983, Suryanarayana, 2001). This method poses much more cost effective technique as opposed to the use of single walled carbon nanotubes and success have been recorded in this applications through the different research papers (Fals et al., 2012a, Fals et al., 2013).

Micro-hardness test were performed on the chitosan and chitosan-carbon nanostructures (CNS) composites that was milled and sintered at 180^0C and 220^0C for 3 hours to illustrate the improvements achieved through the reinforcement of the biomaterial with our milled samples. These samples were sintered with a constant applied load of 3.5 MPa. The results show significant improvements of about 40% increase in the micro-

hardness when compared to the raw chitosan. Table 5.1 shows the results of the micro-hardness test that was performed on the sintered chitosan and chitosan-CNS composites.

Table 5. 1: Micro-hardness test results of chitosan and chitosan-CNS composites (Robles Hernandez et al., 2014)

Sample	Micro-hardness, (μHV)	
	180^0C	220^0C
Chitosan		
Milled 6 hours	18.4 ± 5.4	23.1 ± 1.6
Milled 30 hours	15.1 ± 0.7	23.6 ± 0.1
Chitosan-CNS composite		
Milled 6 hours	21.2 ± 2.5	26.1 ± 2.7
Milled 30 hours	17.6 ± 1.8	24.1 ± 0.6
Sintered 12 hours		26.2 ± 0.8

Nano-hardness tests were also performed on the sintered chitosan and chitosan-CNS composites. These samples were milled for 6 hours and sintered for 3 hours at 220^0C. The nano-hardness results taken at tapping mode for the chitosan and chitosan-CNS composites shows Berkovich impressions on the chitosan sample but cannot be observed in the chitosan-CNS composite. Figure 5.8 shows the results from the nano-hardness of the sintered chitosan and chitosan-CNS composites. The insets represents images taken from the tapping mode as the dotted lines in the chitosan sample represents the Berkovich impressions.

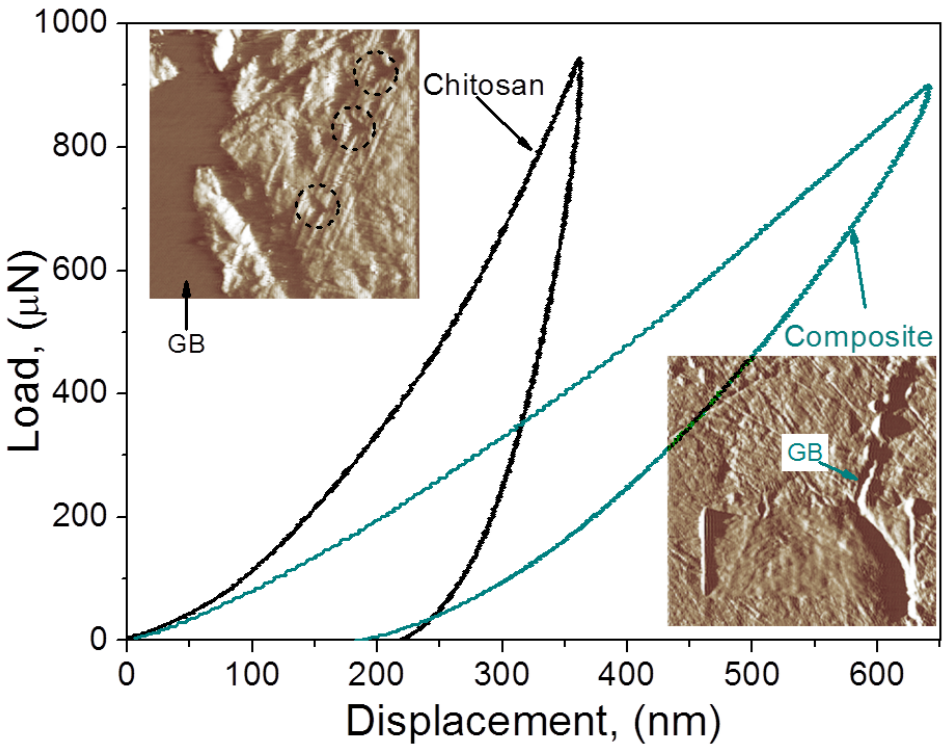

Figure 5. 8: Nano-hardness results of sintered chitosan and chitosan-CNS samples

Conclusively, fullerene soot poses a better and cost effective material for the synthesis of carbon nanostructures such as diamond, graphene and graphitic carbon thereby possessing a better tendency for the improvements of hardness, percolation, conductivity, densification and fracture toughness of ceramic composites. This improvements are best achieved with not more than 2wt% addition of the milled carbon samples, sonicated and sintered for 1 minute at 1500^0C. The resulting sample are highly dense possessing 15 orders of magnitude lower electrical resistivity, fracture toughness of 500% greater than that of the base material and 14.6 ± 4 GPa of hardness (Fals et al., 2012a).

5.1.4 All carbon composites

This involves the synthesis of carbon composites through high energy mechanical milling and spark plasma sintering for effective in-situ reinforcements. The as milled

samples possess carbon nanostructures resulting in excellent mechanical behavior which includes pure elastic behavior under nano and micro-hardness. The samples of shorter milling times displays a morphology of relaxed and highly deformed graphitic carbon structures. This characteristics can be seen clearly from the HRTEM images taken from the as milled samples of short milling times shown in Figure 5.9.

Figure 5.9 illustrates the graphene particles synthesized as a result of in-situ transformation of carbon during thermomechanical milling. We can clearly observe the double and triple layered graphene particles present in sample (a) as well as the multiple layers of graphene particles observed in sample (b). As the milling times increases, so does the synthesis of carbon nanostructures increases in layers of graphene stacking up to form graphitic carbon, onions and other complex structures with graphitic particles.

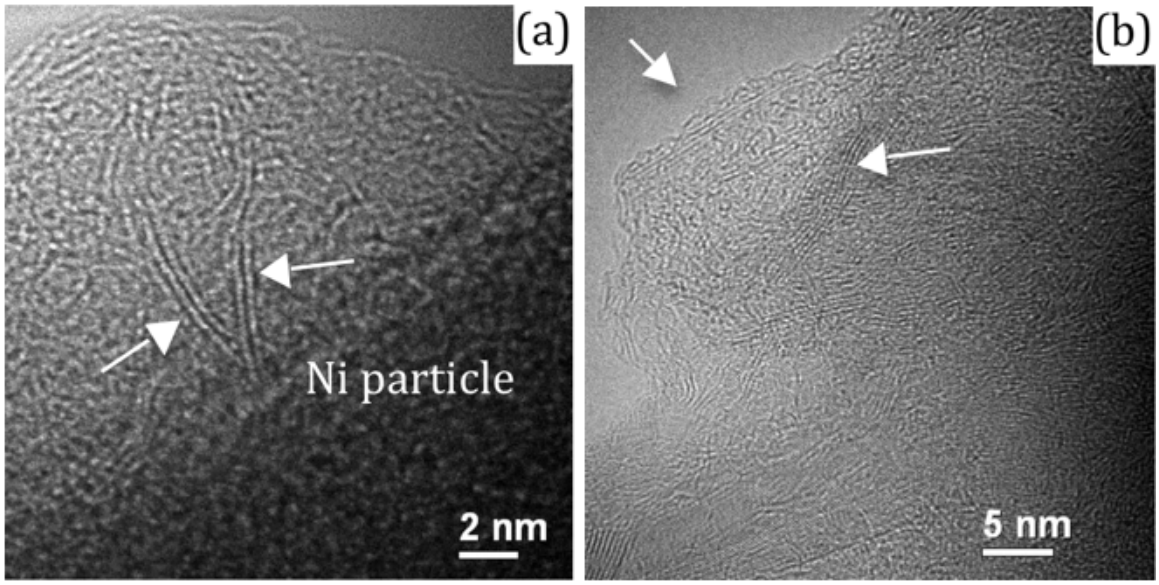

Figure 5. 9: HRTEM images of (a) double layer graphene (b) multiple layer graphene (Robles Hernandez et al., 2014)

Furthermore, the longer milling times synthesizes nano-diamond structures and can be observed through the HRTEM image as shown in Figure 5.10. Figure 5.10 illustrates the nano-diamond structures synthesized through 10 hours milling time. The HRTEM image concurs with the Raman spectra of the sample within the 2D peak. We can clearly see the nano-diamond structures which are characterized by the extra carbon atoms present in inset (b) of Figure 5.10. These extra carbon atoms are known as dumbbells which can also be used in the calibration of the TEM (Barber, 2013). Insets (b) and (c) shows the layers of graphene particles present within the material

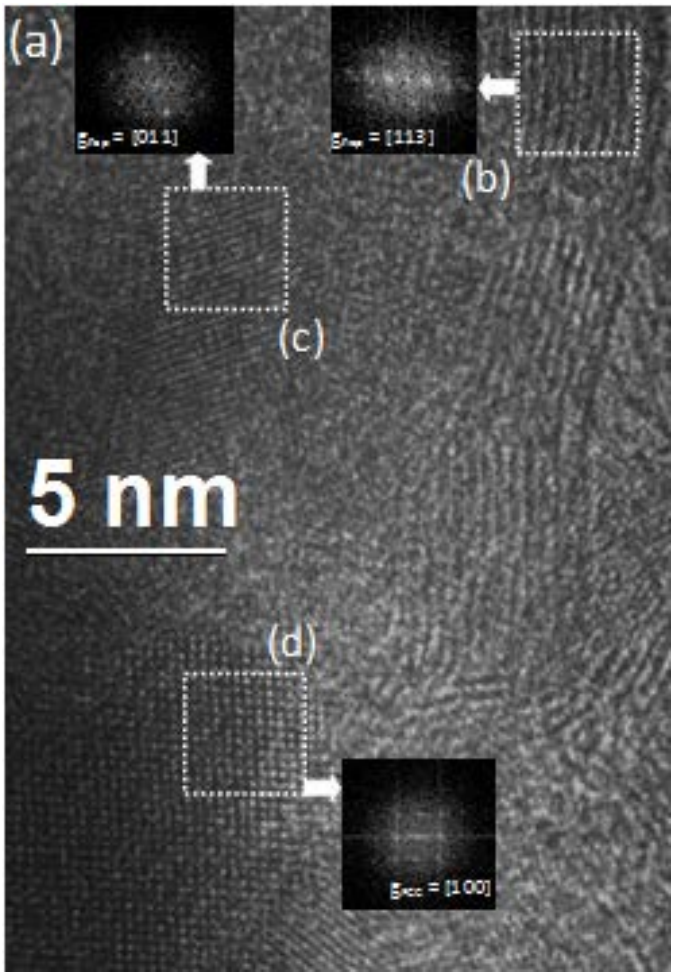

Figure 5. 10: HRTEM of nano-diamond particles observed from 10 hours milling time (Robles Hernandez et al., 2014)

The samples were sintered using spark plasma sintering method and was observed with the SEM. The SEM images from the sintered samples illustrates the transformation of the as milled samples into more complex nanostructures like diamond, multi-walled carbon nanotubes or giant onions. Figure 5.11 shows the nano-diamond synthesized from the sintered sample. The image in Figure 5.11 (b) illustrates that the material formed a plate-like structure with some nanotube structures on it. These structure can be attributed to the stretching caused within the milling crucible.

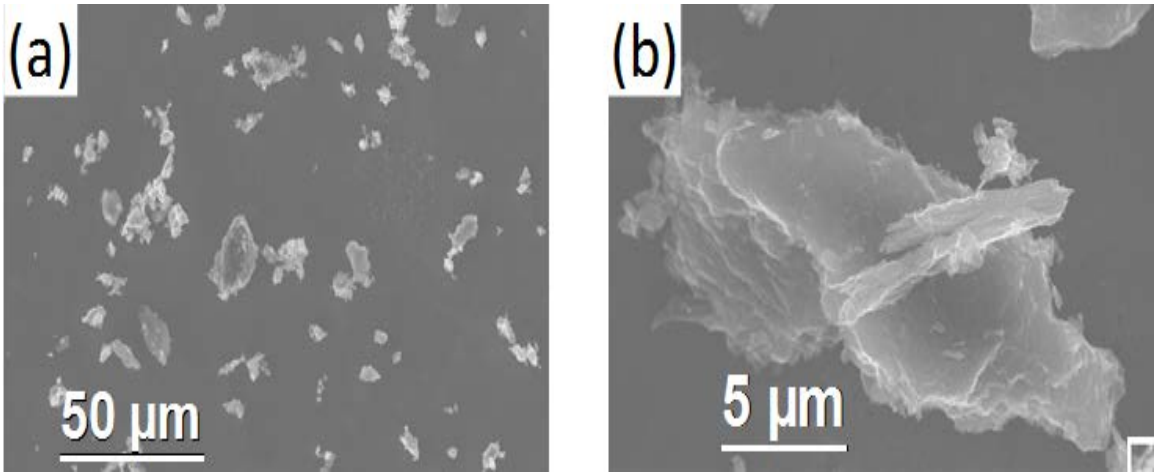

Figure 5. 11: HRTEM images of the sintered sample (Robles Hernandez et al., 2014)

The results of the nano-hardness was very impressive as the recovery of the samples are 284 nm, 390 nm and 536 nm having a permanent deformation of about 13.5%, 8.5% and 14.9% respectively. These results were obtained from carbon samples milled at 0.5, 2 and 20 hours respectively. Some of these results were compared with results of martensite. As we know that martensite is the hardest phase in the steel microstructure having iron and carbon so it possesses low elasticity, the recovery of martensite was of 51 nm showing approximately 73% of permanent deformation. Furthermore, the load over displacement

curves of nano-indentation that was tested on the fracture surface shows a bi-modal distribution. Figure 5.12 shows the results obtained from the nano-hardness for the samples milled with steel vial for 0.5, 2 and 20 hours as the load is plotted against the depth of indentation.

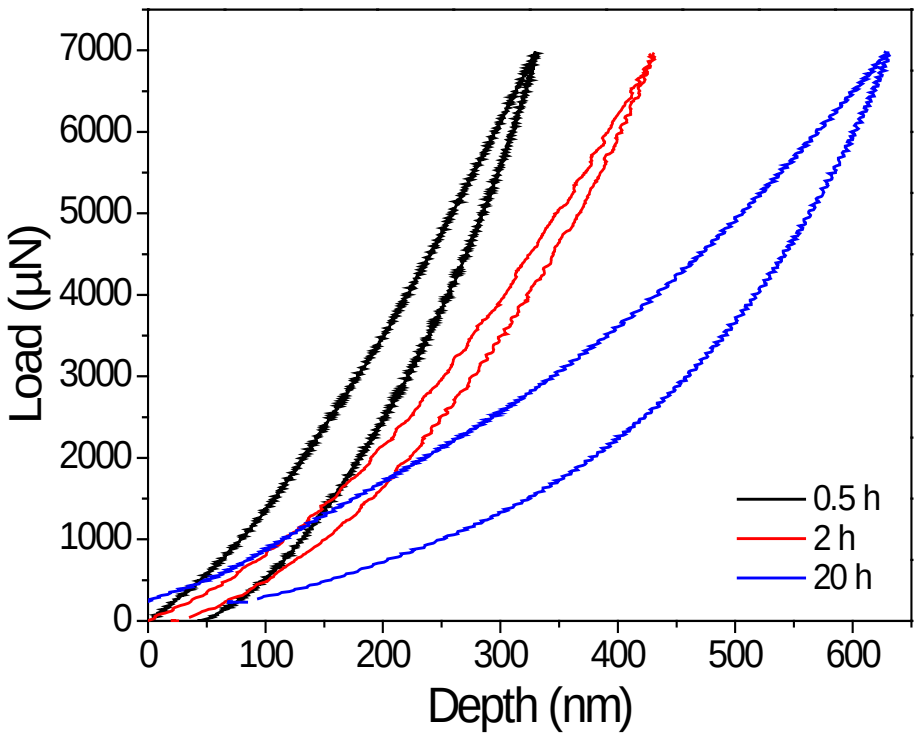

Figure 5. 12: Results of nano-hardness test for samples milled with steel vial for 0.5, 2 and 20 hours (Robles Hernandez et al., 2014)

Finally, the milled samples were in-situ reinforced through the synthesis of graphene, graphitic carbon and nano-diamond particles through mechanical milling. The graphitic particles ranges from 17 to 62 nm in the milled samples and increases significantly after sintering. The percentage of the sp3 bonding also increases to about 42% after sintering and these sintered samples possess full recovery under nano-scratch testing.

Chapter 6

6.1 Conclusion

The characterization techniques completes this project and instate through the gotten data that the processes of mechanical milling instigate the in-situ transformation of the commercially available fullerene soot to complex carbon nanostructures. The intriguing part of the project is the synthesis of nano-diamond through longer milling times which was achieved with both tungsten carbide and steel vial. More so, graphene and graphitic carbon were also observed in the milled samples. We will like to reiterate that all through this project, there was no addition of transition element to propel the in-situ transformation of the sample rather it was activated through the deformation created by the high energy milling balls that cause thermomechanical welding and transformation of the raw soot to other complex nanostructures.

An overview of the project presents the thermomechanical milling of the readily available fullerene soot using different milling vials which include steel, tungsten carbide and zirconium vials to in-situ transform the raw soot to complex carbon nanostructure. The milling times range from 1 hour to 50 hours. The as-milled samples were selected for the samples with little or no contamination. This led to disapproval of samples milled with zirconium vials because as short as 1 hour milling time created a lot of contamination for the sample. Selected samples were characterized using the Raman and XRD to understand the synthesis of these carbon nanostructures. Analysis of these results were performed using the Origin Pro to decipher the peak positions and to calculate the grain size (using XRD data) and the particle size (using the Raman data). The project concluded the synthesis of nano-diamond structures in the as milled samples notwithstanding the milling vial that was

used. We also determined that longer milling times (above 20 hours of milling) causes the material to become more amorphous yet the peaks are still identified in their positions rather more embedded into the background.

Furthermore, we introduced our novel solid state sintering technique which involves the pressureless sintering of the powder using induction heating. We sintered the samples at low (300^0C) and high temperature (2000^0C). These samples were characterized to check the effect of the sintering temperature. The data gotten show that there wasn't significant difference in sintering the samples at low or high temperature using our novel sintering techniques. This project further explored the structural applications of our samples in epoxy matrix composites, anodes for lithium ion batteries, composites reinforcements and all carbon composites.

Few samples were selected for analysis under the HRTEM. The images gotten from the equipment illustrates the presence of diamond which concurs with the results gotten from the XRD and Raman. They also prove the synthesis of complex carbon structures which includes graphene, nanostructures (nano-onions and nanotubes) and graphitic carbon.

The major objective of this project was achieved. This objective is the tendency to synthesize complex carbon nanostructures using cost effective method. This project demonstrated that mechanical milling is capable of causing in-situ transformation of fullerene soot to synthesize graphene, nano-diamond, graphitic carbon and carbon nanotubes. It introduced the novel sintering method that has no significant different in regards to the temperature used (high or low) which successfully consolidated the as milled samples at solid state. It also explored the structural applications of the samples. The

objective of this project were successfully performed, recorded, all the data obtained were analyzed and the results presented herein.

6.2 Future work

After the completion of this work, we recommend some extended studies on topics related to the applications and mechanical testing. So far, we have extended this product towards the improvement of structural composites including: anodes for lithium ion batteries, epoxy matrix, chitosan and all carbon composites. However, more studies will be able to explore more applications of the samples using these above mentioned as fundamentals to understand the working capabilities of the sample.

More work can be done on testing the hardness of the sintered samples at a micro and nano scale. The samples can also undergo tribology testing in order to understand more about the graphene characteristics of the sample. Production of the sample in a commercial scale is very important as it will lead to more refined production process to eliminate unnecessary inclusions and achieve high quality material. This will lead to the industrial analysis and other industrial applications.

Another recommendation is the improvement of the sintering procedures. This is necessary to avoid breaking of the sintered samples. This can be achieved by preventing the samples from sticking to the walls of the die after sintering. Improvement of this procedure can also be extended towards its application in the industry. Since we are producing transparent crystals (diamond) we are also working towards the wear resistance of the sintered products. Isolating the transparent crystals is key to investigate their optical properties and potentially being able to investigate if it is possible to use this materials for electronic and spintronics applications.

References

2009. Pirahna USV built using nano-enhanced carbon prepreg. *ReinforcedPlastics.com.*

ARTEMENKO, A., ELISSALDE, C., CHUNG, U. C., ESTOURNES, C., MORNET, S., BYKOV, I. & MAGLIONE, M. 2010. Linking hopping conductivity to giant dielectric permittivity in oxides. *Applied Physics Letters,* 97.

BADI, N., ERRA, A. R., HERNANDEZ, F. C. R., OKONKWO, A. O., MARTIROSYAN, K. & HOBOSYAN, M. 2014. Low-Cost Carbon-Silicon Nanocomposite Anodes for Lithium Ion Batteries. *Nano Research Letters,* 9.

BAGGOTT, J. 1994. Perfect Symmetry, The accidental discovery of Buckminsterfullerene. Oxford: Oxford University Press.

BARBER, D. A. 2013. *Cost Effective Thermomechanical Synthesis and Characterization of Complex Carbon Nanostructures for Structural Applications.* Masters of Science, University of Houston.

BERGER, C., SONG, Z. M., LI, T. B., LI, X. B., OGBAZGHI, A. Y., FENG, R., DAI, Z. T., MARCHENKOV, A. N., CONRAD, E. H., FIRST, P. N. & DE HEER, W. A. 2004. Ultrathin epitaxial graphite: 2D electron gas properties and a route toward graphene-based nanoelectronics. *Journal of Physical Chemistry B,* 108**,** 19912-19916.

BERGER, S., PORAT, R. & ROSEN, R. 1997. Nanocrystalline materials: A study of WC-based hard metals. *Progress in Materials Science,* 42**,** 311-320.

BOND, T. C., DOHERTY, S. J., FAHEY, D. W., FORSTER, P. M., BERNTSEN, T., DEANGELO, B. J., FLANNER, M. G., GHAN, S., KAERCHER, B., KOCH, D., KINNE, S., KONDO, Y., QUINN, P. K., SAROFIM, M. C., SCHULTZ, M. G., SCHULZ, M., VENKATARAMAN, C., ZHANG, H., ZHANG, S., BELLOUIN, N.,

GUTTIKUNDA, S. K., HOPKE, P. K., JACOBSON, M. Z., KAISER, J. W., KLIMONT, Z., LOHMANN, U., SCHWARZ, J. P., SHINDELL, D., STORELVMO, T., WARREN, S. G. & ZENDER, C. S. 2013. Bounding the role of black carbon in the climate system: A scientific assessment. *Journal of Geophysical Research-Atmospheres,* 118**,** 5380-5552.

BROOKER, E. J. & NUFFIELD, E. W. 1966. A GENERAL X-RAY METHOD FOR ORIENTING A CRYSTAL. *Acta Crystallographica,* 20**,** 496-&.

CALKA, A. & WEXLER, D. 2004. Mechanical milling assisted by electrical discharge - Recent developments. *In:* KIMINAMI, C. S., BOLFARINI, C. & BOTTAF, W. J. (eds.) *Ismanam 2003: Metastable, Mechanically Alloyed and Nanocrystalline Materials.*

CANCADO, L. G., PIMENTA, M. A., NEVES, B. R. A., DANTAS, M. S. S. & JORIO, A. 2004. Influence of the atomic structure on the Raman spectra of graphite edges. *Physical Review Letters,* 93.

CANCADO, L. G., TAKAI, K., ENOKI, T., ENDO, M., KIM, Y. A., MIZUSAKI, H., JORIO, A., COELHO, L. N., MAGALHAES-PANIAGO, R. & PIMENTA, M. A. 2006. General equation for the determination of the crystallite size L-a of nanographite by Raman spectroscopy. *Applied Physics Letters,* 88.

CHAIM, R., LEVIN, M., SHLAYER, A. & ESTOURNES, C. 2008. Sintering and densification of nanocrystalline ceramic oxide powders: a review 2. *Advances in Applied Ceramics,* 107**,** 159-169.

CHAMBERLAIN, A. L., FAHRENHOLTZ, W. G. & HILMAS, G. E. 2006. Pressureless sintering of zirconium diboride. *Journal of the American Ceramic Society,* 89**,** 450-456.

CHEN, P. W., HUANG, F. L. & YUN, S. R. 2004. Structural analysis of dynamically synthesized diamonds. *Materials Research Bulletin,* 39**,** 1589-1597.

CIZERON, G., DESSIEUX, R. & BARREAU, G. 1974. FUNDAMENTAL PROCESSES OF SINTERING IN SOLID-STATE - TRANSPOSITION TO CASE OF COMPACTS. *Annales De Chimie France,* 9**,** 305-321.

DEWIDAR, M. 2010. Microstructure and mechanical properties of biocompatible high density Ti-6Al-4V/W produced by high frequency induction heating sintering. *Materials & Design,* 31**,** 3964-3970.

EIZENBERG, M. & BLAKELY, J. M. 1979. CARBON INTERACTION WITH NICKEL SURFACES - MONOLAYER FORMATION AND STRUCTURAL STABILITY. *Journal of Chemical Physics,* 71**,** 3467-3477.

EL-ESKANDARANY, S. M. 2001. *Mechanical Alloying for Fabrication of Advanced Engineering Materials,* Norwich, NY 13815, Noyes Publications.

FABER, K. T. & EVANS, A. G. 1983. INTERGRANULAR CRACK-DEFLECTION TOUGHENING IN SILICON-CARBIDE. *Journal of the American Ceramic Society,* 66**,** C94-C96.

FALS, A. E., HADJIEV, V. G. & HERNANDEZ, F. C. R. 2012a. Multi-functional fullerene soot/alumina composites with improved toughness and electrical conductivity. *Materials Science and Engineering a-Structural Materials Properties Microstructure and Processing,* 558**,** 13-20.

FALS, A. E., HADJIEV, V. G. & HERNANDEZ, F. C. R. 2013. Porous media reinforced with carbon soots. *Materials Chemistry and Physics,* 140**,** 651-658.

FALS, A. E., HADJIEV, V. G. & ROBLES HERNÁNDEZ, F. C. 2012b. Multi-functional fullerene soot/alumina composites with improved toughness and electrical conductivity. *Materials Science and Engineering: A,* 558**,** 13-20.

FERRARI, A. C. & ROBERTSON, J. 2000. Interpretation of Raman spectra of disordered and amorphous carbon. *Physical Review B,* 61**,** 14095-14107.

FERRARI, A. C. & ROBERTSON, J. 2004. Raman spectroscopy of amorphous, nanostructured, diamond-like carbon, and nanodiamond. *Philosophical Transactions of the Royal Society a-Mathematical Physical and Engineering Sciences,* 362**,** 2477-2512.

FRANK, I. W., TANENBAUM, D. M., VAN DER ZANDE, A. M. & MCEUEN, P. L. 2007. Mechanical properties of suspended graphene sheets. *Journal of Vacuum Science & Technology B,* 25**,** 2558-2561.

FU, L., CAO, L. H. & FAN, Y. S. 2001. Two-step synthesis of nanostructured tungsten carbide-cobalt powders. *Scripta Materialia,* 44**,** 1061-1068.

GARCIA, F., LE BOLAY, N., TROMPETTE, J. L. & FRANCES, C. 2004. On fragmentation and agglomeration phenomena in an ultrafine wet grinding process: the role of polyelectrolyte additives. *International Journal of Mineral Processing,* 74**,** S43-S54.

GARDINER, D. J. 1989. *Practical Raman Spectroscopy,* New York, Springer-Verlag.

GARIBAY-FEBLES, V., CALDERON, H. A., ROBLES-HERNADEZ, F. C., UMEMOTO, M., MASUYAMA, K. & CABANAS-MORENO, J. G. 2000. Production and characterization of (Al, Fe)-C (graphite or fullerene) composites prepared by mechanical alloying. *Materials and Manufacturing Processes,* 15**,** 547-567.

GEIM, A. K. & NOVOSELOV, K. S. 2007. The rise of graphene. *Nature Materials,* 6**,** 183-191.

GHERIANI, R., BENSAHA, R. & HALIMI, R. 2010. Characterization of Titanium Carbides Coatings using X-ray Microanalysis in Scanning Electron Microscopy. *In:* OCHSNER, A., MURCH, G. E., SHOKUHFAR, A. & DELGADO, J. (eds.) *Diffusion in Solids and Liquids V, Pts 1 and 2.*

GILMAN, P. S. & BENJAMIN, J. S. 1983. MECHANICAL ALLOYING. *Annual Review of Materials Science,* 13**,** 279-300.

GOLDSTEIN, J., NEWBURY, D., D, J., LYMAN, C., ECHLIN, P., LIFSHIN, E., SAWYER, L. & MICHAEL, J. R. 2003. *Scanning Electron Microscopy and X-ray Microanalysis,* New York, Springer.

GULDI, D. M. & MARTIN, N. 2010. *Carbon Nanotubes and Related Structures,* Weinheim, Germany, Wiley-VCH Verlag GmbH & Co. KGaA.

GUO, C. X. & LI, C. M. 2011. A self-assembled hierarchical nanostructure comprising carbon spheres and graphene nanosheets for enhanced supercapacitor performance. *Energy & Environmental Science,* 4**,** 4504.

GUO, T., NIKOLAEV, P., RINZLER, A. G., TOMANEK, D., COLBERT, D. T. & SMALLEY, R. E. 1995a. SELF-ASSEMBLY OF TUBULAR FULLERENES. *Journal of Physical Chemistry,* 99**,** 10694-10697.

GUO, T., NIKOLAEV, P., THESS, A., COLBERT, D. T. & SMALLEY, R. E. 1995b. CATALYTIC GROWTH OF SINGLE-WALLED NANOTUBES BY LASER VAPORIZATION. *Chemical Physics Letters,* 243**,** 49-54.

HARRIS, P. J. F. 1999. *Carbon Nanostructures and Related Structures,* Cambridge, Cambridge University Press.

HIORNS, R. C., CLOULET, E., IBARBOURE, E., KHOUKH, A., BEJBOUJI, H., VIGNAU, L. & CRAMAIL, H. 2010. Synthesis of Donor-Acceptor Multiblock Copolymers Incorporating Fullerene Backbone Repeat Units. *Macromolecules,* 43**,** 6033-6044.

IIJIMA, S. 1980. DIRECT OBSERVATION OF THE TETRAHEDRAL BONDING IN GRAPHITIZED CARBON-BLACK BY HIGH-RESOLUTION ELECTRON-MICROSCOPY. *Journal of Crystal Growth,* 50**,** 675-683.

IIJIMA, S. 1991. HELICAL MICROTUBULES OF GRAPHITIC CARBON. *Nature,* 354**,** 56-58.

JAFARI, M., ENAYATI, M. H., ABBASI, M. H. & KARIMZADEH, F. 2010. Compressive and wear behaviors of bulk nanostructured Al2024 alloy. *Materials & Design,* 31**,** 663-669.

JONES, D. E. H. 1996. Science of fullerenes and carbon nanotubes - Dresselhaus,MS, Dresselhaus,G, Eklund,PC. *Nature,* 381**,** 384-384.

JORIO, A., LUCCHESE, M. M., STAVALE, F., MARTINS FERREIRA, E. H., MOUTINHO, M. V. O., CAPAZ, R. B. & ACHETE, C. A. 2010a. Raman study of ion-induced defects in N-layer graphene. *Journal of Physics-Condensed Matter,* 22.

JORIO, A., MARTINS FERREIRA, E. H., CANCADO, L. G., ACHETE, C. A. & CAPAZ, R. B. 2011. *Measuring Disorder in Graphene with Raman Spectroscopy,* CC BY-NC-SA.

JORIO, A., MARTINS FERREIRA, E. H., MOUTINHO, M. V. O., STAVALE, F., ACHETE, C. A. & CAPAZ, R. B. 2010b. Measuring disorder in graphene with the G and D bands. *Physica Status Solidi B-Basic Solid State Physics,* 247**,** 2980-2982.

JOSEYACAMAN, M., MIKIYOSHIDA, M., RENDON, L. & SANTIESTEBAN, J. G. 1993. CATALYTIC GROWTH OF CARBON MICROTUBULES WITH FULLERENE STRUCTURE (APPLIED PHYSICS LETTER, VOL 62, PG 202, 1993). *Applied Physics Letters,* 62**,** 657-659.

KANNO, Y., KAWASE, K. & NAKANO, K. 1987. ADDITIVE EFFECT ON SINTERING OF BORON-CARBIDE. *Yogyo-Kyokai-Shi,* 95**,** 1137-1140.

KENNEDY, J. & THORLEY, M. 1999. *Crystal Structure Determination,* , Oxford, William Clegg, Oxford University Press, Oxford.

KHALIL, A. K., KIM, S. W., DHARMARAJ, N., KIM, K. W. & KIM, H. Y. 2007a. Novel mechanism to improve toughness of the hydroxyapatite bioceramics using high-frequency induction heat sintering. *Journal of Materials Processing Technology,* 187**,** 417-420.

KHALIL, K. A.-R. & KIM, S. W. 2007a. High-frequency induction heating sintering of hydroxyapatite-(Zro(2)+3%Mol Y2o(3)) bioceramics. *In:* YOON, D. Y., KANG, S. J. L., EUN, K. Y. & KIM, Y. S. (eds.) *Progress in Powder Metallurgy, Pts 1 and 2.*

KHALIL, K. A. & ALMAJID, A. A. 2012. Effect of high-frequency induction heat sintering conditions on the microstructure and mechanical properties of nanostructured magnesium/hydroxyapatite nanocomposites. *Materials & Design,* 36**,** 58-68.

KHALIL, K. A., KIM, H. Y., KIM, S. W. & KIM, K. W. 2007b. Observation of toughness improvement of the hydroxyapatite bioceramics densified using high-frequency induction heat sintering. *International Journal of Applied Ceramic Technology,* 4**,** 30-37.

KHALIL, K. A. & KIM, S. W. 2006. Effect of processing parameters on the mechanical and microstructural behavior of ultra-fine Al2O3-(ZrO2+8%Mol Y2O3) bioceramic, densified by high-frequency induction heat sintering. *International Journal of Applied Ceramic Technology,* 3**,** 322-330.

KHALIL, K. A. & KIM, S. W. 2007b. Mechanical wet-milling and subsequent consolidation of ultra-fine Al2O3-(ZrO2+3%Y2O3) bioceramics by using high-frequency induction heat sintering. *Transactions of Nonferrous Metals Society of China,* 17**,** 21-26.

KHALIL, K. A. & KIM, S. W. 2007c. Synthesis and Densification of Ultra-fine Al2O3 - (ZrO2 + 3%Mol Y2 O3) bioceramics by high-frequency induction heat sintering. *Material Science Forum***,** 1033-1036.

KHALIL, K. A., KIM, S. W. & KIM, H. Y. 2007c. Consolidation and mechanical properties of nanostructured hydroxyapatite-(ZrO2+3 mol% Y2O3) bioceramics by high-frequency induction heat sintering. *Materials Science and Engineering a-Structural Materials Properties Microstructure and Processing,* 456**,** 368-372.

KIM, E.-S., HWANG, G., EL-DIN, M. G. & LIU, Y. 2012. Development of nanosilver and multi-walled carbon nanotubes thin-film nanocomposite membrane for enhanced water treatment. *Journal of Membrane Science,* 394**,** 37-48.

KIM, I., T & TANNENBAUM, R. 2011. *Magnetic Carbon Nanotubes: Synthesis, Characterization and Anisotropic Electrical Properties,* Georgia Institute of Technology, United States, NC-SA.

KIM, S. W. & KHALIL, K. A. R. 2006. High-frequency induction heat sintering of mechanically alloyed alumina-yttria-stabilized zirconia nano-bioceramics. *Journal of the American Ceramic Society,* 89**,** 1280-1285.

KIM, W., SUH, C.-Y., ROH, K.-M., LIM, J.-W., LEE, S., DU, S.-L. & SHON, I.-J. 2013. High-frequency induction heated sintering of High-energy ball milled TiC0.5N0.5 powders and mechanical properties of the sintered products. *Ceramics International,* 39**,** 585-591.

KINGERY, D. W., BOWEN, H. K. & UHLMANN, D. R. 1976. *Introduction to Ceramics,* John Wiley & Sons Academic Press.

KRATSCHMER, W., LAMB, L. D., FOSTIROPOULOS, K. & HUFFMAN, D. R. 1990. SOLID C-60 - A NEW FORM OF CARBON. *Nature,* 347**,** 354-358.

KROTO, H. W. 1996. Nobel Lecture: Symmetry, Space, Stars and C60. *Nobel Lectures, Chemistry 1996-2000*.

KROTO, H. W., HEATH, J. R., OBRIEN, S. C., CURL, R. F. & SMALLEY, R. E. 1985. C-60 - BUCKMINSTERFULLERENE. *Nature,* 318**,** 162-163.

KUZENKOVA, M. A., KISLYI, P. S., GRABCHUK, B. L. & BODNARUK, N. I. 1979. STRUCTURE AND PROPERTIES OF SINTERED BORON-CARBIDE. *Journal of the Less-Common Metals,* 67**,** 217-223.

LEE, C. H. & KIM, C. H. 1992. PRESSURELESS SINTERING AND RELATED REACTION PHENOMENA OF AL2O3-DOPED B4C. *Journal of Materials Science,* 27**,** 6335-6340.

LEE, H. & SPEYER, R. F. 2003. Pressureless sintering of boron carbide. *Journal of the American Ceramic Society,* 86**,** 1468-1473.

LI, H., LI, H. R., GUO, Z. C. & LIU, Y. 2006. The application of power ultrasound to reaction crystallization. *Ultrasonics Sonochemistry,* 13**,** 359-363.

LI, X., CAI, W., AN, J., KIM, S., NAH, J., YANG, D., PINER, R., VELAMAKANNI, A., JUNG, I., TUTUC, E., BANERJEE, S. K., COLOMBO, L. & RUOFF, R. S. 2009. Large-Area Synthesis of High-Quality and Uniform Graphene Films on Copper Foils. *Science,* 324**,** 1312-1314.

LI, Y. X., HUANG, Y. H., DU, S. X. & LIU, R. Z. 2001. Structures and stabilities of C-60-rings. *Chemical Physics Letters,* 335**,** 524-532.

LUCCHESE, M. M., STAVALE, F., FERREIRA, E. H. M., VILANI, C., MOUTINHO, M. V. O., CAPAZ, R. B., ACHETE, C. A. & JORIO, A. 2010. Quantifying ion-induced defects and Raman relaxation length in graphene. *Carbon,* 48**,** 1592-1597.

MANOJ, B. & KUNJOMANA, A. G. 2012. Study of Stacking Structure of Amorphous Carbon by X-Ray Diffraction Technique. *International Journal of Electrochemical Science,* 7**,** 3127-3134.

MARTIN, N., GULDI, D. M. & HIRSCH, A. 2011. Carbon nanostructures for energy. *Energy & Environmental Science,* 4**,** 604-604.

MARTINS FERREIRA, E. H., MOUTINHO, M. V. O., STAVALE, F., LUCCHESE, M. M., CAPAZ, R. B., ACHETE, C. A. & JORIO, A. 2010. Evolution of the Raman spectra from single-, few-, and many-layer graphene with increasing disorder. *Physical Review B,* 82.

MASIR, M. R. 2012. *Electronic Properties of Graphene in Inhomogenous Magnetic Fields.* PhD, Universiteit Antwerpen.

MCMULLAN, D. 2004. An improved scanning electron microscope for opaque specimens. *Advances in Imaging and Electron Physics, Vol 133,* 133**,** 59-91.

MERRITT, L. L. & STREIB, W. E. 1964. XRAY DIFFRACTION. *Analytical Chemistry,* 36**,** 399-&.

MIESSLER, G. L. & TARR, D. A. 2004. *Inorganic Chemistry,* Pearson Education.

MINTMIRE, J. W., DUNLAP, B. I. & WHITE, C. T. 1992. ARE FULLERENE TUBULES METALLIC. *Physical Review Letters,* 68**,** 631-634.

MITCHELL, D. R., BROWN, R. M., SPIRES, T. L., ROMANOVICZ, D. K. & LAGOW, R. J. 2001. The synthesis of megatubes: New dimensions in carbon materials. *Inorganic Chemistry,* 40**,** 2751-2755.

NEUBECK, S., YOU, Y. M., NI, Z. H., BLAKE, P., SHEN, Z. X., GEIM, A. K. & NOVOSELOV, K. S. 2010. Direct determination of the crystallographic orientation of graphene edges by atomic resolution imaging. *Applied Physics Letters,* 97.

OKONKWO, A. O., ROBLES HERNANDEZ, F. C., JAGADALE, P., GARCIA HERRERA, J. E., HADJIEV, V. G., SALDANA, J. M. & TAGLAFIERRO 2014. Ultra-ductile and low friction epoxy matrix composites. *Material Science Forum.*

PAGNI, J. 2010. Amroy aims to become nano-leader. *European Plastics News,* 5 March 2010.

PALANIANDY, S. & JAMIL, N. H. 2009. Influence of milling conditions on the mechanochemical synthesis of CaTiO3 nanoparticles. *Journal of Alloys and Compounds,* 476**,** 894-902.

PARK, M.-H., KIM, M. G., JOO, J., KIM, K., KIM, J., AHN, S., CUI, Y. & CHO, J. 2009. Silicon Nanotube Battery Anodes. *Nano Letters,* 9**,** 3844-3847.

PATTERSON, A. 1939. The Scherrer Formula for X-Ray Particle Size Determination. *Physical Review,* 56**,** 978 - 982.

PIMENTA, M. A., DRESSELHAUS, G., DRESSELHAUS, M. S., CANCADO, L. G., JORIO, A. & SAITO, R. 2007. Studying disorder in graphite-based systems by Raman spectroscopy. *Physical Chemistry Chemical Physics,* 9**,** 1276-1291.

PLESHAKOV, V. 2014. Computer models of icosahedral carbon nanostructures (shungite). *Journal of Applied Crystallography,* 47**,** 539-543.

POELMAN, D. & SMET, P. F. 2014. Time resolved microscopic cathodoluminescence spectroscopy for phosphor research. *Physica B-Condensed Matter,* 439**,** 35-40.

POURGHAHRAMANI, P. & FORSSBERG, E. 2007a. Changes in the structure of hematite by extended dry grinding in relation to imposed stress energy. *Powder Technology,* 178**,** 30-39.

POURGHAHRAMANI, P. & FORSSBERG, E. 2007b. Effects of mechanical activation on the reduction behavior of hematite concentrate. *International Journal of Mineral Processing,* 82**,** 96-105.

ROBERTSON, J. 2002. Diamond-like amorphous carbon. *Materials Science & Engineering R-Reports,* 37**,** 129-281.

ROBLES-HERNANDEZ, F. C. & CALDERON, H. A. 2010. Nanostructured Metal Composites Reinforced with Fullerenes. *Jom,* 62**,** 63-68.

ROBLES HERNANDEZ, F. C. & CALDERON, H. A. 2012. Nanostructured Al/Al4C3 composites reinforced with graphite or fullerene and manufactured by mechanical milling and spark plasma sintering. *Materials Chemistry and Physics,* 132**,** 815-822.

ROBLES HERNANDEZ, F. C., OKONKWO, A. O., CALDERON, H. A., BARBER, D. A., ALVAREZ RAMIREZ, F., QUINTERO, J., ORDOÑEZ OLIVARES, R. & HADJIEV, V. G. 2014. Pure Elastic Phenomena in all Carbon Composites and Applications. *VII Congreso Internacional de Metalurgia y Materiales.* Monclova, Coahuila Mexico 2014.

ROCHIE, S. 2000. Carbon Nanotubes: Exceptional Mechanical and Electrical Properties. *Annales de Chimie - Science des Materiaux***,** 529-532.

SANO, N., WANG, H., CHHOWALLA, M., ALEXANDROU, I. & AMARATUNGA, G. A. J. 2001. Nanotechnology - Synthesis of carbon 'onions' in water. *Nature,* 414**,** 506-507.

SANTANACH, J. G., ESTOURNES, C., WEIBEL, A., CHEVALLIER, G., BLEY, V., LAURENT, C. & PEIGNEY, A. 2011a. Influence of pulse current during Spark Plasma

Sintering evidenced on reactive alumina-hematite powders. *Journal of the European Ceramic Society,* 31**,** 2247-2254.

SANTANACH, J. G., WEIBEL, A., ESTOURNES, C., YANG, Q., LAURENT, C. & PEIGNEY, A. 2011b. Spark plasma sintering of alumina: Study of parameters, formal sintering analysis and hypotheses on the mechanism(s) involved in densification and grain growth. *Acta Materialia,* 59**,** 1400-1408.

SCHWETZ, K. A., GRELLNER, W. & LIPP, A. 1986. Mechanical Properties of HIP Treated Sintered Boron Carbide. *Inst. Phys. Conf.*

SCOTT, L. T., BOORUM, M. M., MCMAHON, B. J., HAGEN, S., MACK, J., BLANK, J., WEGNER, H. & DE MEIJERE, A. 2002. A rational chemical synthesis of C-60. *Science,* 295**,** 1500-1503.

SEITER, J., MULLER, E., BLANK, H., GEHRKE, H., MARKO, D. & GERTHSEN, D. 2014. Backscattered electron SEM imaging of cells and determination of the information depth. *Journal of microscopy,* 254**,** 75-83.

SETASUWON, P. & METANAWIN, T. 2009. Study of Diamond Film Interface Structure and Contacting Area. *Materials Research-Ibero-American Journal of Materials,* 12**,** 89-94.

SEUNG HUN, H., HAE-MI, J. & SUNG-HO, C. 2010. X-ray Diffraction Patterns of Thermally-reduced Graphenes. *Journal of the Korean Physical Society,* 57**,** 1649.

SHIH, T. T. & OPOKU, J. 1979. APPLICATION OF FRACTURE-MECHANICS TO CERAMIC MATERIALS - STATE-OF-THE-ART REVIEW. *Engineering Fracture Mechanics,* 12**,** 479-498.

SHVARTSBURG, A. A., HUDGINS, R. R., GUTIERREZ, R., JUNGNICKEL, G., FRAUENHEIM, T., JACKSON, K. A. & JARROLD, M. F. 1999. Ball-and-chain dimers from a hot fullerene plasma. *Journal of Physical Chemistry A,* 103**,** 5275-5284.

SICH, J., AMER ASSOC TEXTILE, C. & COLORISTS 1989. FIBER ANALYSIS THROUGH TRANSMITTED LIGHT AND SCANNING ELECTRON-MICROSCOPY. *1989 International Conference & Exhibition Aatcc: Book of Papers***,** 285-287.

SKOROKHOD, V., VLAJIC, M. D. & KRSTIC, V. D. 1996. Mechanical properties of pressureless sintered boron carbide containing TiB2 phase. *Journal of Materials Science Letters,* 15**,** 1337-1339.

SMILJANIC, O., STANSFIELD, B. L., DODELET, J. P., SERVENTI, A. & DESILETS, S. 2002. Gas-phase synthesis of SWNT by an atmospheric pressure plasma jet. *Chemical Physics Letters,* 356**,** 189-193.

STANKOVICH, S., DIKIN, D. A., PINER, R. D., KOHLHAAS, K. A., KLEINHAMMES, A., JIA, Y., WU, Y., NGUYEN, S. T. & RUOFF, R. S. 2007. Synthesis of graphene-based nanosheets via chemical reduction of exfoliated graphite oxide. *Carbon,* 45**,** 1558-1565.

STONER, B. R., RAUT, A. S., BROWN, B., PARKER, C. B. & GLASS, J. T. 2011. Graphenated carbon nanotubes for enhanced electrochemical double layer capacitor performance. *Applied Physics Letters,* 99.

SURYANARAYANA, C. 2001. Mechanical alloying and milling. *Progress in Materials Science,* 46**,** 1-184.

SYGULA, A., FRONCZEK, F. R., SYGULA, R., RABIDEAU, P. W. & OLMSTEAD, M. M. 2007. A double concave hydrocarbon buckycatcher. *Journal of the American Chemical Society,* 129**,** 3842-+.

TERRONES, H. & TERRONES, M. 1997. The transformation of polyhedral particles into graphitic onions. *Journal of Physics and Chemistry of Solids,* 58**,** 1789-1796.

TEWELDEBRHAN, D. & BALANDIN, A. A. 2009. Modification of graphene properties due to electron-beam irradiation. *Applied Physics Letters,* 94.

TUINSTRA, F. & KOENIG, J. L. 1970. RAMAN SPECTRUM OF GRAPHITE. *Journal of Chemical Physics,* 53**,** 1126-&.

UGARTE, D. 1992. CURLING AND CLOSURE OF GRAPHITIC NETWORKS UNDER ELECTRON-BEAM IRRADIATION. *Nature,* 359**,** 707-709.

VUL, A. Y. 2002. *Some aspects of fullerene application.*

VUL, A. Y. & HUFFMAN, D. R. 1998. Fullerene applications: The first steps from dreams to reality. *Molecular Crystals and Liquid Crystals Science and Technology Section C-Molecular Materials,* 10**,** 37-46.

WANG, L.-L. & JIANG, J.-S. 2007. Preparation of alpha-Fe2O3 nanoparticles by high-energy ball milling. *Physica B-Condensed Matter,* 390**,** 23-27.

WANG, X., LI, Q., XIE, J., JIN, Z., WANG, J., LI, Y., JIANG, K. & FAN, S. 2009. Fabrication of Ultralong and Electrically Uniform Single-Walled Carbon Nanotubes on Clean Substrates. *Nano Letters,* 9**,** 3137-3141.

WARNER, J. H. 2013. *Graphene: Fundamentals to Applications,* Elsevier.

WEN, B., ZHAO, J. J., LI, T. J. & DONG, C. 2006. n-diamond: an intermediate state between rhombohedral graphite and diamond? *New Journal of Physics,* 8.

WILLEMSEN, O. H., SNEL, M. M. E., CAMBI, A., GREVE, J., DE GROOTH, B. G. & FIGDOR, C. G. 2000. Biomolecular interactions measured by atomic force microscopy. *Biophysical Journal,* 79**,** 3267-3281.

WITHERS, J. C., LOUTFY, R. O. & LOWE, T. P. 1997. Fullerene commercial vision. *Fullerene Science and Technology,* 5**,** 1-31.

WONBONG, C. & LEE, J.-W. 2012. *Graphene: Synthesis and Application,* Boca Raton, CRC Press.

WU, H., CHAN, G., CHOI, J. W., RYU, I., YAO, Y., MCDOWELL, M. T., LEE, S. W., JACKSON, A., YANG, Y., HU, L. & CUI, Y. 2012. Stable cycling of double-walled silicon nanotube battery anodes through solid-electrolyte interphase control. *Nature Nanotechnology,* 7**,** 309-314.

XU, G., YAMAKAMI, T., YAMAGUCHI, T., ENDO, M., TARUTA, S. & KUBO, I. 2014. Pressureless Sintering of Carbon Nanofibre/SiC Composites and Their Properties. *International Journal of Applied Ceramic Technology,* 11**,** 280-288.

YANG, R. & ZHANG, H. 2014. Every Extremal Fullerene Graph with No Less than 60 Vertices is 2-Resonant. *Match-Communications in Mathematical and in Computer Chemistry,* 71**,** 99-114.

YU, K., LU, G., BO, Z., MAO, S. & CHEN, J. 2011. Carbon Nanotube with Chemically Bonded Graphene Leaves for Electronic and Optoelectronic Applications. *Journal of Physical Chemistry Letters,* 2**,** 1556-1562.

ZAKHARIEV, Z. & RADEV, D. 1988. PROPERTIES OF POLYCRYSTALLINE BORON-CARBIDE SINTERED IN THE PRESENCE OF W2B5 WITHOUT PRESSING. *Journal of Materials Science Letters,* 7**,** 695-696.

ZANELLO, L. P., ZHAO, B., HU, H. & HADDON, R. C. 2006. Bone cell proliferation on carbon nanotubes. *Nano Letters,* 6**,** 562-567.

ZAPATA-SOLVAS, E., GOMEZ-GARCIA, D., POYATO, R., LEE, Z., CASTILLO-RODRIGUEZ, M., DOMINGUEZ-RODRIGUEZ, A., RADMILOVIC, V. & PADTURE, N. P. 2010. Microstructural Effects on the Creep Deformation of Alumina/Single-Wall Carbon Nanotubes Composites. *Journal of the American Ceramic Society,* 93**,** 2042-2047.

ZHAN, G. D., KUNTZ, J., WAN, J., GARAY, J. & MUKHERJEE, A. K. 2002. Alumina-based nanocomposites consolidated by spark plasma sintering. *Scripta Materialia,* 47**,** 737-741.

ZHAN, G. D., KUNTZ, J. D., GARAY, J. E. & MUKHERJEE, A. K. 2003. Electrical properties of nanoceramics reinforced with ropes of single-walled carbon nanotubes. *Applied Physics Letters,* 83**,** 1228-1230.

ZHANG, Q., KANO, J. & SAITO, F. 2007. Fine Grinding of Materials in Dry Systems and Mechanochemistry. *Particle Breakage,* 12**,** 509-528.

ZHANG, Y. B., TAN, Y. W., STORMER, H. L. & KIM, P. 2005. Experimental observation of the quantum Hall effect and Berry's phase in graphene. *Nature,* 438**,** 201-204.